AGH University of Science and Technology
Faculty of Physics and Applied Computer Science

Master thesis

Marta Babicz

field of study: **technical physics**

The light collection system of ICARUS T600 detector for the Short Baseline Neutrino (SBN) experiment at Fermilab

Supervisor: **prof. dr hab. Agnieszka Zalewska**

CERN, September 2017

Aware of criminal liability for making untrue statements I decleare that the following thesis was written personally by myself and that I did not use any sources but the ones mentioned in the dissertation itself.

....

(czytelny podpis)

Cracow, 20 September 2017

The subject of the master thesis and the internship by Marta Babicz, student of 5th year major in technical physics

The subject of the master thesis:
The light collection system of ICARUS T600 detector for the Short Baseline Neutrino (SBN) experiment at Fermilab

Supervisor:	prof. dr hab. Agnieszka Zalewska
Reviewer:	Dr inz. Jan Kulka
A place of the internship:	CERN, Meyrin

Programme of the master thesis and the internship

1. First discussion with the supervisor on realization of the thesis.
2. Collecting and studying the references relevant to the thesis topic.
3. The internship:
    - establishing a plan of the internship,
    - participation in CENF-CERN group weekly meetings, WA104 Technical Working Group Meetings and in 8th International Conference on New Developments In Photodetection in France in July 2017 with a presentation of two posters,
    - development of the analysis software, participation in the LArSoft workshop,
    - discussions with the supervisor focused on the results obtained from the tests of photomultipliers,
    - preparation of the internship report.
4. Continuation of calculations concerning the thesis subject.
5. Ordering and first analysis of the calculation results.
6. Final analysis of the results obtained, conclusions – discussion with and the final approval of thesis contents by the thesis supervisor.
7. Completion of the thesis.

Dean's office delivery deadline: 21 September 2017

Recenzja1

Recenzja1

Recenzja2

Recenzja2

Contents

Introduction

During the last 50 years an enormous progress has been made in particle physics, astrophysics and cosmology. The Standard Model of particle physics and the Lambda-CDM cosmological model give a good base for interpretations of the results of numerous experiments and observations. However, fundamental questions remain open. What is the Dark Matter? What is the Dark Energy? Why matter dominates over antimatter in the Universe?

The baryonic matter, described by the Standard Model, is less than 5% of the Universe mass-energy. Thus, experimental observations pointing to physics from beyond the Standard Model are highly demanded. Neutrino oscillations, discovered and established in several experiments during the last 20 years are often considered to be the first such experimental fact. Actually, the 2015 Nobel Prize in physics was given for this discovery. The observation of neutrino oscillations means that at least two out of the three neutrino mass states have non-zero masses. These masses are so small that they have not yet been directly measured. The possible explanations of these tiny neutrino masses lead to many interesting theoretical hypotheses, in particular concerning the nature of Dark Matter. The recent hint of a strong, if not maximal, violation of the CP symmetry in the neutrino sector can possibly help to explain the observed asymmetry between matter and antimatter in the Universe.

Another interesting question in neutrino physics concerns the existence of one or more sterile neutrinos. If really observed, sterile neutrinos would offer a strong evidence for physics from beyond the Standard Model. Many experiments are dedicated to answering this question. One of them is the SBNE (Short Baseline Neutrino Experiment) experiment under preparation at FNAL (Fermi National Accelerator Laboratory) in the USA.

The work described in this diploma thesis is related to the ICARUS T600 detector, which will serve as the SBNE far detector. The T600 detector had already been successfully used in the ICARUS experiment at the CNGS (CERN Neutrinos to Gran Sasso) beam in the underground Gran Sasso laboratory. This was the first and up to now the largest LArTPC (Liquid Argon Time Projection Chamber) ever used in neutrino studies. This experimental technique is becoming very popular and in particular LAr detectors with a total mass of 40 kton are prototyped for the future long baseline neutrino programme in the USA.

In 2014 the ICARUS T600 detector was transported from Gran Sasso to CERN, where for a period of more than two years it had been refurbished. During that time I have been twice at CERN: as a scholar of the AGH University of Science and Technology in summer 2015 and as a CERN technical student from September 2016 till October 2017. In both cases I worked within the CERN Neutrino Platform (CENP) on the preparation of the ICARUS T600 detector for its application in SBNE.

The main subject of my internship at CERN was related to the T600 light collection system a fundamental task for the detector functioning at a shallow depth at FNAL. My contributions include: tests of photomultiplier tubes (PMTs) at room and at LAr temperatures, test data analysis, tests of dedicated electronics boards and cabling of PMTs. I was also responsible for collecting and documenting all the available data for the future PMT database of SBNE. The PMT tests and their results are described in this diploma thesis. The input data for the PMT database are presented in the Appendix. This data has already been used for different purposes. Some initial results concerning tests of the first 20 PMTs were presented at an IEEE conference.

In addition to this main subject of my scholarship at CERN, I have participated in two R&D projects. One of them was studying the performance of silicon photomultipliers (SiPMs) as a future alternative for PMTs. SiPMs are the semiconductor-based devices with performances comparable to the PMTs, but with very small active areas. For test purposes we built a prototype array composed by SiPMs connected in different electrical configurations. The preliminary results of tests made with four SiPMs, connected both in parallel and in series configurations, and deployed into a 50 liters LAr-TPC exposed to cosmic rays at CERN, were presented at the14th Topical Seminar on Innovative Particle and Radiation Detectors (IPRD16) in Siena in October 2016 [1]. Further progress in this work was presented by me at the 8th International Conference on New Developments In Photodetection in Tour in July 2017 in the form of two posters. The article for the conference proceedings is in preparation. Another project with my participation concerns the measurement of the scintillation light (128 nm) propagation and attenuation in Liquid Argon. The studies have been performed using cosmic muon tracks and the related paper is under preparation for publication.

The present diploma thesis consists of this introduction, five chapters, a summary and an Appendix. Chapter 1 gives a brief introduction to neutrino physics. Chapter 2 concerns the Liquid Argon detection technique and its application in the experiments studying neutrino oscillations. Technical aspects of the ICARUS T600 detector in its past and for the future use are presented in Chapter 3. Chapter 4 contains the description of the new light collection system of the T600 detector based on 360 8 PMTs. In Chapter 5 the PMT tests and their results are presented. The Appendix contains the input data for the future PMT database to be used in the SBNE experiment.

1 Introduction to neutrino physics

The theoretical hypothesis positing the neutrino existence was proposed by W. Pauli in 1930 as an explanation of the observed energy spectra in β-decays. In the process of β-decay a nucleus of atomic number Z transforms to one with a smaller mass and atomic number $Z+1$ and an emitted electron is observed:

$$ {}^{A}_{Z}X \rightarrow {}^{A}_{Z+1} X^{`} + e^{-}, \tag{1} $$

According to the Einstein equation $E = mc^2$ it was predicted that in such a two-body decay electron would carry off the difference of masses of nuclei in the form of kinetic energy. Nevertheless, the observations showed that in various observed β-decays the electron always carried off less energy than expected and instead of all electrons having the same energy there was a continuous distribution like it is shown in Figure 1.

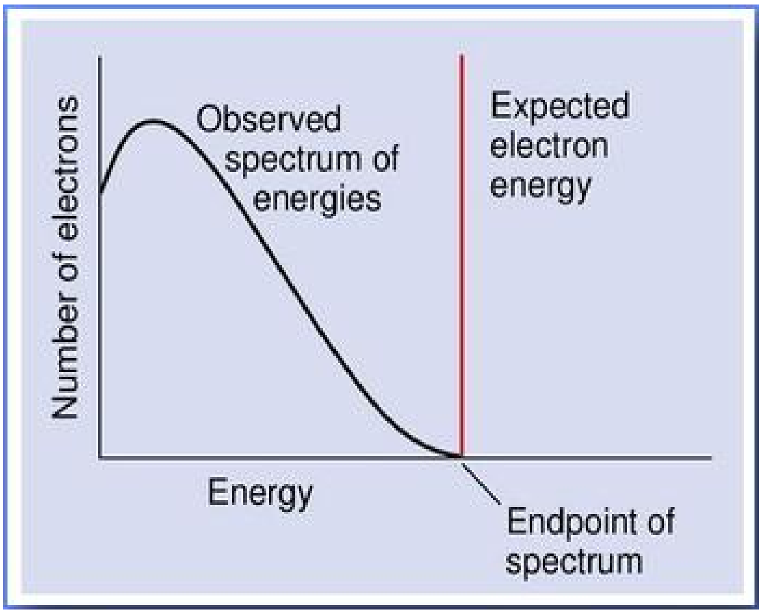

Figure 1: The observed distribution of energy of electrons emitted in a β-decay.

In addition, both the parent nucleus and daughter nucleus have either integer or half-integer spins which was not consistent with an emission of an electron which has spin $\frac{1}{2}$. That would mean that the law of conservation of energy and of angular momentum did not hold at the atomic level.

Fortunately, the Pauli hypothesis of the existence of a very light neutral particle of spin $\frac{1}{2}$, very weaekly interacting with matter and emitted alongside the electron in β-decay, explained the continuous spectrum and helped with solving both non-conservation problems. The name of neutrino was given to this new hypothetical particle by E. Fermi who later on developed a theory of β-decay [2]. The electron neutrino produced in the β-decay was discovered in the Cowan and Reines experiment in 1956 [3].

1.1 Basic properties of neutrinos

The Standard Model (SM) of particle physics describes neutrinos as neutral leptons. The SM is the most prevailing theory which describes the most elementary particles and three fundamental interactions: the electromagnetic, weak, and strong.

The existance of three generations of elementary particles of matter with half-integer spin, called fermions, was proved by the experiments at the Large Electron-Positron (LEP) collider at CERN [4], but it does not have a theoretical explanation. Each generation contains one pair of leptons (charged and neutral) and one pair of quarks (with electrical charges $+\frac{2}{3}$ and $-\frac{1}{3}$) which totals to six leptons and six quarks. Moreover, each of these particles has a corresponding antiparticle and each quark possesses a property called color charge. In Figure 2, the first three columns show the Standard Model elementary particles of matter with their principal properties.

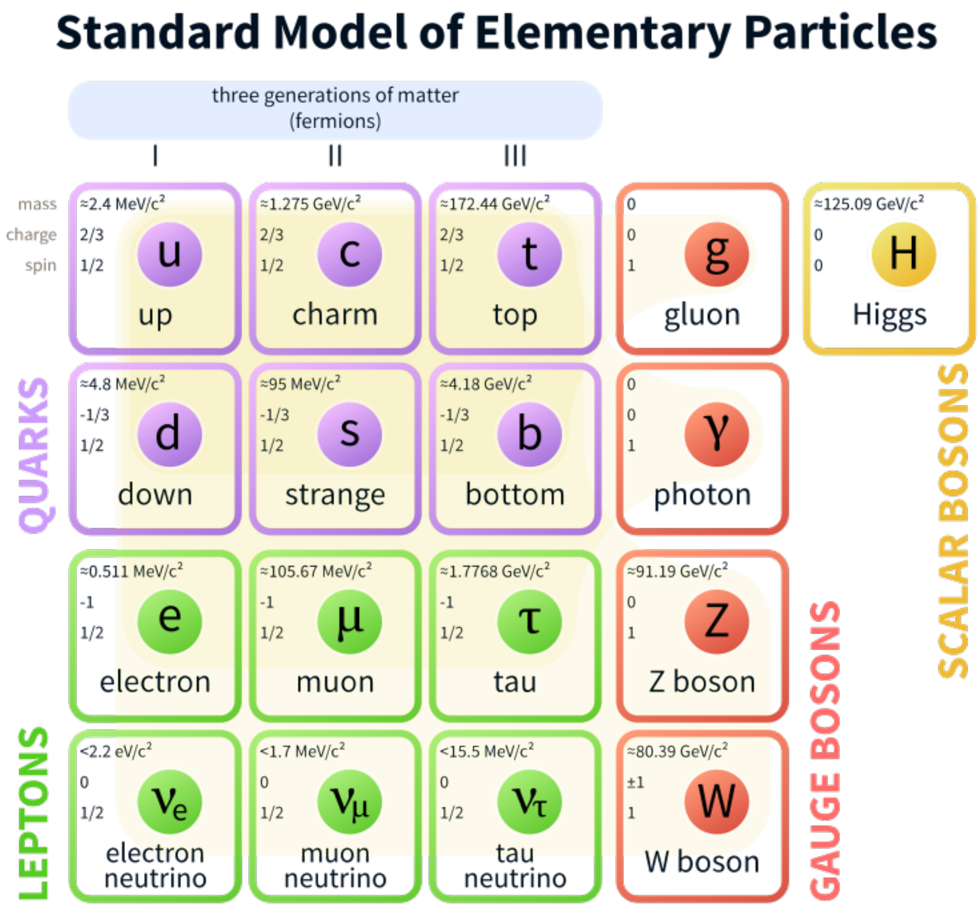

Figure 2: The Standard Model of elementary particles, with the three generations of matter particles in the first three columns, gauge bosons in the fourth column, and the Higgs boson in the fifth.

All the particles described by the Standard Model are interacting with the force mediating particles, which unlike fermions have integer spin equal 1. According to the Standard Model these gauge bosons, namely gluons, $W^{\pm}$ and Z and photons are force carriers that mediate the strong, weak and electromagnetic fundamental interactions, respectively. In Figure 2, the gauge bosons are listed in the fourth column. There is also a Higgs boson with spin 0, discovered at CERN in 2012 [5][6]. In SM it explains how fundamental particles acquire mass.

In SM neutrinos exist in three flavors (ν_e,ν_μ,ν_τ). They have no electric charge, are massless and left-handed. Their corresponding antiparticles are right-handed. However, propounded by SM zero mass of neutrinos has turned to be antithetical to observations of neutrino oscillations in detector Super-Kamiokande in Japan [7] and in Canadian experiment called Sudbury Neutrino Observatory (SNO) [8][9], and subsequently confirmed by series of other experiments. The ν_μ disappearance observed by Super-Kamiokande in the atmospheric data can be very well explained by the presence of $\nu_\mu \to \nu_\tau$ oscillation. The oscillation parameters fitted to Super Kamiokande data were given by $\Delta m^2 = 2.5 \times 10^{-3} ev^2$ with $sin^2 2\theta = 1.0$. The range of allowed values at 90% confidance level correspond to $5 \times 10^{-4} < \Delta m^2 < 6 \times 10^{-3} eV^2$ and $sin^2 2\theta > 0.82$ [7]. The data published by the SNO [9] demonstrated a clear flavour change process through the well established solar neutrino deficit. The solar observations are compatible with an oscillation process aiding again a large mixing angle but at a Δm^2 one order of magnitude less than for the atmospheric data. In order to study the nature of the oscillation mechanism the first generation of long baseline experiments has been launched.

The fact that neutrinos can oscillate is a quantum mechanical phenomenon whereby a neutrino created with a specific lepton flavour can later be detected as having a different flavour. This means that neutrinos have non-zero mass [10]. Since neutrinos are neutral leptons they interact only via the weak subatomic force. Due to their extremely low interaction cross-sections, of the order of 10^{-43} cm^2 at 1 MeV, neutrino interactions are very difficult to observe. Mediating bosons exchanged during these interactions are $W^{\pm}$ and Z^0. Depending on which one of these particles mediates in the interaction, there are two kinds of weak interactions. The first one is called the charged-current (CC) interaction, because it is mediated by bosons W^- or W^+, which are particles that carry an electric charge and the second one is called the neutral-current (NC) interaction, because it is is mediated by Z^0 boson, which is a neutral particle. In the CC interactions, a charged lepton (such as an electron or a muon with negative charge) can absorb a W^+ boson (a particle with a charge of +1) and be thereby converted into a corresponding neutrino (with a charge of 0), where the type of neutrino corresponds to the type of lepton in the interaction. Vice versa, the type of charged lepton produced in the neutrino CC interaction is used for the identification of the interacting neutrino flavour. In particle physics the interactions are described by the so called Feynman diagrams. The examples of the diagrams showing the weak interactions with neutrinos are illustrated in Figure 3.

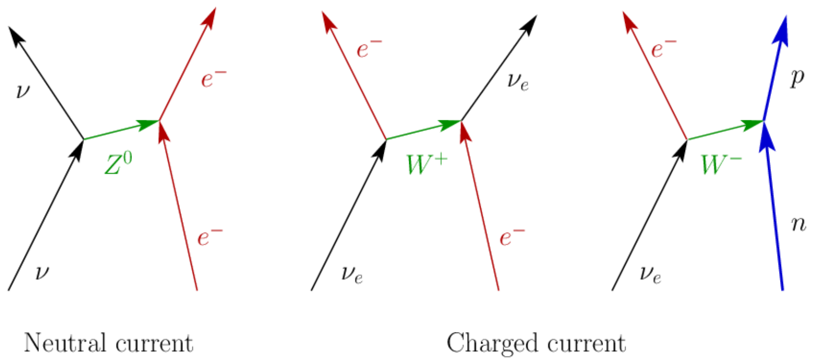

Figure 3: Examples of the neutrino scattering Feynman diagrams.

Neutrinos are the second most abundant particles in the Universe after photons. The estimate is that each cubic centimeter of the Universe contains more than 300 relic neutrinos created shortly after the Big Bang. There are several other natural neutrino sources, including the interactions of cosmic rays with atomic nuclei in the Earth's atmosphere, the nuclear reactions in the cores of stars, and Supernova explosions. The majority of neutrinos in the vicinity of the Earth are from nuclear reactions in the core of Sun. About 65 billion solar neutrinos per second pass through every square centimeter perpendicular to the direction of the Sun [11]. Neutrinos can be also created artificially with nuclear reactors and particle accelerators.

1.2 Neutrino oscillations

Neutrino and antineutrino oscillations were first proposed by B. Pontecorvo [12] [13]. In 1962, Japanese physicists Z. Maki, M. Nakagawa, S. Sakata [14] introduced the idea of neutrino flavour oscillations. However, only at the end of the 20th century this effect has been experimentally confirmed, giving the final answer to some puzzles like Solar neutrino problem [15] or atmospheric neutrino anomaly [16] [17].

The observations of Solar neutrinos in several initial experiments resulted in the measurements of only $\frac{1}{3} - \frac{1}{2}$ of the expected neutrino flux. This phenomenon was called Solar neutrino problem. The deficit of muon neutrino interactions as compared to electron neutrino interactions, called the atmospheric neutrino anomaly, was observed in 80. and early 90. in some experiments searching for proton decay, predicteed by Grand Unified Theories (GUT) [18]. Neutrino interactions were the most substantial background for proton decays, hence their studies in the experiments dedicated to GUTs.

Both the Solar neutrino problem and atmospheric neutrino anomaly were resolved by the observations of neutrino oscillations [10]. This phenomenon was first discovered by the SuperKamiokande experiment in 1998 [7], where a deficit in the ratio of the flux of muon to electron flavour atmospheric neutrinos as well as the correlation between the muon neutrino disappearance and the distance traveled to the detector have been observed with a sufficient statistical significance and interpreted as the $\nu_\mu \leftrightarrow \nu_\tau$ oscillation. After 1998 the oscillation phenomenon has been confirmed and precisely measured by several experiments with solar, reactor and accelerator neutrinos.

The detection of neutrino oscillations implies that neutrinos have non-zero masses. Assuming the existance of only two kinds of neutrino flavours α and β and two states of mass 1 and 2, the probability that a neutrino originally of flavour α will later be observed as having flavour β is:

$$P(\nu_\alpha \rightarrow \nu_\beta) = sin^2 2\theta sin^2(1,27\Delta m^2 \frac{L}{E}), \tag{2}$$

where:

- $\Delta m^2 = m_2^2 - m_1^2$ is the mass square difference in eV^{-2} units;
- θ - is the mixing angle of states 1 and 2;
- L - is the distance traveled by neutrinos in km;
- E - is the neutrino's energy in GeV.

For this simplified model the probability of oscillation $\nu_\alpha \rightarrow \nu_\beta$ depends on only two theoretical parameters, namely Δm^2 and θ, and on two experimental parameters - the distance traveled by neutrinos and neutrino energy. The L/E ratio has to be taken into account while designing experiments dedicated to neutrino oscillation studies.

More accurate theoretical description of neutrino oscillations in vacuum can be obtained for three neutrino flavours (ν_e, ν_μ, ν_τ) and three states of mass (m_1, m_2, m_3). Therefore, there are 6 theoretical parameters: three mixing angles θ_{12}, θ_{23}, θ_{13}, two mass square differences Δm_{12}^2, Δm_{23}^2 and phase factor δ_{CP} which is different than 0 or π if the CP symmetry is not conserved for neutrinos. The simplified model with two neutrino states described well the experimental results from the initial oscillation experiments because of the small value of the mixing angle θ_{13} in comparison to the two other mixing angles. The first statistically significant measurement of θ_{13} and the best up to now come from the Daya Bay experiment [19] [20].

Values of the oscillations parameters obtained by fitting the current oscillation data with 1 σ uncertainity are as follows: $\Delta m^2_{21} \simeq 7.54^{+0.26}_{-0.22} \times 10^{-5} eV^2$, $\Delta m^2_{31} \simeq \Delta m^2_{32} \simeq 2.43^{+0.06}_{-0.10} \times 10^{-3} eV^2$, $sin^2\theta_{12} \simeq 0.307^{+0.18}_{-0.16}$, $sin^2\theta_{23} \simeq 0.386^{+0.24}_{-0.21}$, $sin^2\theta_{13} \simeq 0.0241 \pm -0.0025$ for normal hierarchy [21] [22].

The second theoretical refinement of the oscillation description is essential while neutrinos are rippling through the matter, for example neutrinos passing from the core of the Sun to its surface. The optimized experiments dedicated to more precise measurements of the oscillation parameters take into account all the above-mentioned requirements; however, it is not possible to make a precise measurement of all the parameters simultaneously in a single experiment.

1.3 Sterile Neutrino

According to many neutrino oscillation studies, based on solar, atmospheric, reactor and accelerator neutrinos, the oscillation mechanism is explained by three neutrino flavours. However, some experiments demonstrate possible deviations from the three neutrino flavours model.

The first anomaly came up from the $\bar{\nu}_\mu \rightarrow \bar{\nu}_e$ transition studies in the Liquid Scintillator Neutrino Detector (LSND) [23]. The LSND collaboration measured the $\bar{\nu}_\mu$ neutrino flux produced in the antimuon decays ($\mu^+ \rightarrow e^+\nu_e\bar{\nu_\mu}$) from pion decays ($\pi^+ \rightarrow \mu^+\nu_\mu$). The excess of the $\bar{\nu}_e$ flux of about 3.8 σ above the expected background was observed. That points out to Δm^2 in the range from $0.2eV^2$ to $2eV^2$ for the oscillation $\bar{\nu_\mu} \rightarrow \bar{\nu}_e$ and requires another species of neutrino which is called sterile neutrino.

The Mini Booster Neutrino Experiment (MiniBooNE) was designed in order to examine the LSND observation with a higher precission. The parameters of this experiment were selected to fit the LSND-like L/E ratio. The aim was to investigate the $\nu_\mu \rightarrow \nu_e$ and $\bar{\nu_\mu} \rightarrow \bar{\nu}_e$ transitions. The extracted parameter values for $\bar{\nu}_\mu \rightarrow \bar{\nu}_e$ were consistent with the ones coming from LSND [24].

Experiments SAGE (Soviet-American Gallium Experiment) [25] and GALLEX (Gallium Experiment)[26] have resulted with the so called Gallium anomaly. They were studying solar neutrino flux based on the inverse beta decay reaction. Investigating the ν_e flux coming from the ^{51}Cr and ^{37}Ar sources, used for calibration, they obtained the event rate $\sim$ 15 % lower than expected [27]. However, statistical significance of these measurements was not sufficient to draw the definite conclusions.

The last, so called reactor anomaly, reflects the fact that the measured reactor flux was found to be smaller than the predicted one [28]. Many precise measurements are now performed at various reactors to clarify this issue.

All above-mentioned experiments were studying neutrino oscillations over short distances. One possible explanation of these anomalies happening while shrinking down the distance between a neutrino source and detector is the existance of a hypothetical sterile fourth neutrino separated from the three standard neutrinos by a squared mass difference of one to a few eV^2.

All these anomalies require to be explained. Therefore, searches for sterile neutrino (or neutrinos) are one of the most important topics in neutrino physics. Among others, the large accelerator neutrino experiment at Fermilab (SBNE) has been designed in order to hunt for the definitive evidence or exclusion of the LSND-like sterile neutrinos.

The discovery of sterile neutrinos would open a rich field of experimental and theoretical studies of their properties, their mixing with the Standard Model neutrinos and their role in particle physics in astrophysics and in cosmology.

2 Liquid Argon detectors in neutrino studies

A number of innovative experiments dedicated to rare event physics, such as direct searches for dark matter particles or neutrinoless double beta decays, are using liquefied noble-gases, particularly Liquid Argon (LAr) and Liquid Xenon (LXe), as detection media. Among many advantages of noble liquids, from the detection point of view, the most important ones are high scintillation and ionisation yields, possible long drift paths of ionisation electrons and feasible large detector masses. However, in neutrino studies huge detector masses are required and those experiments are using only LAr as an active detector volume. Liquid Argon is sufficielntly dense and much less expensive than LXe and therefore is the only adequate noble liquid for huge volumes.

The first neutrino experiment based on the large Liquid Argon detector was the Imaging Cosmic and Rare Underground Signals (ICARUS) experiment with the detector (T600) filled with 600 tons of LAr. It was located in the underground Gran Sasso laboratory. Recent developments in LAr technology offer new opportunities to study neutrinos with unprecedented precision. Therefore, there are a few other LAr detectors which are presently either operating or under construction. In particular, the planned short- and long-baseline neutrino programmes at FNAL dedicated to neutrino oscillation studies are based on the LAr detection technology.

In this chapter the following issues will be described: the principles of particle detection in LAr, the accomplished ICARUS experiment in Gran Sasso, the Short Baseline Neutrino Experiment (SBNE) under construction and commissioning at FNAL and the future long baseline neutrino programme LBNF - DUNE at FNAL.

2.1 Principles of particle detection in LAr

When charged particle is passing through the Liquid Argon volume two processes occur: ionisation and scintillation light emission. The average energy required to produce an electron - ion pair in Argon is $W_{ion} = 23.6$ eV, whereas the average energy for a scintillation photon emission is $W_{ph} = 19.5$ eV. Both the emitted vacuum ultraviolet (VUV) scintillation light and the ionisation electrons, produced by charged particles are used to detect and identify these particles.

The excited or ionised Argon atoms which atom form excited Ar_2^* or ionised Ar_2^+ molecules (dimers) with another Argon.

The Ar_2^* excimer (excited dimer) decays radiatively:

$$Ar^* + Ar \rightarrow Ar_2^* \rightarrow 2Ar + \gamma, \tag{3}$$

while the Ar_2^+ state can recombine with an electron, falling into the Ar_2^* state which decays radiatively:

$$Ar_2^+ + e^- \rightarrow Ar_2^* \rightarrow 2Ar + \gamma. \quad (4)$$

The recombination process occurs close to the particle trajectory where free electrons and positively charged ions from the ionisation process are available in big quantities. The recombination reduces the ionisation electron signal causing a worse performance of the detector. In order to minimise this effect the electrons have to be immediately driven to the anode. Therefore, a strong electric field is required to be applied to the LAr volume of the detector.

The scintillation light emission and the ionisation processes are complementary and their relative weight depends on particle energy and on how strong is the applied electric field.

The increase of the electric field reduces the effect of recombination, hence also the scintillation light emission. The free electron yield due to ionisation increases with an field value while the photon yield due to scintillation decreases. However, for both processes saturation occurs for fields higher than $\sim$ 10kV/cm. At the typical value of 500 V/cm both processes have to be taken into account.

The signal from ionisation electrons allows a precise 3D reconstruction of the charged particle paths, while the fast scintillation signal provides the t_0 time of a drift of those electrons as well as a rough information about the particle location in other two coordinates.

The experiments dedicated to neutrino and rare event physics studies require the capability to discriminate between various particles interacting in the detector volume, e.g. for the efficient background reduction.

Scintillation light in Liquid Argon has a wavelength of about 128 nm and is characterised by two distinct decay times: a fast component (single eximer) and a slow component (triplet eximer). The mean lifetime of the single eximer state is 6 ns. The triplet eximer state has a significantly longer mean lifetime of 1.5 μs. The decay time of the slow component increases with the increasing purity of Argon, so it can be also used as a measure of its purity. Impurities within Liquid Argon can absorb emitted ultraviolet (UV) photons, leading to a loss of the light collection. In addition, impurities in LAr can also impede the drifting electrons or quench Argon excimers, leading to a loss of both light and charge collection. Thus, the efficient purification system of LAr is very important.

The main properties of Argon are summarized in Table 1. Argon is the third most common gas in the Earth's atmosphere and for that reason can be easily obtained in large quantities by cryogenic fractional distillation of air. Pure LAr is an almost ideal material for the Time Projection Chamber (TPC), because it is sufficiently dense to offer reasonably short radiation and nuclear interaction

LAr property	value
Atomic number, mass	18, 40
Atomic weight	39.948 m_u
$\langle Z/A \rangle$	0.45059
Concentration in air	0.934 %
W_{ion} (1 MeV e^-)	23.6 eV
Energy loss $\langle dE/dx \rangle$ (minimum ionising particle)	1.519 MeV cm^2/g
W_{ph} (1 MeV e^-)	19.5 eV
Photon yield scintillation (at 128 nm) 0-field	$\sim 4.0 \times 10^4$ ph/MeV
Decay time constants	$\sim$ 6 ns (23 %)
	$\sim 1.6\ \mu$ s (77 %)
Radiation length	19.55 g/cm^2
Nuclear interaction length	117.2 g/cm^2
Dielectric constant at 128 nm (550 nm)	1.9 (1.5)
Refractive index at 128 nm (550 nm)	1.38 (1.23)
Rayleigh scattering length at 128 nm (550)	0.9 m (10^3 m)

Table 1: LAr chemical and physical properties [40].

lengths, it does not attach ionisation electrons and hence permits long drift-times, it has a high electron mobility, it is easy to obtain and to purify, it is cheap.

2.2 ICARUS experiment in the underground Gran Sasso laboratory

The ICARUS (Imaging Cosmic And Rare Underground Signals) experiment in the underground Gran Sasso laboratory pioneered the use of LAr detectors for neutrino studies. T600 Liquid Argon time projection chamber with a total Argon mass of 600 t is the largest LAr imaging detector built up to now. The design and assembly of the ICARUS T600 LArTPC relied on industrial support and represented the application of concepts matured in laboratory tests. The ICARUS T600 detector was installed in hall B of the Gran Sasso underground laboratory. The 2400 meters of rock above the experimental halls provides a very efficient cosmic ray shielding.

The ICARUS experiment belonged to the European programme of neutrino oscillation studies at the CNGS (CERN to Gran Sasso) beam, approved in 1998.

The CNGS ν_μ beam was produced at CERN and directed towards the Laboratori Nazionali del Gran Sasso (LNGS), 732 km away. The beam resulted from the collisions of protons with nucleons in a graphite target. The products of such interactions, mainly pions and kaons, in most cases decay to ν_μ and muons. The CNGS neutrino facility provided an almost pure ν_μ beam peaked in the energy range $10 \leq E_\nu \leq 30$ GeV, with a contamination from muon anti-neutrino of about 2% and an electron neutrino component of less than 1% [29].

The main goal of the CNGS scientific programme was a direct observation of the ν_τ CC interactions for ν_τ appearing in the ν_μ beam on the way from CERN to Gran Sasso due to the $\nu_\mu \leftrightarrow \nu_\tau$ oscillations. Although the disappearance of the atmospheric ν_μs, discovered in the SuperKamiokande experiment, was interpreted this way, a direct proof with a sufficient statistical significance was too difficult for the water Chenerknov Super Kamiokande detector. The direct observation of the ν_τ CC interactions required the identification of the charged τ lepton in the final state of the ν_τ CC interactions - experimentally very demanding.

The OPERA (Oscillation Project with Emulsion-tRacking Apparatus) experiment, equipped with almost 2 ktons of emulsion chambers, was especially designed for this purose and discovered the ν_τ appearance in the CNGS beam [30].

The T600 detector had operated at Gran Sasso from May 2010 to June 2013, taking both the CNGS neutrino beam and atmospheric data with an extremely high Argon purity and a good detector stability. During the period of 2010 - 2012, the detector had collected neutrinos corresponding to a total of 8.6 $\times 10^{19}$ 400 GeV protons-on-target with a recording efficiency exceeding 93 %.

The ICARUS approach to the $\nu_\mu \leftrightarrow \nu_\tau$ oscillation studies was to separate the ν_τ CC events from the background through kinematical criteria and very characteristic electromagnetic showers for electrons, with some of them coming from the τ lepton decays. However, there was no conclusive result concerning the $\nu_\mu \leftrightarrow \nu_\tau$ oscillations, mostly due to the too small detector mass and too short data taking period.

Despite the failure concerning the observation of the ν_τ appearance in the CNGS beam, the ICARUS experiment obtained a few valuable physics results.

The first one was related to the 2011 announcement of the observation of superluminal neutrinos by the OPERA experiment [31]. The ICARUS collaboration published a paper [32] in which it was indicated that the energy distribution of the neutrinos is not compatible with superluminal particles. In 2012 ICARUS directly measured the neutrino velocity [33] [34] which was in agreement with the speed of light and the special relativity theory. For the final analysis 25 neutrino events were selected yielding an upper limit for the difference between the neutrino and the light time of flight:

$$\delta t = 0.18 \pm 0.69(stat.) \pm 2.17(sys.)ns, \tag{5}$$

corresponding to:

$$\frac{v - c}{c} = (0.7 \pm 2.8(stat.) \pm 8.9(sys.)) \times 10^{-7}. \tag{6}$$

Another important physics result, obtained in the ICARUS experiment, was a strong reduction of the allowed parameter space for the LSND anomaly [35].

Apart from physics results, the collected data had been used for the development of the analysis software, in particular the reconstruction program [36].

In 2014 the ICARUS T600 detector was moved to CERN for overhauling. In April 2017 the upgraded detector was transported from CERN to the FNAL near Chicago in the U.S. In 2018 it is expected to be put again in operation at FNAL at the Booster Neutrino Beam (BNB), for a definitive clarification concerning the existance of a new sterile neutrino state (ν_s) suggested by the LSND and MiniBooNE observations.

The successful operation of the ICARUS T600 detector opened the way to the construction of more advanced detectors and to larger detector masses up to tens of ktons as required to realise the next generation experiments for neutrino oscillation studies and searches for proton decays.

2.3 Short Baseline Neutrino Experiment at Fermilab

The Short Baseline Neutrino Experiment (SBNE) performed by a large international collaboration is an extensive experimental programme to search for the sterile neutrino and to study neutrino properties using the Booster Neutrino Beam line (BNB) at FNAL. The SBNE will make use of three Liquid Argon Time Projection Chambers (LArTPCs) exposed to the ν_μ and $\bar{\nu}_\mu$ beams of energy about 0.8 GeV at different distances from the target - SBND, MicroBooNE and ICARUS at 110 m, 470 m and 600 m respectively, as is shown in Figure 4. As mentioned above, the ICARUS T600 detector was the first successful large scale LArTPC to be exposed to a neutrino beam and to this point the largest LArTPC for neutrino physics. The Micro Booster Neutrino Experiment (MicroBooNE) detector is the largest LArTPC built in the U.S. and it has already started collecting data. The Short-Baseline Near Detector (SBND) is being developed by an international team with experience from the ArgoNeuT, MicroBooNE and Liquid Argon prototypes for the LBNE project.

The main purposes of the SBNE experiment are searching for the LSND-like sterile neutrino oscillations, following up on the MiniBooNE additional low energy excesses and making precision measurements of neutrino interactions with Argon.

The hints of new physics, reported by LSND and MiniBooNE, are related to the oscillations with Δ m^2 $\sim$ eV^2, i.e. significantly different than the ones for the oscillations of atmospheric and solar neutrinos. This result can point to the existance of one or more new sterile neutrino states with masses in the eV scale. Both size and locations of the three SBNE detectors allow the characterisation of the beam before oscillations in the SBND detector and the measurements of

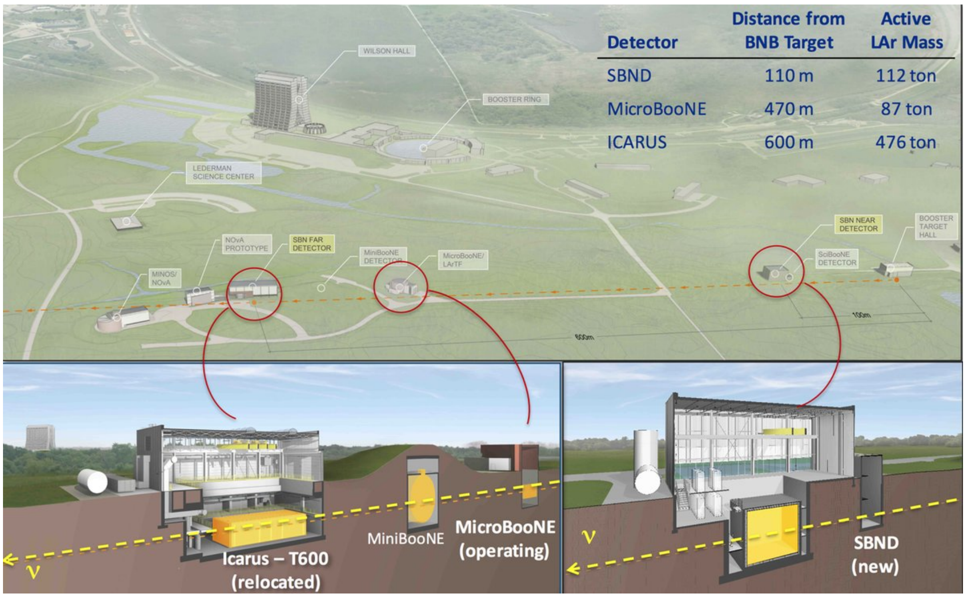

Figure 4: Layout of the three LAr TPCs of SBNE and their positions at the BNB line [37].

the ν_e ($\bar{\nu}_e$) appearance and ν_μ ($\bar{\nu}_\mu$) disappearance in the the MicroBooNE and ICARUS detectors.

The future projects, including long-baseline neutrino experiments, will need significant improvements of the neutrino intraction model to make precise measurements of neutrino oscillations. In SBNE, it will be possible to achieve the highest precision cross section measurements of $\nu_\mu - Ar$ and $\nu_e - Ar$, as well as $\bar{\nu}_\mu - Ar$ and $\bar{\nu}_e - Ar$, scatterings from about 100 MeV to 1 GeV as each of the three SBNE detectors will register neutrino interactions coming from the BNB beam. The ICARUS T600 detector will also be able to register neutrinos from the NuMI beam.

Finally, SBNE is an excellent opportunity for further developement of the LAr TPC detector technology for the future long-baseline neutrino project DUNE at FNAL while exploiting its expected performance to investigate open questions in neutrino physics today.

The MicroBooNE detector has already started the data taking, ICARUS after its refurbishment at CERN has been moved to Fermilab, while SBND is under construction and will begin taking data in 2019.

2.4 LBNF-DUNE long baseline project

LBNF - DUNE is a large future experimental project led by FNAL with contributions of physicists from all over the world. LBNF (Long Baseline Neutrino Facility) is an infrastructure which will include the world's highest-intensity neutrino beam produced at FNAL. DUNE (Deep Underground Neutrino Experiment) will be conducted with the near detector station installed at FNAL and the massive, cryogenic far detector station installed deep underground at

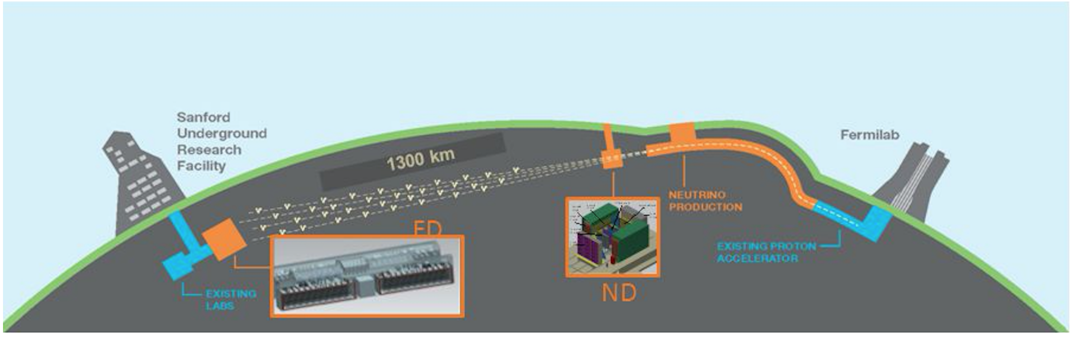

Figure 5: The scheme of LBNF-DUNE, hosted at Fermilab in Batavia with far detectors installed deep underground at the SURF [38].

the Sanford Underground Research Facility (SURF), 1300 km away from FNAL. The scheme of LBNF-DUNE is shown in Figure 5. The DUNE near detector will measure the energy spectrum and the composition of the neutrino beam before oscillations occur. Traveling with the speed close to the speed of light, the neutrinos will leave the Fermilab site, continue straight through the earth and arrive at SURF in South Dakota within a fraction of a second.

The main scientific goals of the experiment are precise measurements of the parameters that govern $\nu_\mu \rightarrow \nu_e$ and $\bar{\nu}_\mu \rightarrow \bar{\nu}_e$ oscillations as well as $\bar{\nu}_\mu \rightarrow \nu_{mu}$ and $\nu_\mu \rightarrow \bar{\nu}_\mu$ oscillations, mostly aiming at the charge-parity violating phase δ_{CP} measurement and the determination of the neutrino mass hierarchy.

The δ_{CP} value different from zero or π would mean the CP-violation in the leptonic sector, providing a possible explanation for the observed matter-antimatter asymmetry in the Universe.

Thanks to 1300 km baseline, the experiment will be sensitive to the matter effects which enable the determination of the neutrino mass hierarchy, i.e. answering the question whether the mass state m_3 is below or above the mass states m_1 and m_2.

Both the CP-violation and the matter effects lead to asymmetries in the $\nu_\mu \rightarrow \nu_e$ versus $\bar{\nu}_\mu \rightarrow \bar{\nu}_e$ oscillation probabilities. Those two asymmetries depend differently on the neutrino energies and this feature can be used to distinguish them. Liquid Argon detectors of the DUNE experiment will allow a precise determination of neutrino energies, so the neutrino spectra can be used. This in turn allows the determination of the CP-violation and neutrino mass hierarchy in the same experiment assuming separate optimisation towards each of those measurements. The statistical significance of 5σ, required in particle physics to recognise the discovery, should be possible for both measurements [39].

In addition, the experiment will search for proton decay in several important decay models, in particular $p \rightarrow K^+\nu$, prefered by the supersymmetric Grand Unification models. The DUNE scientific programme also includes the Supernova burst physics, if any Supernova explosion occurs during the lifetime of the

DUNE experiment.

The design of LBNF and DUNE is under preparation and the construction will start at FNAL in 2018.

3 ICARUS T600 detector

Technical aspects of the T600 detector are shortly discussed in this chapter. The description of basic detector elements for the already completed ICARUS experiment in the Gran Sasso laboratory is given in the first section. The main improvements introduced during the detector overhauling at CERN are presented in the second section. The requirements for its future use in the SBNE experiment at the FNAL are introduced in the third section.

3.1 Construction of the T600 detector

As shown in Figure 6 the ICARUS T600 detector consists of two identical, adjacent T300 modules, each one being an aluminium cuboid with internal dimensions of 3.6 m × 3.9 m × 19.6 m. Each T300 module houses an inner detector composed of two time projection chambers (TPC) with a common cathode, and each one equipped with an anode, a field-shaping system, monitors, probes and liquid argon scintillation light detection system. Each TPC anode consists of three parallel wire planes, which are held by sustaining frames mounted along the longest walls of the T300 module. The total number of wires and electronic channels in the T600 detector is 53248. Each T300 module is externally surrounded by thermal insulation layers.

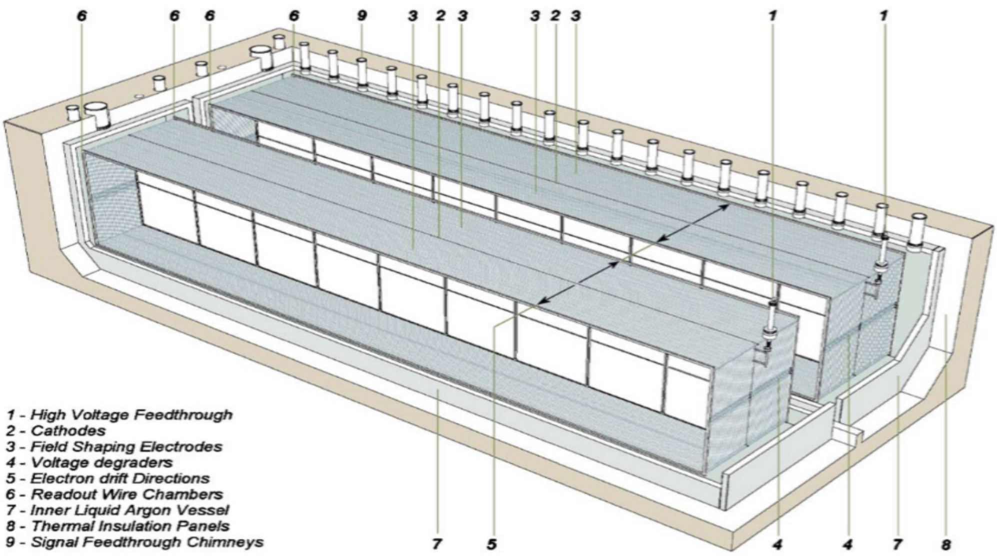

Figure 6: Schematic layout of the T600 detector [40].

The inner volume size of each of the two T300 modules amounts to 275.2 m^3 and the active volume size equals to 170.2 m^3. In each TPC between the cathode and the anode wire planes an uniform electric field is set in the LAr volume to allow the drift of ionisation electrons towards the anode wires. In the center of each T300 module the cathode plane is mounted at a distance of

1.5 m from the wires on each side. This distance represents the maximum drift path of the electrons. In order to set the required voltage on the cathode and for obtaining the uniformity of the field along the drift direction the HV system is built with an HV feedthrough and field-shaping electrodes. At the nominal voltage of 75 kV, corresponding to an electric field of 500 V/cm, the maximum drift time in LAr is about 1 ms.

On the top side of the cryostat there are exit flanges with cryogenic feedthroughs for the electrical connections of the wires and for all the internal instrumentation.

The technology of the LArTPC allows an almost undistorted transportation of ionisation electrons, produced along the tracks of charged particles, in the uniform electric field over macroscopic distances in a highly purified LAr.

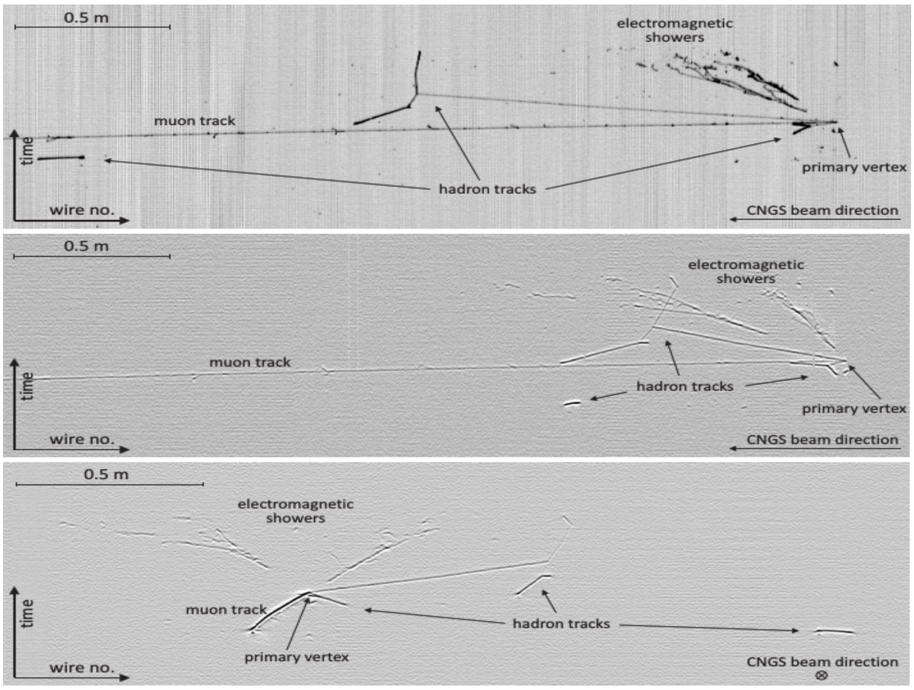

Figure 7: Data from CNGS ν_μ CC interaction in the ICARUS T600 detector; starting from the top: projective views in the Collection plane, Induction2 plane and Induction1 planes [41].

Ionisation electrons are detected almost undisturbed on the anode wires. The first two anode planes register induced signals and hence are called Induction1 and Induction2. The signal on the third wire plane, Collection, is formed by collecting the ionisation charge, which is also used for the calorimetric measurements. Orientations of the wires in the anode planes are $0°, +60°$ and $-60°$ with respect to Z coordinate along the beam, with 3 mm wire spacing in each plane. This allows to obtain projective views of the same event for all three wire planes with one coordinate related to the wires and the second one related to the drift time.

An example of the neutrino interaction recorded at all three wire planes is shown in Figure 7. The horizontal wires of the Induction1 plane form the projection on XY plane and give the frontal view of the event while the Collection and Induction2 planes form YZ projections and give the top views of the event seen at two different angles.

After the 3D reconstruction based on the three projective views one obtains a precise spacial imagining of events registered in the detector fiducial volume as well as very good calorimetric measurements. Aming other things, this allowed a highly-efficient electron and γ discrimination and therefore of minimisation the main source of background for electron-like neutrino events coming from neutral current interactions with a π_0 production.

In order to reduce the concentrations of electronegative impurities like O_2, N_2, H_2O, affecting ionisation electrons during their drift to the anode wires, a continous gas (2.5 m^3/h) and liquid (100 m^3/d) recirculation with a standard commercial Hydrosorb/Oxysorb filters had been used. It kept the impurity levels far below the value of 0.1 ppb - O_2 equivalent allowing the travel of ionisation electrons almost undisturbed through the entire drift volume. During the LNGS run the obtained maximum value of electron life-time was equal to 16 ms corresponding to an impurity concentration lower than 20 ppt O_2 equivalent. This result represents a fundamental step towards the construction of a new generation of detectors, with drift paths many meters long.

3.2 T600 detector overhauling at CERN

The ICARUS T600 detector was transported to CERN at the end of 2014 for overhauling and refurbishment oriented towards its future use in the SBNE experiment. As it was mentioned before, the main goals of SBNE are studies of the short-baseline neutrino oscillations in the 1 eV mass range, making a precise measurements of the neutrino-argon interactions and future development of the LArTPC technology.

In order to fulfil the requirements of SBNE, a proper refurbishment of the detector had to be undertaken. The WA104 programme at CERN was conceived for the required refurbishment operations.

During its operation in the underground Gran Sasso laboratory the detector was in the low background conditions. At FNAL the T600 will operate at shallow depths. Several additional cosmic muons ($\sim$ 12) will be present during the 1 ms drift time, causing problems for the track reconstruction.

In order to identify cosmic rays entering the detector, cosmic muon tagging system of about 1000 m^2 is needed. Available technologies to realize this system include either resistive plane chambers or scintillator slabs read out by photomultipliers or silicon photomultipliers.

Moreover, the light detection system for sensing the light emitted in LAr at 128 nm by ionising particles had to be upgraded in order to allow a more precise event timing and a better event localisation, as well as the exploitation of the bunched beam structure of BNB at FNAL (1.15 ns every 19 ns) to reject out-of-bunch cosmics.

Among refinement activities the new light collection system represented a fundamental task [42]. This system will be used for triggering and timing purposes. Light pulses collected by photomultiplier tubes, in coincidence with the beam spill gate, will be used as a trigger signal similarly to the experiment in Gran Sasso. In addition, for non-beam events scintillation light provides the information about the t_0 time of each event inside the TPC. By combining the t_0 information with the drift electron velocity the precise event coordinate along the drift direction can be determined.

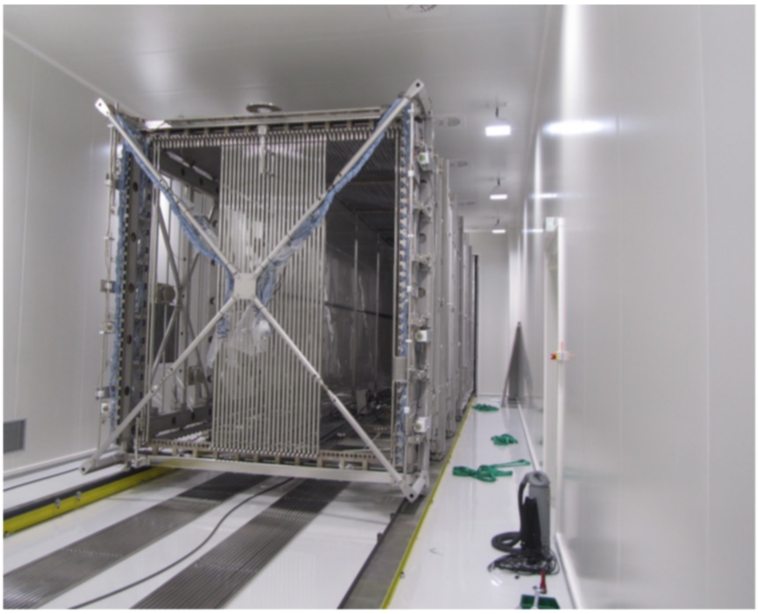

Figure 8: One T300 module of the T600 detector inside the clean room at CERN Bldg. 185 [42].

The renovation was held for each T300 module separately in a dedicated clean room at CERN Bldg 185, as it is shown In Figure 8. The refurbishment operations, in a framework of the WA104 programme at CERN, included:

- construction of the new cold vessels and the new passive thermal insulation;
- refurbishing the cryogenic and purification equipment;
- flattening of the existing cathode panels in order to obtain their better planarity;
- improvement of the existing warm electronics;

- replacement of the old light collection system with the new one based on 360 PMTs;

The WA104 programme at CERN also concerns the further R&D activities related to the future LBNF programme at FNAL such as studies of the magnetization of the LArTPCs and a possibility of the replacement of PMTs with photodetectors insensitive to external magnetic fields, such as Silicon Phtotomultipliers (SiPMs).

3.3 Future use of the T600 detector in the SBNE experiment at FNAL

The extensive overhauling that took place at CERN will allow the use of the ICARUS T600 detector at the FNAL upcoming SBNE experiment, approved for five years of runing. The T600 detector is forseen to act as a far detector located at 600 m distance from the BNB primary target, providing the signal for the oscillation analysis of the experiment. In addition, the detector will also be able to take data with the NuMI beam dedicated to the NOvA (NuMI Off-Axis ν_e Appearance) experiment at FNAL.

As mentioned before, in SBNE the operation of all the detectors will take place at shallow depths. Therefore, in the T600 detetctor 12 muon tracks are expected in the 1 ms drift readout window, as estimated during the 2001 test run performed in an experimental hall in Pavia [40] .

Therefore, the work on the design and construction of the dedicated Cosmic Ray Tagging (CRT) system has started. The CRT detection system will consist of two layers of scintillator panels, for XY position reconstruction, with embedded optical fibres read out by SiPMs. The panels will be installed and integrated in the outer supporting structure (warm vessel) of the T600 [43].

The combination of timing from both the CRT panels and internal PMT system will allow an efficient recognising of cosmic muon tracks and distinguishing them from long muon tracks in ν_μ CC beam events.

4 Light collection system of the ICARUS T600 detector for the SBNE experiment

As explained in Chapter 2., charged particles crossing the active volume of the detector are depositing energy in LAr by excitation and ionisation of its atoms. This leads to a scintillation light emission and free electron production, respectively. Additional scintillation light occurs because of electron-ion pairs recombination, which is inversely proportional to the strength of the electric field applied to the detector. Therefore, free electron yield increases with higher value of electric field, while photon yield decreases.

The scintillation light in LAr arises as a consequence of the deexcitation of the molecules (Ar_2^*). It is characterised by photons from a VUV spectrum with λ of about 128 nm and by yield of the order of 10^4/MeV. This is a very fast signal and propagates with a negligible attenuation throughout the TPC volume, hence providing an absolute time measurement (t_0) and a trigger for ionising events occurring in LAr.

To extract physics information from the scintillation light a suitable light collection system is required. The ICARUS T600 light collection system has been extensively upgraded at CERN in a framework of the WA104 project. Outdated PMTs were replaced with new photomultipliers and their total number was increased to 360 devices. They have been placed behind the 4 sets of wire planes, 90 units per each TPC chamber. Scintillation light signal collected by PMTs, in coincidence with the beam spill gate, produces a trigger signal. In addition, the light provides the timing, t_0, of each event in the active volume. The combination of the t_0 with the drift electron velocity is allowing a precise determination of the event coordinate along the drift direction.

4.1 Requirements of SBNE

As it was mentioned before, the ICARUS T600 detector during its operation in the deep underground LNGS laboratory had operated in the low background conditions, i.e. with practically no cosmic muons entering the detector during the readout time of 1 ms following the beam trigger. In the SBNE experiment the detector will be placed at a shallow depth (of 3 meters underground). This means that it will be subjected to a huge background of cosmic muons.

A huge rate of 0.83 $\times 10^6$ cosmic muons per year will be produced in coincidence with the beam trigger window of $\sim$ 1.6 μs. In the measurements at the Earth surface carried out by the ICARUS collaboration [40] it was found that during the 1 ms long readout window $\sim$ 12 cosmic muon tracks will cross the whole ICARUS T600 detector. Therefore, it will be essential to precisely link timings of all elements of the image with their own specific delays with respect to the trigger.

The idea of studying oscillations caused by sterile neutrinos is based on the search for a signal of single electrons or positrons produced in the interactions of muon neutrinos or antineutrinos from the accelerator beams. Such electrons or positrons can also be produced by high energy cosmic muons creating secondary showers with similar energies. At the neutrino energy range of the FNAL BNB, the actual contamination of the ν_eCC will occur at the rate of $\sim$ 500 ν_eCC events per year while the expected LSND-like oscillation signal will contain a few hundred of the ν_eCC interactions.

Thus, it was concluded that the ICARUS T600 detector has to be upgraded in order to deal with the cosmic muon events being so frequent. Aiming of the background reduction, the detector required the following changes:

- the realisation of a new light collection system for a better timing and localization of individual events in the detector,
- the design and construction of a cosmic tagging system to veto cosmic muons entering the detector.

It is fundamental to localize in space the signals related to the neutrino beam induced events in order to perform a high quality selection and a good 3D reconstruction of these events. It was estimated that the new light collection system has to be sensitive to the energy down to $\sim$ 100 MeV and it has to be able to localize the track associated with the light pulse with a precission higher than 1 m in the Z coordinate (See Figure 9) along the beam direction, allowing an efficient cosmic muon rejection.

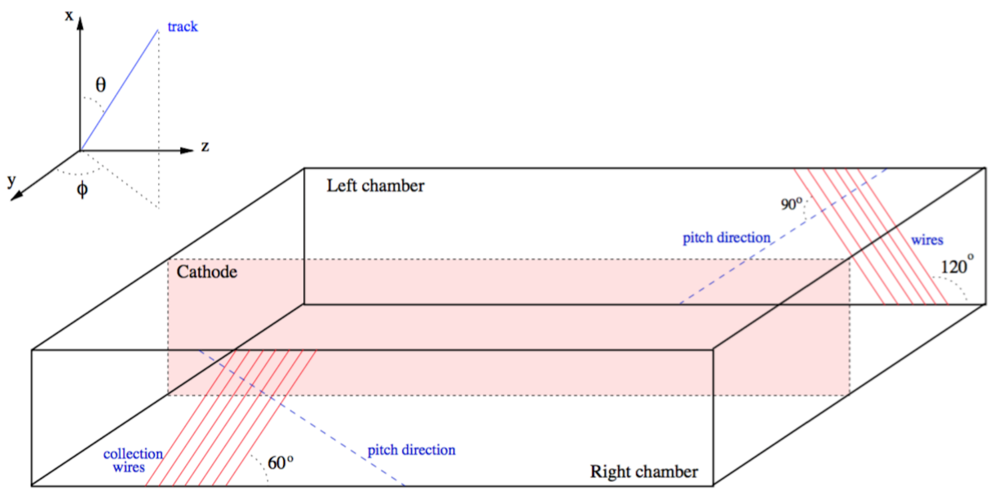

Figure 9: T300 module in the ICARUS detector coordinate system [40].

Figure 10 presents the light collection system of ICARUS for one plane of PMTs with their positions pictured in the ICARUS coordinates system.

Simulations showed that in order to reach a FWHM of 19, 24 or 38 cm in the Z coordinate the number of 90, 54 or 27 PMTs per plane is required.

The spatial reconstruction performence at the light collection system in terms of a fraction of the reconstructed events and a spatial error is illustrated in Figure 11. A better performance was obtained for geometries with a higher numbers of PMTs. The best results are obtained for 90 PMTs - 8" configuration with an additional requirement of a signal above 30 photoelectrons. This configuration presents a better reconstruction capability than the one with 210 PMTs - 5".

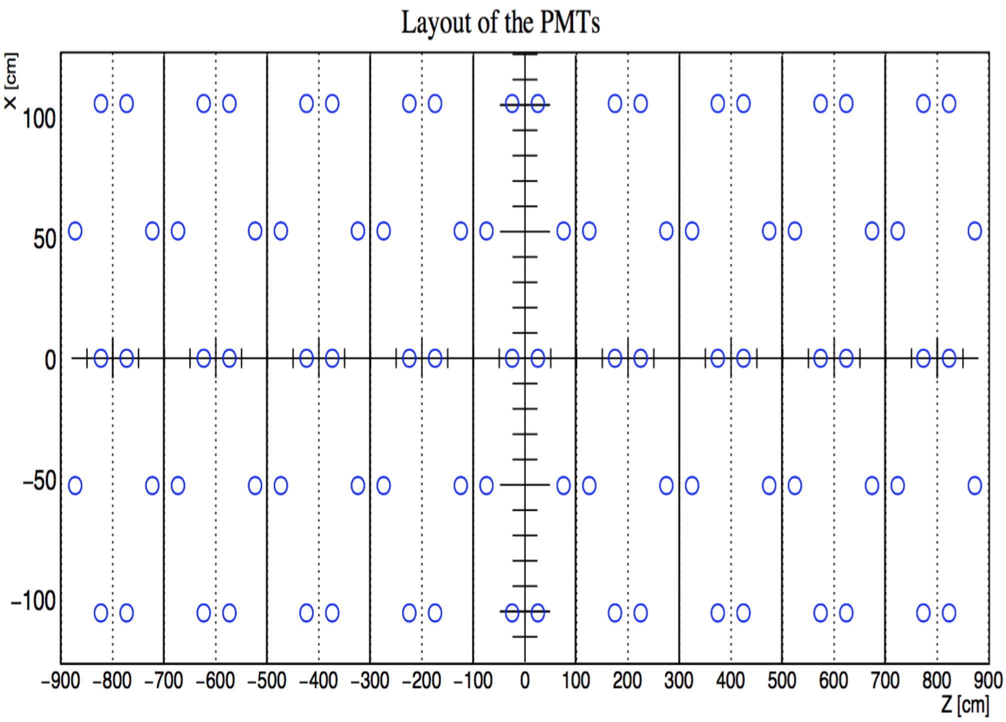

Figure 10: The PMT layout for 9 sectors of a single TPC chamber in the ICARUS coordinate system.

For additional rejection of cosmic muon background, while exploiting the BNB bunch structure lasting 1.15 ns every 19 ns, the time resolution of the order of one nanosecond will be required. Hence, an accurate time calibration of the PMT system is needed.

Achieving these tasks requiers very good PMT response and a small transit time spread to ensure high signals and a low noise level. The requirements are as follows:

- Several dynode stages to allow a gain of $> 10^7$ at cryogenic temperature of 87K;
- 1750 V as the maximal applied voltage for the gain of 10^7;

- Response deviations from uniformity lower than 10%;
- Single Electron Response (SER) peak-to-valley ratio higher than 2 for the gain 10^7;
- Response linearity up to 150 photoelectrons (phe);
- Transit time spread smaller than 2.5 ns;
- Maximal dark count rate of 5 kHz for 0.25 phe threshold.

As already explained, the realisation of the cosmic ray tagging system, which is placed outside the ICARUS T600 detector and serves for automatic identifcation of entering charged tracks, will greatly facilitate the reconstruction and identification of cosmic muon tracks.

Applying both the cosmic ray tagging system and the information based on the light collection system should give a strong reduction of the cosmic ray background.

4.2 Layout of the ICARUS light collection system

The prompt scintillation light emitted in LAr along the trajectory of the charged particle is used to establish its t_0 value. It represents a fundamental part of the trigger system for ionising events which take place in the detector active volume. Many extensive R&D studies performed in the past confirmed that photomultiplier tubes are dealing well with collecting light produced in LAr.

The realisation of a new light collection system is a fundamental task in order to reject the expected huge cosmic background to provide the triggering of the signals, to enable fast spatial localization of neutrino beam associated events and a preliminary selection of events based on characteristics of the induced light signals. Therefore, it requires the sensitivity to the deposited energy below 100 MeV, the time resolution of about 1 ns and the high granuality.

To select the most suitable PMTs to fulfil these requirements several tests were carried out [44]. The selection was made among three large area (8' inch) PMTs: Hamamatsu R5912 MOD, Hamamatsu R5912-02 MOD and ETL 9357 KFLB, by studying the performance of each device at both room and cryogenic temperatures. All three models have borosilicate glass windows and bialkali photocathode with platinum undercoating to restore photocathode conductivity under the cryogenic conditions. In order to make the PMTs sensitive to the photons from VUV range the sanded photocathode window is evaporated with a proper wavelength shifter, which in that case is tetraphenylbutadiene (TPB). The measurement of Quantum Efficiency (Q.E.) in the VUV region was obtained with the usage of a McPherson 234/302 VUV monochromator, equipped with a Mc Pherson 632 Deuterium lamp [46]. The cryogenic conditions were realized by immersing the PMTs directly in a liquid N_2 (T = 77K) and the results were aquired after few days of rest.

Final results of tests for all three types of PMTs are given in Table 2. All the measured parameters of each PMT model were compatible with what is reported by the manufacturer. The rise time represents the time needed for the output pulse to rise from 10% to 90% of the peak when the photocathode is illuminated by a light pulse of very short duration. The shortest rise time was measured for ETL 9357KFLB, however, the Hamamatsu R5912 model rise time is longer only by 0.3 ns. Transit time was very short for Hamatsu R5912 model. The model with 14 dynodes presented the highest Dark Current value. The models provided by Hamamatsu show better Quantum Efficiency than the ETL 9357KFLB one.

	Hama R5912	Hama R5912-02	ETL 9357KFLB
no. dynodes	10	14	12
Gain (typical)	10^7 (at 1500V)	10^9 (at 1700V)	10^7 (at 1500V)
Rise Time (ns)	3.8	4	3.5
TTS (FWHM ns)	2.4	2.8	4
Dark Current(nA)	50	10^3	10
Q.E.at 390 nm (%)	25	25	18

Table 2: The comparison of three PMT types [46].

Although all three models marked good photocathode uniformity and a linear behaviour, the Hamamatsu R5916-MOD PMTs were chosen because of their best performance at the cryogenic temperature.

The new light collection system of the ICARUS T600 detector is made of four planes of PMTs, with 90 units each. Figure 12 presents the scheme of the placement of the 90 PMTs on the module wall.

All 360 PMTs are mounted on the wire chamber frames placed 20 cm behind the wire planes of each TPC, at 5 mm distance from the wires of the Collection plane. Each unit is located on a dedicated structure, which provides the support of the PMT in the correct position and orientation and prevents the electrical interference with the wire planes by means of additional screening grids. In addition, each support holds up a 50 μm optical fibre in front of the PMT sensitive surface, allowing for the gain and timing equalisation by means of an external laser. Figure 13 represents a CAD drawing of three TPC sectors with the PMTs and their support structers represented by circles and rectangles. Figure 14 shows a small part of the T300 module with installed PMTs, when located in the clean room at CERN.

A more detailed information about the ICARUS T600 light collection system is given in Appendix to this paper. In particular, the positions of all 360 PMTs

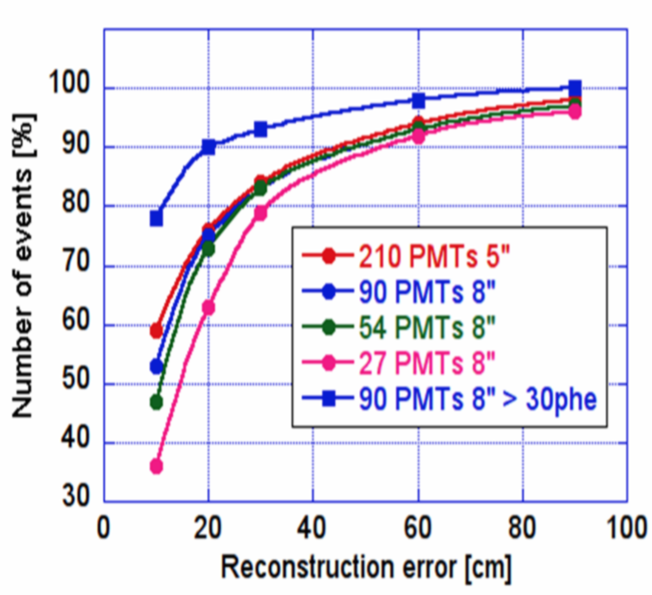

Figure 11: Monte Carlo evaluation of the spatial reconstruction capability in terms of a fraction of reconstructed events and of the spatial error for different PMT deployments and for the 90 PMTs - 8" configuration with a selection of signal above 30 photoelectrons [45].

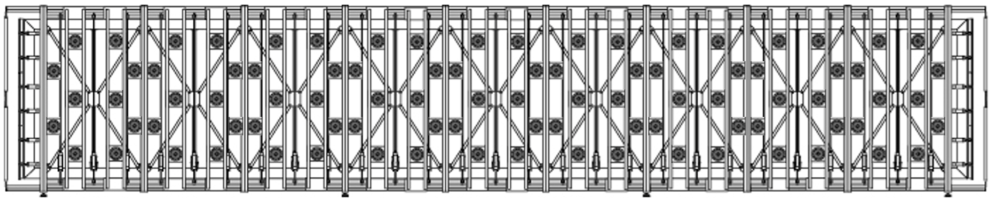

Figure 12: The representation of the T300 module with the chosen configuration of 90 PMTs [45].

in the ICARUS coordinate system are defined and the naming and numbering conventions are presented. For each PMT position the PMT serial number is given together with indeces of the connected HV cable, signal cable and optical fibre.

4.3 PMT characterisation

The simplified scheme of a typical PMT is illustrated in Figure 15. The PMT is converting a weak scintillation light signal into an usable electrical pulse without adding a big amount of random noise to the signal. It consists of two major elements, namely a photosensitive layer, called the photocathode, coupled to an electron multiplier structure. The incident photon is absorbed by the photocathode and its energy is used for a photoelectron emission from the photocathode through the photoelectric effect. The photocathode is converting as many of the incident light photons as possible into low-energy electrons. Photoelectrons produced by the photocathode serve as a current pulse, however, typically only a few hundred photoelectrons may be involved in an electrical sig-

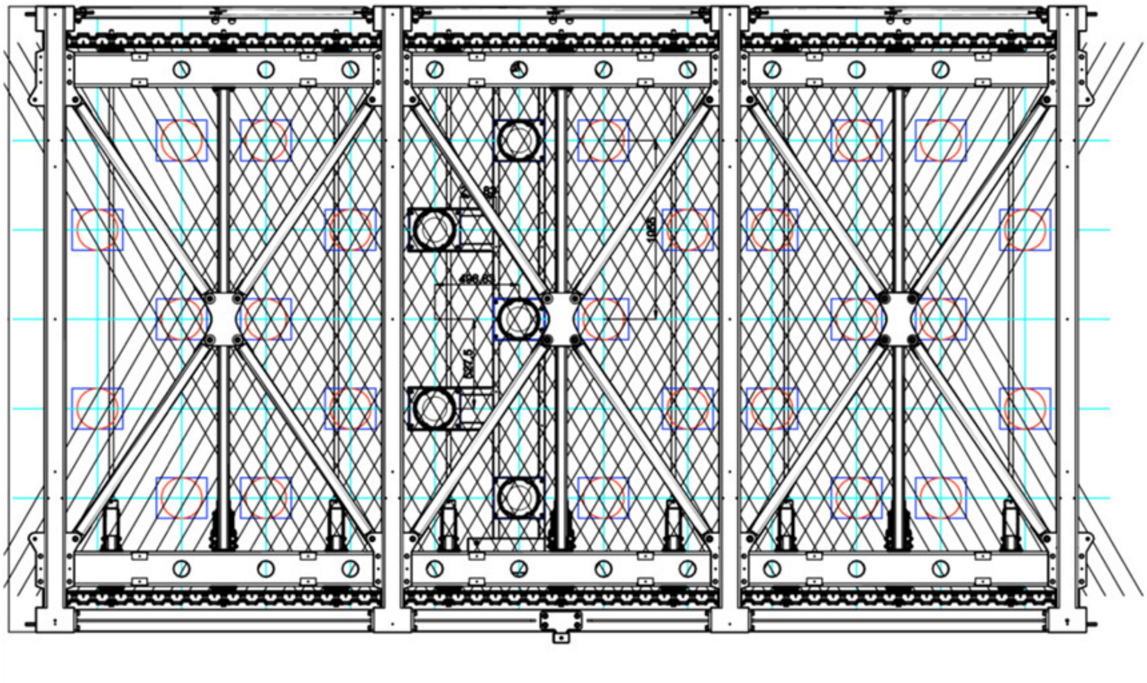

Figure 13: The layout of the light collection system in ICARUS T600, where the rectangles with red circles inside them represent the installed PMT.

Figure 14: Part of the ICARUS T600 module with the installed PMTs.

nal, so their charge is too small to serve as a convinient signal to be registered. Therefore, the electron multiplier, composed of dynodes, is used to provide an efficient collection geometry for the photoelectrons and to significantly enhance their number. Photoelectrons produced by the photocathode are accelerated by applied electric field towards a first dynode, from where the secondary electrons are released. Each of these electrons unleashes successive electrons from subsequent dynodes. As a result, a typical input scintillation pulse will give rise to about $10^7 - 10^{10}$ electrons, which is the output charge signal collected at the anode or the output stage of the multiplier structure.

The intensity of the output signal is usually reliant on the number of incident photons on the photocathode as well as on their energies. Thus the PMT sensitivity strongly depends on the wavelength of radiation spectrum reaching the photocathode.

In addition to the generated relevant signal there is also the noise fraction generated by the PMT. The major source of the noise is the so called dark current produced by the electrons emitted from the dynodes and photocathode as a consequence of thermoelectric effect.

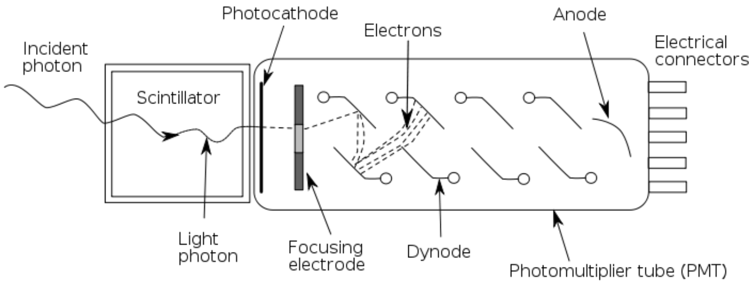

Figure 15: The simplified structure of a typical photomultiplier tube.

As it was menstioned before, the new PMT type installed in the ICARUS T600 detector is Hamamatsu R5912-MOD with 8 in. diameter. The feature window of this model is made of borosilicate glass. It contains 10 dynodes and a bialkali photocathode (K_2CsSb) with platinum undercoating to restore the photocathode conductivity at cryogenic temperatures.

The scintillation light emitted by particles in LAr is characterised by photons with a wavelength $\lambda = 128$ nm. This wavelength is too short for penetrating through the glass enclosure of the PMT. Thus, it is necessary to convert this light to the light with a longer wavelength (~ 500 nm) through depositing a special waveshifter on the photocathode. All the PMTs were evaporated with a proper fluorescent wavelength shifter reemitting the visible light. The uniform thickness of ~ 200 g/cm^2 of TPB was deposited on the sensitive surface of each device by using a dedicated evaporation system. The main characteristics of the Hamamatsu R5912-MOD PMTs are reported in Table 3.

As it is shown in Figure 16, a proper base circuit was installed at each PMT in order to supply the high voltage for the photocathode grids, dynodes and anode, and to make possible the signal readout directly from the anode.

The base circuit is entirely passive, and it is fabricated with the SMD (surface-mount device) resistors and capacitors, all tested at cryogenic temperatures. The bases were directly welded on the PMT flying leads. Two independent cables are mounted in order to provide the device with the high voltage and to read out the anode signal.

Spectral Response	300 ÷ 650 nm
Window Material	Borosilicate glass (sand blasted)
Photocathode	Bialkali with Pt under-layer
Max suppy voltage (anode-cathode)	200V
Photocathode Q.E. at 420nm	15 ÷ 16 %
Typical Gain	10^7 at 1500 V
Nominal anode pulse rise time	3.6 ns
Nominal P/V ratio	2.5
Max. dark count rate	$5000s^{-1}$
Nominal electron transit time	54 ns
Max. transit time variation	2.5 ns
Pulse linearity variation	± 10% up to 150 phe

Table 3: The main PMT features and acceptance requirements.

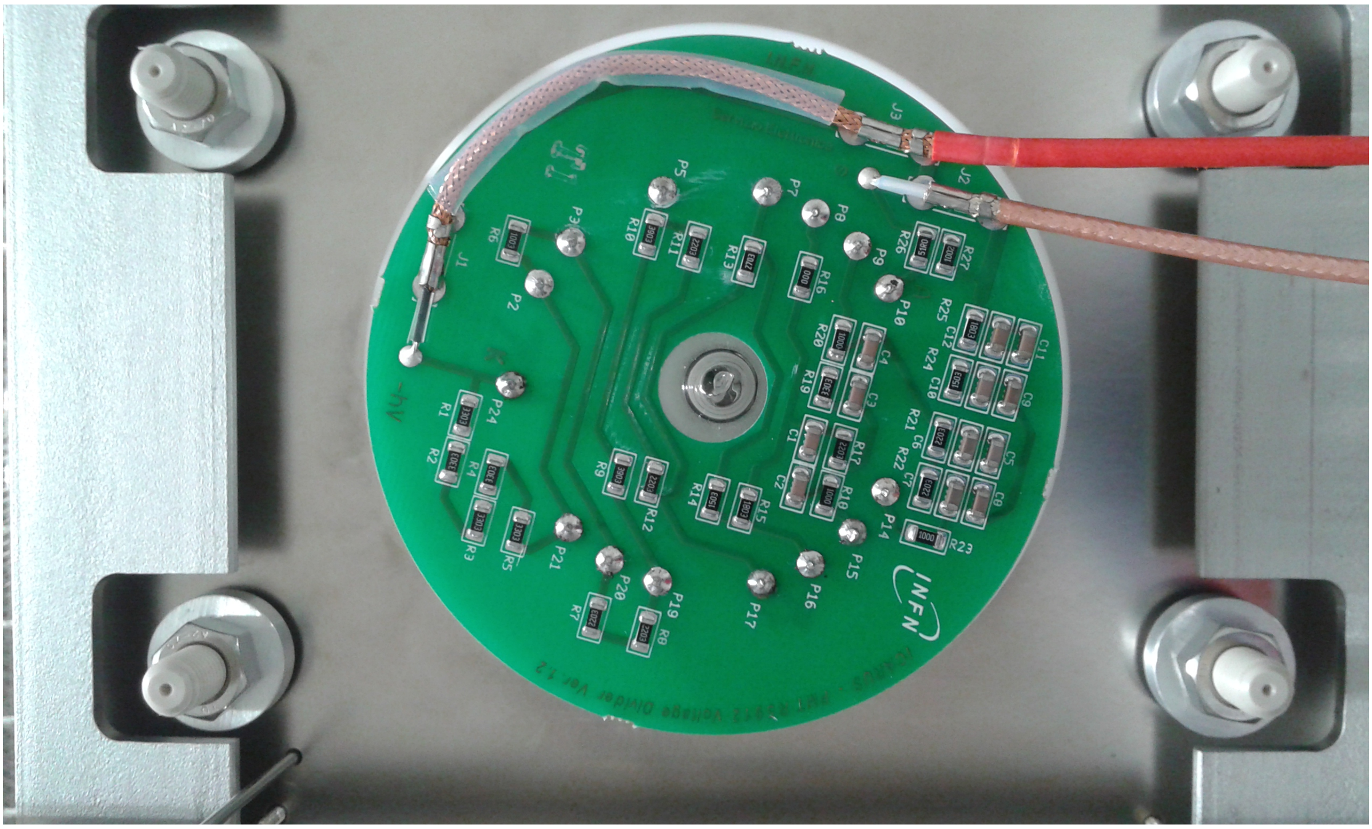

Figure 16: Base circuit installed at a PMT.

5 PMT tests and results

A complete set of 400 PMTs (20 PMTs from pre-series, first batch of 80 PMTs and 100 PMTs in each of the other three batches), including a 10 % of spare units, were sent by Hamamatsu to CERN. Each unit was tested before the installation in the ICARUS T600, to verify its compliance with the required functioning specifications given in Table 3. In particular, all the PMTs were tested at and 60 units were also characterised at cryogenic temperature of 87K, in a liquid argon bath. Some additional mechanical tests at cryogenic temperature were carried out in the factory for all the PMTs. Measurements were carried out in dedicated areas at CERN, where a dark-room and a cryogenic test facility were set up.

Tests at room temperature conditions were carried out in a dark room, where the 16 PMTs in parallel were measured. In a contiguous electronic workshop, a laser diode was operated to produce fast light pulses at 405 nm and 1 kHz repetition rate. Light intensity was controlled by using the calibrated optical filters mounted on two-wheel supports. The light was focused on the PMT windows by means of 100 μm optical fibres. The characterisation at room temperature was carried out using an electronics set-up in which the PMT output was integrated by means of the CANBERRA 2005 charge preamplifier and shaped by means of the ORTEC 570 amplifier. The output distribution was recorded by means of a multichannel analyzer.

Tests at cryogenic temperature were carried out in building 182. In order to obtain experimental conditions similar to those in the real apparatus, PMTs were directly immersed in liquid argon (T = 87 K) inside a dewar (1 m in diameter and 1.5 m high), allowing the simultaneous bath of 10 PMTs. The internal illumination was achieved by means of a single 100 μm multi-mode optical fibre. The same described above set-up and acquisition system were used, with the fibre and the cables entering by a proper feed-through, used to preserve darkness conditions and thermal insulation.

Measurements at room temperature were carried out to evaluate the performance of the devices and their conformity to the requested features. Most of the measurements were repeated at cryogenic temperature to evaluate variation of any parameter which could affect the scintillation light detection. Therefore, the following PMT characteristics where tested:

- Single electron response and gain;
- Response linearity and saturation;
- Transit time and its spread;

- Photocathode uniformity;
- Dark counts.

5.1 Single electron response and gain

The output signals of the tested PMTs under a single photoelectron illumination (SER) were recorded by feeding directly the anode output to the 50 Ω input of a 1 GHz bandwidth oscilloscope. Measurements were carried out with the PMT under test operating both at room and at cryogenic temperatures, and at a multiplier gain G $\approx 10^7$. No significant variation were observed between room and cryogenic temperature, resulting in the following mean values: a leading edge of 3.9 ± 1.1 ns, a FWHM of 5.6 ± 1.1 ns and a trailing edge of 10.3 ± 1.6 ns, in good agreement with the nominal values indicated by the manufacturer.

SER measurement was made by registering the charge distribution of the PMT pulses induced by single-electron excitation at different power supply values. The typical single electron response of a PMT with labelled parts of the spectrum is shown in Figure 17.

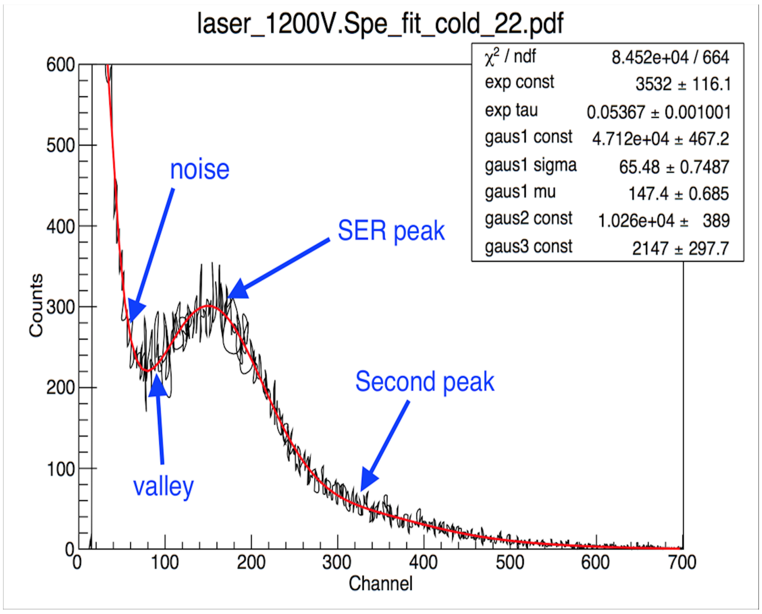

Figure 17: PMT FB0022 at 1200V, the spectrum obtained at cryogenic temperature.

This measurement represents the charge distribution of the PMT pulses integrated over the whole signal shape and by fitting a proper function it is possible to evaluate the gain of the PMT. The fitting method was elaborated in [47]. The multi-dynode system single photoelectron response can be essentially described by the Poisson distribution. However, since the amplification of a first dynode is sufficiently large the PMT response can be approximated with the

Gaussian distribution:

$$G(x) = \frac{1}{\sigma\sqrt{2\pi}} exp(\frac{-(x-\mu)^2}{2\sigma}), \quad (7)$$

where:

- x - is the measured output charge for single photoelectron;
- μ - is the average charge at the PMT output when one electron is collected by the first dynode;
- σ - is the corresponding standard deviation of the charge distribution.

The charge distribution when the process is initiated by n photoelectrons is a convolution of n one-electron cases:

$$G_n(x) = \frac{1}{\sigma\sqrt{2\pi n}} exp(\frac{-(x-n\mu)^2}{2n\sigma^2}), \quad (8)$$

All the spectra obtained from the tests were fitted by means of an analytical expression which consists of an exponential distribution related to the PMT dark counts and the electronic noise at the low signal values, and a few (3 for most of the cases) Gaussian distrubutions describing the response of the PMT to different numbers of photoelectrons. Thus the typical SER spectrum was usually fitted with the following formula:

$$F(x) = Ae^{-Bx} + \frac{C}{\sqrt{2\pi}\sigma} e^{\frac{-(x-\mu)^2}{2\sigma^2}} + \frac{D}{\sqrt{4\pi}\sigma} e^{\frac{-(x-2\mu)^2}{4\sigma^2}} + \frac{E}{\sqrt{6\pi}\sigma} e^{\frac{-(x-3\mu)^2}{6\sigma^2}}, \quad (9)$$

The position μ of the first peak allows to estimate the PMT gain G. The relation between the gain and the HV applied to the PMT was measured by changing the HV setting in a range from about G= 10^6 to about G= 5×10^7.

Test results described in this section are usually shown for the PMT with serial number FB0051, which is a typical one.

Figure 18 shows the signal amplitude (gain) distributions in a function of the applied voltage at room and cryogenic temperatures for the PMT FB0051. At both temperatures the data are well described by the function:

$$G = A * V^C + B \quad (10)$$

where $C = \alpha \times n$. The α parameter is usually ranging from 0.7 to 0.8 and n is being the number of dynodes. In this case the value of C parameter is 7.954 $\pm$ 0.023 and 7.921 $\pm$ 0.011 at room and cryogenic temeperatures, respectively.

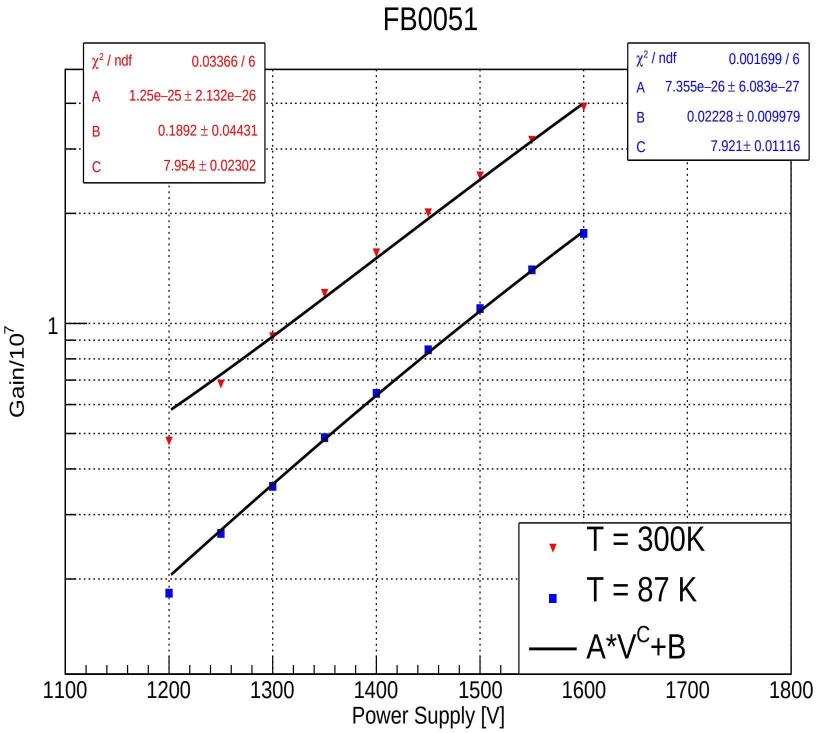

Figure 18: Signal amplitude (Gain) as a function of the anode voltage at room (300K) and at cryogenic (87K) temperatures for the PMT number FB0051. For each measurement the first peak position of the SER distribution (blue and red points) is coming from the fit (9).

These results meet the expectation of C ranging from 7 to 8 for the case of 10 dynodes stage PMT.

Figure 19 shows the relative gain variation between the room and the cryogenic temperature for the selected 60 PMTs. It is evident that a vast majority of the tested devices is characterised a gain reduction at 87 K.

With a nominal gain G $= 10^7$ at room temperature, the PMTs showed the gain losses down to about 10% at the cryogenic temperature. However, seven PMTs have the same gain at room and cryogenic temperatures. In order to recover the original gain factors an increase of the anode voltage by about 150 V was applied and appeared to be sufficient.

The resolution of the SER peak, or relative variance to the peak, defined as the ratio $\sqrt{s} = \sigma/\mu$, where the parameters are taken from the fit of SER spectrum for the first Gaussian peak of the PMT. The average values obtained for the PMTs under test for the nominal gain $G = 10^7$ are:

$$\sqrt{s_{T=300}} = 0.35 \pm 0.03,$$

$$\sqrt{s_{T=87K}} = 0.46 \pm 0.11.$$

These values are demonstrating the good PMT performance in terms of the SER resolution at both temperatures, with a slight worsening at 87 K.

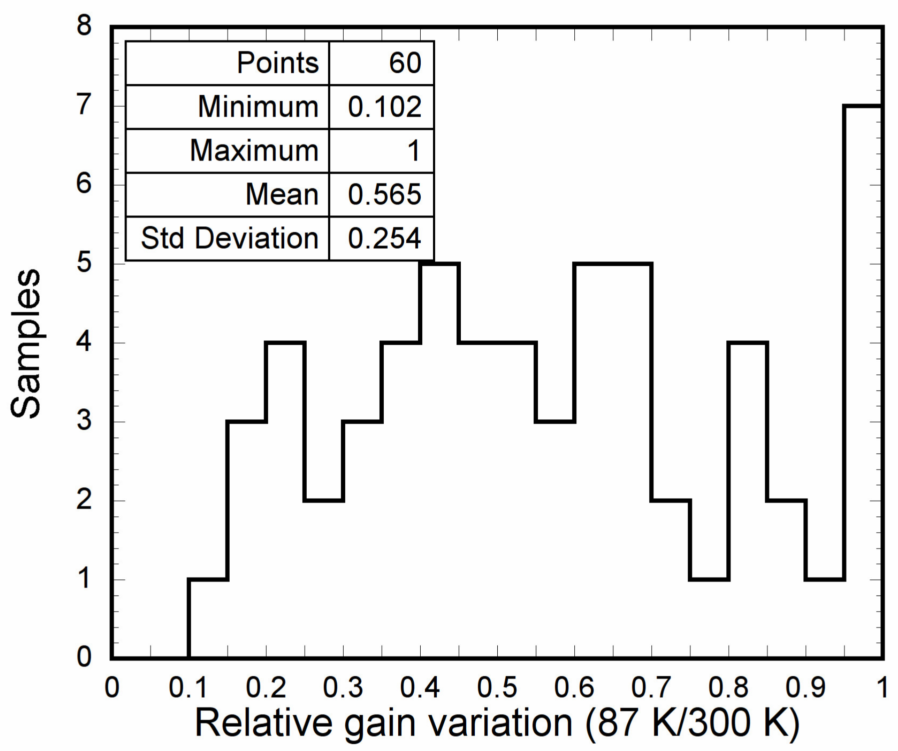

Figure 19: Relative gain variation between room and cryogenic temperature for 60 PMTs tested at both temperatures. Results are referred to a power supply settings consistent with a gain $G = 10^7$ at room temperature.

The PMT distribution of the ratio of the peak-to-valley values P/V, defined as the SER peak value divided by the minimum value to the left of the peak, obtained from fitting of the $G = 10^7$ data at the room and cryogenic temperatures, are presented in Figure 20. The most probable decrease of the P/V at crygenic temperature as compared to the room temperature was by about 50%, mainly due to an increase of the PMT dynode noise at the cryogenic temperature.

5.2 PMT response linearity and saturation

The evaluation of the PMT response linearity was carried out by the calibration system composed of a pulsed laser diode, a calibrated set of light filters with attenuation factors up to 1000 and a fibre to transmit the light to the PMT surface. The filters were mounted in a rotating support positioned between the light source and the optical fibre light guides. Taking into account the attenuation factor of the filters, it was possible to vary the light intensity on the photocathode by three orders of magnitude. The PMT gain under test was set to $G = 10^7$ both at room and at cryogenic temperatures.

As a first step the output charge distribution using the maximum attenuation filter was measured. The output charge distribution, acquired increasing the light intensity and the corresponding mean number of detected photoelectrons, was then evaluated for each filter. In Figure 21 this measured signal amplitude

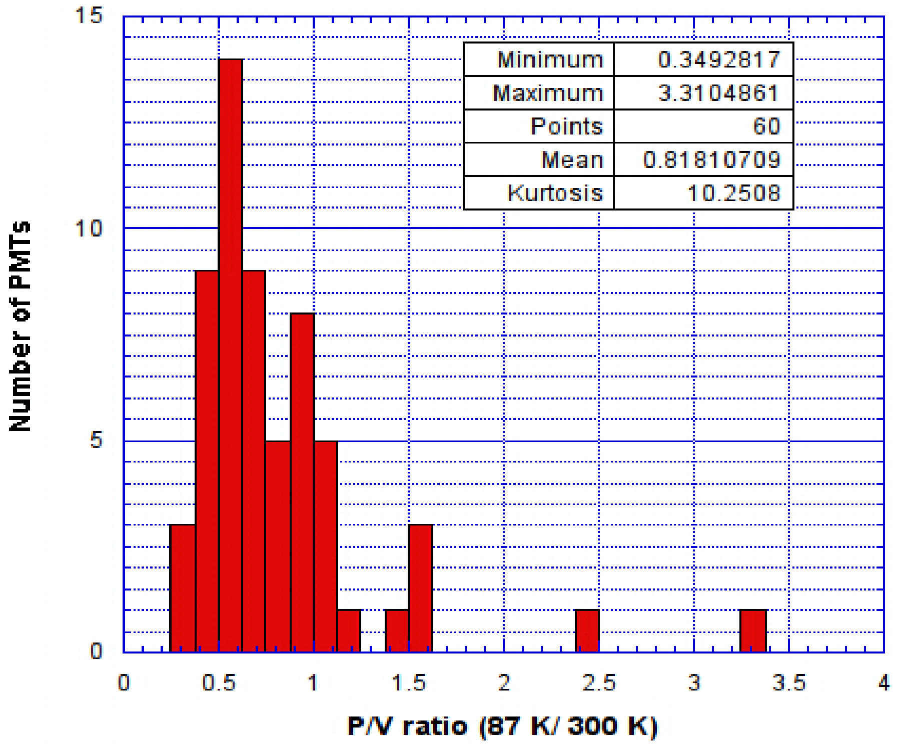

Figure 20: Distribution of the ratio of the peak-to-valley (P/V) values at the room and at the cryogenic temperatures for the 60 tested PMTs.

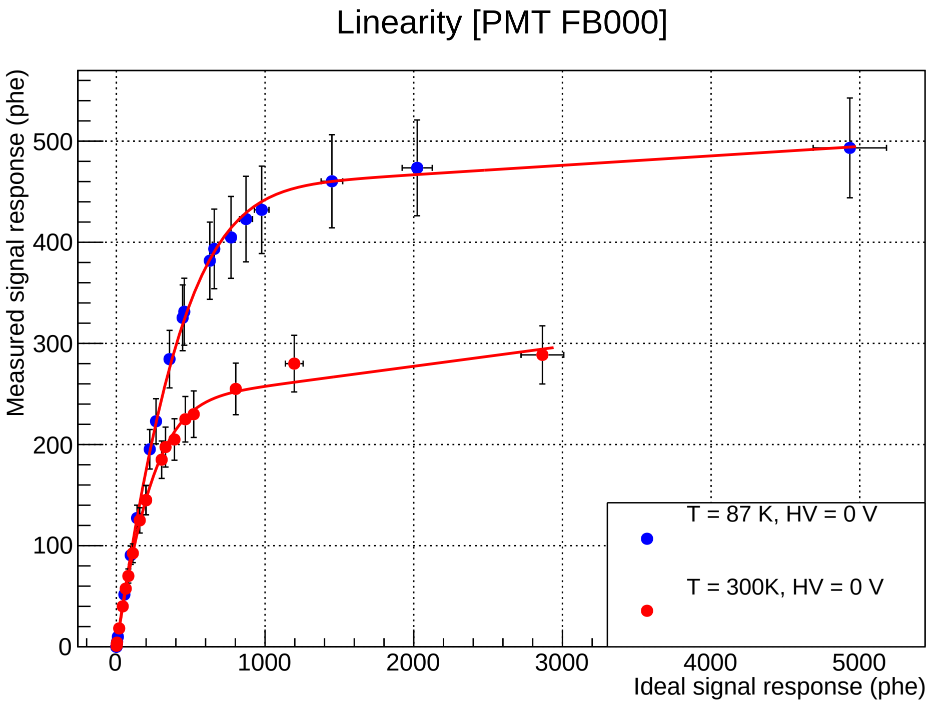

Figure 21: Measured PMT signal as a function of the ideal one at room and at cryogenic temperatures together with fitted function. The results are for the PMT number FB0051.

is plotted as a function of the number of injected photoelectrons (ideal signal amplitude), evaluated by means of the light attenuation factor, at room and at cryogenic temperatures, for the PMT number FB0051. The results demonstrate a good response linearity for up to 300 photoelectrons at cryogenic temperature and the signal saturation above this value. This fulfils the requirements of the SBNE experiment.

5.3 Transit time and its spread

The time characteristics of the PMT are governed by the electron trajectories within the tube. The transit time of a PMT is defined as a time difference between the arrival time of a photon at the photocathode and the collection of electrons at the anode. However, a spread at the transit time (TTS) is a more important parameter, because it determines the time width of the pulse of electrons arriving at the anode. The time response of a typical PMT is illustrated in Figure 22.

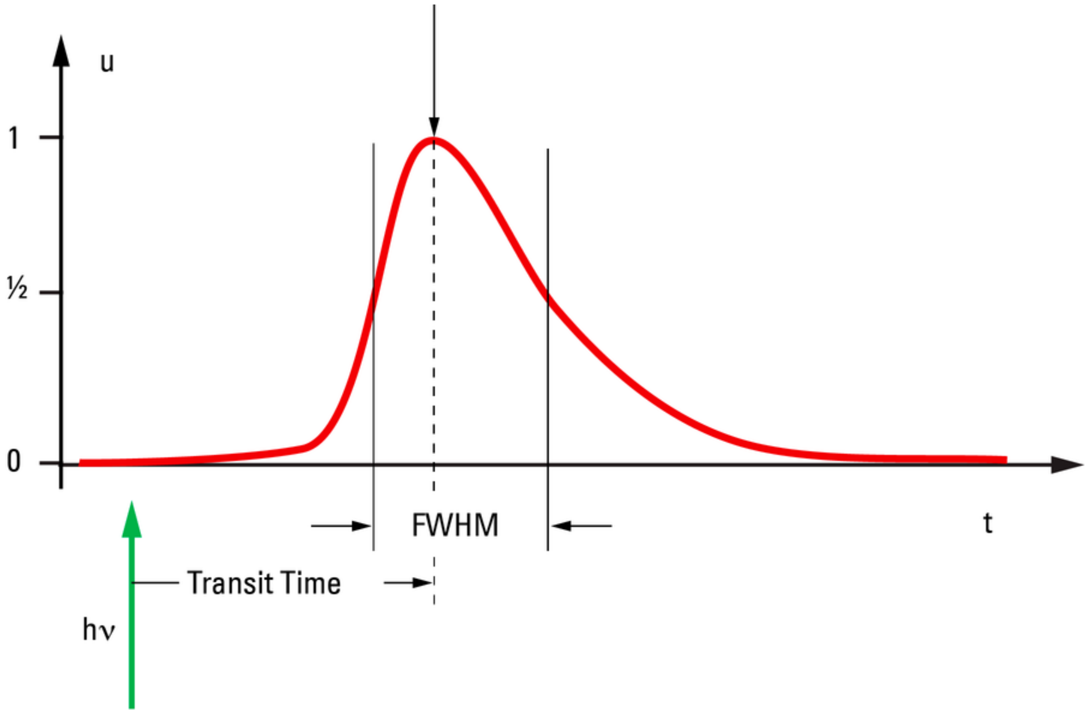

Figure 22: Photomultiplier time response.

Depending on the origin on the photocathode and emission velocities, photoelectrons produced by the light pulse follow individual paths towards the first dynode. The time dispersion present in the photomultiplier output pulse is mostly caused by the difference in paths between a photoelectron leaving the center of the photocathode and the one at its edge. Therefore, the photocathode is often curved to minimize the transit time spread across its diameter. Transit time spread results also from the distribution in initial velocities of photoelectrons leaving the photocathode. This effect can be minimized by using a large voltage difference between the photocathode and first dynode. The transit time spread depends also on the number of initial photoelectrons per pulse. For this reason usually the transit time spread is determined for a single photoelectron.

The time spread related to the multiplier section also decreases with an increasing interdynode voltage, and the best timing performance is normally obtained by operating the tube at the maximum voltage permitted by the ratings.

During the tests, the PMT transit time and its spread were measured only at room temperature. The light produced by a laser was splitted towards a fast calibrated photodiode and towards the PMT under test by means of optical fibre. The light intesity corresponded to a single photon illuminating the PMT photocathode. Both the PMT output signal and the signal on the photodiode were acquired in a common trigger mode, by a 10 GS/s oscilloscope (LeCroy WaveRunner 104MXI). The transit time of the PMT was evaluated as the difference between the reference times of these two signals, decreased by the delays due to the cables. The 50% of the leading edge signals were used as a reference. Figure 23 illustrates the measured response of a PMT to a pulse of light on the photocathode.

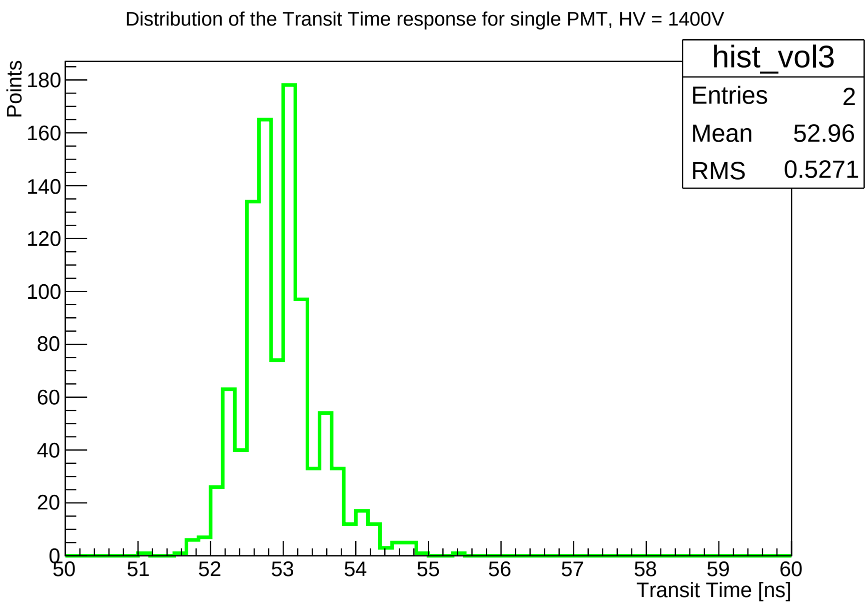

Figure 23: Distribution of the transit time response for a single PMT at room temperatures, for HV=1400V.

As a first step the optical fibre was positioned at the PMT window center. An example of the absolute PMT transit time measurement is shown in Figure 24. In the considered range of biasing voltage, a linear dependence of the transit time with a negative slope (-18 ps/V) is observed. At the nominal PMT gain $G = 10^7$, obtained at 1350 V, the measured spread of the transit time is 0.52 ns, represented in the plot by vertical error bars for the measured values of the transit time.

The same test was carried out for the illumination of different points of the

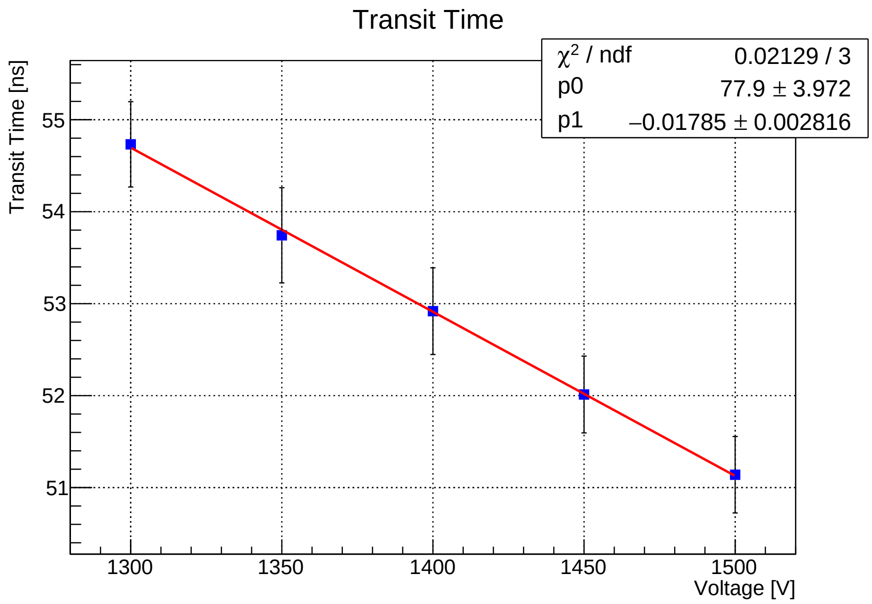

Figure 24: The relation between an absolute PMT transit time and an applied voltage together with fitted linear function. The nominal PMT gain of G= 10^7 is obtained at 1350 V. Vertical bars represent the measured transit time spread.

photocathode. The TTS variations obtained due to changing the positions of irradiation on the PMT window is showed in Figure 25. A slight increase of the absolute transit time value of up to 1 ns was observed for all the tested devices when the optical fibre was placed close to the external edge of the photocathode.

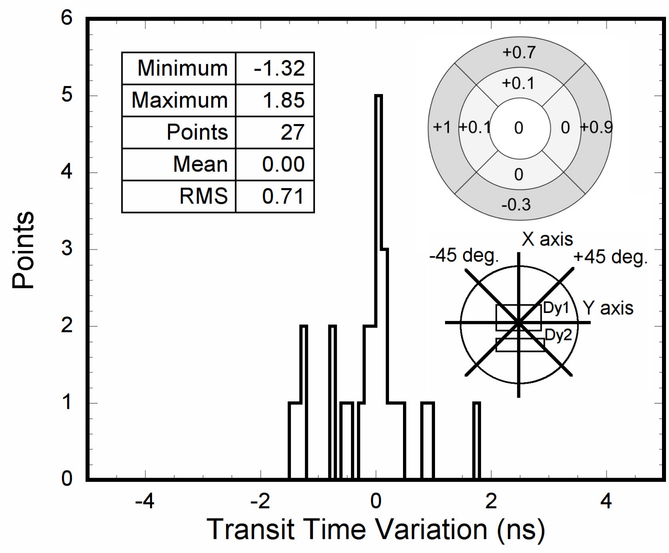

Figure 25: Variation of the TTS as a function of the incident light position on the PMT window.

5.4 Photocathode uniformity

In order to evaluate the photocathode uniformity the PMTs were operated as photodiodes. That was achieved by tying together all the dynodes and the anode as a single electrode collecting the photoelectrons emitted by the cathode kept at the negative voltage of about 300 V. The tested PMT was illuminated by means of an optical fibre: a proper support was used to maintain the fibre in a fixed orientation, normal to the PMT window, while allowing to move it in various positions on the window itself. The position was controlled by the angle along the window surface with respect to the center of curvature. As a continuos light source, a laser generating photons with a wavelength of generating $\lambda = 532$ nm was used. In order to monitor the illumination intensity and its stability, the light was splitted towards a photometer. The cathode current with the order of 10 μA, was directly measured by a picoammeter. All the PMTs show a good uniformity, within 10%, all over the measured surface. An example is shown in Figure 26.

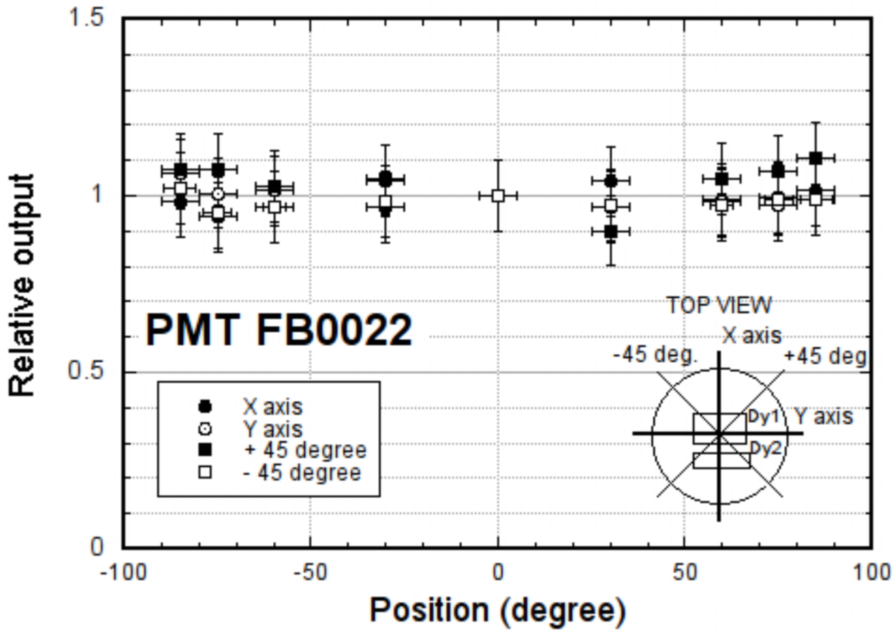

Figure 26: Response distribution for illumination of different positions on the photocathode. Values are normalized to the central position.

5.5 Dark counts

Dark counts are the response of a PMT in absence of light. The dark rate was evaluated for the PMT, operating in darkness conditions by measuring pulses to the left of the minimum value below the SER peak. The distribution obtained at room temperature for 20 tested PMTs is shown in Figure 27.

The precise evaluation of the dark count rate at cryogenic temperature was carried out for a few PMTs only, housing the device under test inside a stainless steel vacuum chamber that was set in a liquid argon bath during the cryogenic

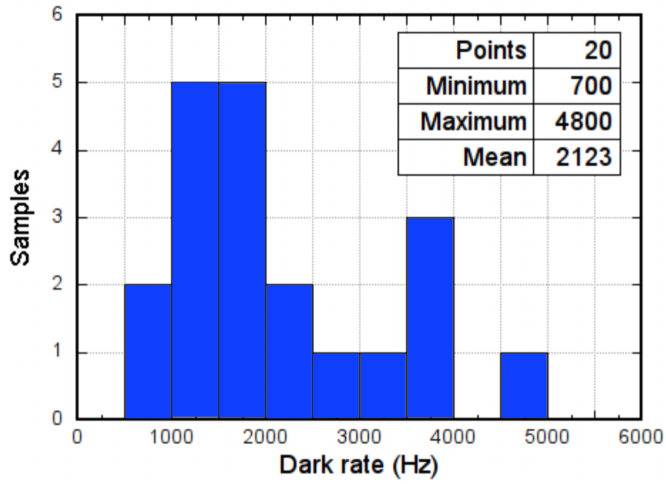

Figure 27: Dark count rate at room temperature for the 20 tested PMTs.

measurement. The increase of dark rate with decreasing temperature was observed. It is a well known effect, referred as Non-Thermal Dark Rate.

Summary and Outlook

Nowadays neutrino studies are an important part of particle physics. One of the open questions concerns the existence of sterile neutrinos. The SBNE experiment at FNAL should definitely solve the problem of the so-called LSND anomaly interpreted as evidence for sterile neutrinos.

The LArTPC detectors offer an unprecedented performance for this kind of studies, as demonstrated by the success of the already completed ICARUS experiment in the Gran Sasso laboratory. In the years 2015-2017 the ICARUS T600 detector went through an extensive renovation at CERN. Recently it was transported to FNAL to be installed as the far detector of SBNE, together with two others LArTPCs serving as the SBNE near and intermediate detectors.

The ICARUS T600 detector upgrade at CERN included the implementation of a new light collection system composed of 360 PMTs. This system is designed to identify the about 12 cosmic muons per event, constituting the most important background for the muons originating from accelerator beam neutrino interactions. This huge cosmic background is due to the fact that the detector will operate almost at the Earth surface.

During my scholarships at CERN I made significant contributions to the PMT tests, both at room and cryogenic temperatures, and to their analysis. The gamut of properties of these devices was measured in order to evaluate their performance in cryogenic conditions. For above-mentioned application of the ICARUS T600 detector the most important parameters of the PMTs are: gain, transit time and its spread, response linearity and saturation, cathode uniformity and dark count rate.

The tests demonstrated that the T600 light collection system fulfils the requirements of the SBNE experiment and the detector will manage to operate at the surface.

I have also been responsible for collecting and documenting data for all the 360 PMTs including their positions in the ICARUS coordinate system, their serial numbers and the indices of the connected cables and optical fibres. All this information is presented in the Appendix to this thesis. The next step of my work for the T600 detector will be converting the information contained in the Appendix into a professional online database for the T600 light collection system.

The work on the structure of this database has already been started with the involvement of scientists from FNAL. Next months it will be adjusted to gather any remaining data, in particular the calibration data. The T600 light collection database will be crucial for the software development of the detector.

References

[1] T. Cervi, M.E. Babicz et al., *Study of SiPM custom arrays for scintillation light detection in a Liquid Argon Time Projection Chamber,* ,JINST 12 (2017) no.03, C03007

[2] E. Fermi, *Attempt at a Theory of E-rays,* Il Nuovo Cimento, Vol.11, p.1, 1934; Zeitschrift fur Physik, Vol.88, p.161, 1934.

[3] CL. Jr. Cowan, F. Reines, et al., *Detection of the Free Neutrino: a Confirmation,* Science. (1956); 124(3212):103-4

[4] G. Giacomelli, R. Giacomelli, *The LEP Legacy,* arXiv:hep-ex/0503050

[5] ATLAS Collaboration, *Observation of a new particle in the search for the Standard Model Higgs boson with the ATLAS detector at the LHC,* Phys. Lett. B Vol. 716, (2012), Pages 1-29

[6] CMS Collaboration, *Observation of a new boson at a mass of 125 GeV with the CMS experiment at the LHC,* Phys. Lett. B Vol. 716, (2012), Pages 30-61

[7] Y. Fukuda et al, Super-Kamiokande Collaboration, *Evidence for Oscillation of Atmospheric Neutrinos* , Phys. Rev, Lett. 81 (1998) 1562-1567

[8] Q. R. Ahmad et al. (SNO Collaboration), *Measurement of the Rate of* $\nu_e + d \rightarrow p + p + e^-$ *Interactions Produced by* ^8B *Solar Neutrinos at the Sudbury Neutrino Observatory,* Phys. Rev. Lett. 87, (2001) 071301

[9] Q. R. Ahmad et al. (SNO Collaboration), *Direct Evidence for Neutrino Flavor Transformation from Neutral-Current Interactions in the Sudbury Neutrino Observatory,* Phys. Rev. Lett. 89, (2002) 011301

[10] Barger, Vernon; Marfatia, Danny; Whisnant, Kerry Lewis (2012), The Physics of Neutrinos. Princeton University Press. ISBN 0-691-12853-7.

[11] P. Armitage, *Solar Neutrinos,* JILA, University of Colorado, Boulder, 2003, Retrieved 24 April 2016

[12] B. Pontecorvo, *Mesonium and antimesonium,* Zhurnal Eksperimental'noi i Teoreticheskoi Fiziki, vol. 33, p. 549, 1957

[13] B. Pontecorvo, *Inverse beta processes and nonconservation of lepton charge,* Zhurnal Eksperimental'noi i Teoreticheskoi Fiziki, vol. 34, p. 247, 1957, Soviet Physics JETP, vol.7, (1958) p. 172-173

[14] Z. Maki, M. Nakagawa and S. Sakata, *Remarks on the Unified Model of Elementary Particles,* Progress of Theoretical Physics, Vol. 28, No. 5 (1962), p.870-880

[15] R. Davis, Jr., *A Progress Report on the Brookhaven Solar Neutrino Experiment,* BNL-14470, CONF-690814-11

John N. Bahcall, R. Davis, *Solar Neutrinos - a Scientific Puzzle,* Science 191 (1976) 264-267

[16] D. Kielczewska et al. (IMB Collaboration), *Flavor composition of atmospheric neutrinos measured in IMB-3 detector,* C93-01-30(1993), p.219-225

R. Becker-Szendy et al., *Neutrino measurements with the IMB detector,* Nucl.Phys.Proc.Suppl. 38 (1995) 331-336

[17] Kamiokande-II Collaboration (K.S. Hirata et al.), *Observation of a small atmospheric muon-neutrino / electron-neutrino ratio in Kamiokande,* Phys.Lett. B280 (1992) 146-152

[18] G. Ross, 1984, *Grand Unified Theories* , Westview Press, ISBN 978-0-8053-6968-7 Westview Press

[19] F. P. An et al., *Observation of Electron-Antineutrino Disappearance at Daya Bay,* Phys. Rev. Lett. 108 (2012) 171803

[20] Daya Bay Collaboration, *The Detector System of The Daya Bay Reactor Neutrino Experiment,* Nucl.Instrum.Meth. A811 (2016) 133-161

[21] C. Patrignani et al. (Particle Data Group), *The Review of Particle Physics,* Chin. Phys. C, 40, 100001 (2016) and 2017 update

[22] G. L. Fogli, E. Lisi, A. Marrone, D. Montanino, A. Palazzo, and A. M. Rotunno, *Global analysis of neutrino masses, mixings, and phases: Entering the era of leptonic CP violation searches,* Phys. Rev. D 86, (2012) 013012

[23] A. Aguilar et al., (LSND Collaboration), *Evidence for neutrino oscillations from the observation of $\bar{\nu}_e$ appearance in a $\bar{\nu}_\mu$ beam,* Phys. Rev. D 64, (2001) 112007

[24] A. A. Aguilar-Arevalo et al. (MiniBooNE Collaboration), *Improved Search for $\bar{\nu}_\mu \to \bar{\nu}_e$ Oscillations in the MiniBooNE Experiment,* Phys. Rev. Lett. 110, (2013) 161801

MiniBooNE Collaboration, et al., *A Combined $\nu_\mu \to \nu_e$ and $\bar{\nu}_\mu \to \bar{\nu}_e$ Oscillation Analysis of the MiniBooNE Excesses,*arXiv:1207.4809 [hep-ex]

[25] SAGE Collaboration, J. N. Abdurashitov, et al., *Measurement of the solar neutrino capture rate with gallium metal. III. Results for the 2002 - 2007 data-taking period,* Phys. Rev. C 80, (2009) 015807

[26] GALLEX Collaboration, et al., *Final results of the* ^{51}Cr *neutrino source experiments in GALLEX,* Phys. Lett., Vol. 420, (1998), 114

[27] M. A. Acero, C. Giunti, M. Laveder, *Limits on* ν_e *and* $\bar{\nu_e}$ *disappearance from Gallium and reactor experiments,* Phys. Rev. D 78, (2008) 073009

[28] G. Mention, et al., *Reactor antineutrino anomaly,* Phys. Rev. D 83, (2011) 073006

[29] M. Antonello et al. (ICARUS Coll.), *Experimental search for the LSND anomaly with the ICARUS detector in the CNGS neutrino beam,* Eur. Phys. J. C73, 2345 (2013)

[30] N. Agafonova (Moscow, INR) et al., (OPERA Collaboration), *Discovery of* τ *Neutrino Appearance in the CNGS Neutrino Beam with the OPERA Experiment,* Phys.Rev.Lett. 115 (2015) no.12, 121802

[31] The OPERA Collaboration et al., *Measurement of the neutrino velocity with the OPERA detector in the CNGS beam,* JHEP 1210 (2012) 093

[32] ICARUS Collaboration (M. Antonello (Gran Sasso) et al.), *A Search for the analogue to Cherenkov radiation by high energy neutrinos at superluminal speeds in ICARUS,* Phys.Lett. B711 (2012) 270-275

[33] M. Antonello et al., *Measurement of the neutrino velocity with the ICARUS detector at the CNGS beam,* Phys. Lett. B, Vol. 713, Issue 1, (2012), p. 17-22

[34] M. Antonello et al., *Precision measurement of the neutrino velocity with the ICARUS detector in the CNGS beam,* JHEP 1211 (2012) 049

[35] M Antonello (Gran Sasso) et al., *Experimental search for the LSND anomaly with the ICARUS detector in the CNGS neutrino beam,* Eur.Phys.J. C73 (2013) no.3, 2345

[36] M. Antonello (Gran Sasso) et al., *Precise 3D track reconstruction algorithm for the ICARUS T600 liquid argon time projection chamber detector,* Adv.High Energy Phys. 2013 (2013) 260820

[37] M. Bass, *The Short Baseline Neutrino Oscillation Program at Fermilab,* PoS ICHEP2016 (2016) 481

[38] R. Acciarri, et al., *Long-Baseline Neutrino Facility (LBNF) and Deep Underground Neutrino Experiment (DUNE) Conceptual Design Report Volume 1: The LBNF and DUNE Projects,* FERMILAB-DESIGN-2016-01

[39] R. Acciarri, et al., *Long-Baseline Neutrino Facility (LBNF) and Deep Underground Neutrino Experiment (DUNE) : Volume 2: The Physics Program for DUNE at LBNF,* FERMILAB-DESIGN-2016-02

[40] S. Amerio et al., (ICARUS Collaboration), *Design, construction and tests of the ICARUS T600 detector,* Nucl.Instrum.Meth. A527 (2004) 329-410

[41] M. Antonello et al., *Precise 3D track reconstruction algorithm for the ICARUS T600 liquid argon time projection chamber detector,* Adv.High Energy Phys. 2013 (2013) 260820

[42] ICARUS/WA104 Collaboration (Maurizio Bonesini (INFN, Milan) for the collaboration), *The WA104 Experiment at CERN,* J.Phys.Conf.Ser. 650 (2015) no.1, 012015

[43] M. Auger et al., *A Novel Cosmic Ray Tagger System for Liquid Argon TPC Neutrino Detectors,* Instruments 1 (2017) no.1, 2

[44] A. Falcone et al., *Comparison between large area photo-multiplier tubes at cryogenic temperature for neutrino and rare event physics experiments,* Nucl.Instrum.Meth. , - (2014).

[45] Milano Bicocca, Catania, LNGS, Pavia GROUPS, *Proposal for WA104 light detection system,* WA104

[46] M. Bonesini, *The WA104 Experiment at CERN,* J.Phys.Conf.Ser. 650 (2015) no.1, 012015

[47] E.H.Bellamy et al., *Absolute calibration and monitoring of a spectrometric channel using a photomultiplier,* Nucl. Instrum. Meth., in Phys. Res. A 339(1994) 468-476

List of abbreviation

$ArgoNeuT$ Argon Neutrino Teststand

BNB Booster Neutrino Beam

CC Charged-current interactions

$CNGS$ CERN Neutrinos to Gran Sasso

$CPsymmetry$ charge conjugation parity symmetry

$DUNE$ Deep Underground Neutrino Experiment

$FNAL$ Fermi National Accelerator Laboratory

$FWHM$ Full width at half maximum

$GALLEX$ Gallium Experiment

GUT Grand Unified Theory

$ICARUS$ Imaging Cosmic And Rare Underground Signals

$Lambda - CDM$ Lambda cold dark matter

LAr Liquid Argon

$LBNF$ Long Baseline Neutrino Facility

LEP Large Electron-Positron Collider

$LNGS$ Laboratori Nazionali del Gran Sasso

$LSND$ Liquid Scintillator Neutrino Detector

LXe Liquid Xenon

$MicroBooNE$ Micro Booster Neutrino Experiment

$MiniBooNE$ Mini Booster Neutrino Experiment

NC Neutral-current interactions

$NOvA$ NuMI Off-Axis ν_e Appearance

$NuMI$ Neutrinos at the Main Injector

$OPERA$ Oscillation Project with Emulsion-tRacking Apparatus

PMT Photomultiplier Tube

$SAGE$ Soviet-American Gallium Experiment

$SBND$ Short-Baseline Near Detector

$SBNE$ Short Baseline Neutrino Experiment

SER Single Electron Responce

$SiPM$ Silicon photomultiplier

SM Standard Model

SMD Surface-mounted device

SNO Sudbury Neutrino Observatory

$SURF$ Sanford Underground Research Facility

TPC Time Projection Chamber

TTS Transit Time Spread

UV Ultraviolet

VUV Vacuum Ultraviolet

Appendix

The light collection system of ICARUS T600 detector.

Layout, definitions and input into the future PMT database for the SBNE experiment.

Marta Babicz

position: **Technical Student at CERN**

CERN, September 2017

Contents

6 ICARUS T600 detector - layout of the light collection system

The ICARUS T600 detector consists of two modules and each module houses two TPCs. The detector layout is shown in Figure 28, where modules are indicated by number 1 and 2, respectively. Two TPCs in one module are indicated as the left (L) one and the right (R) one. The TPCs are divided into 9 sectors, therefore the first sector of the right TPC in the first module is marked as 1R-1. Names of all 36 sectors of the T600 detector, follow this convention.

There are 10 PMTs per sector. The scheme of their positions and numbering in each sector is presented in Figure 29.

The corresponding PMTs installed on the walls of all four TPC's, e.g. 1R-1, 1L-1, 2R-1 and 2L-1, have the same Z and X coordinates in the ICARUS coordinate system. These coordinates of all 90 PMT positions in a single TPC are shown in Figure 28 and are listed in Table 4.

As shown in Figure 30, each PMT is equipped with an optical fibre and is connected to a printed board with a signal cable and a HV cable.

The following two sections contain the PMT serial numbers and indices of the corresponding HV cable, signal cable and optical fibre associated with the positions of all 360 PMTs in a form of tables and graphical presentation, respectively.

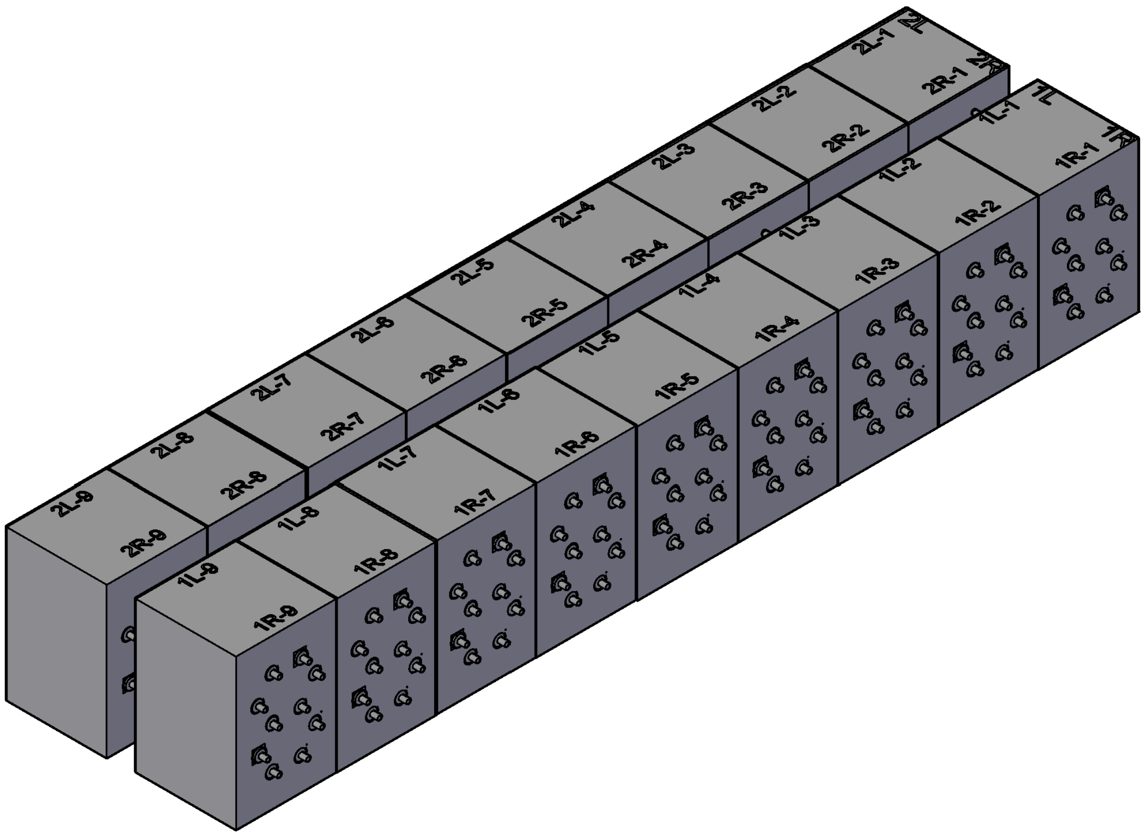

Figure 28: ICARUS T600 detector and its sectors.

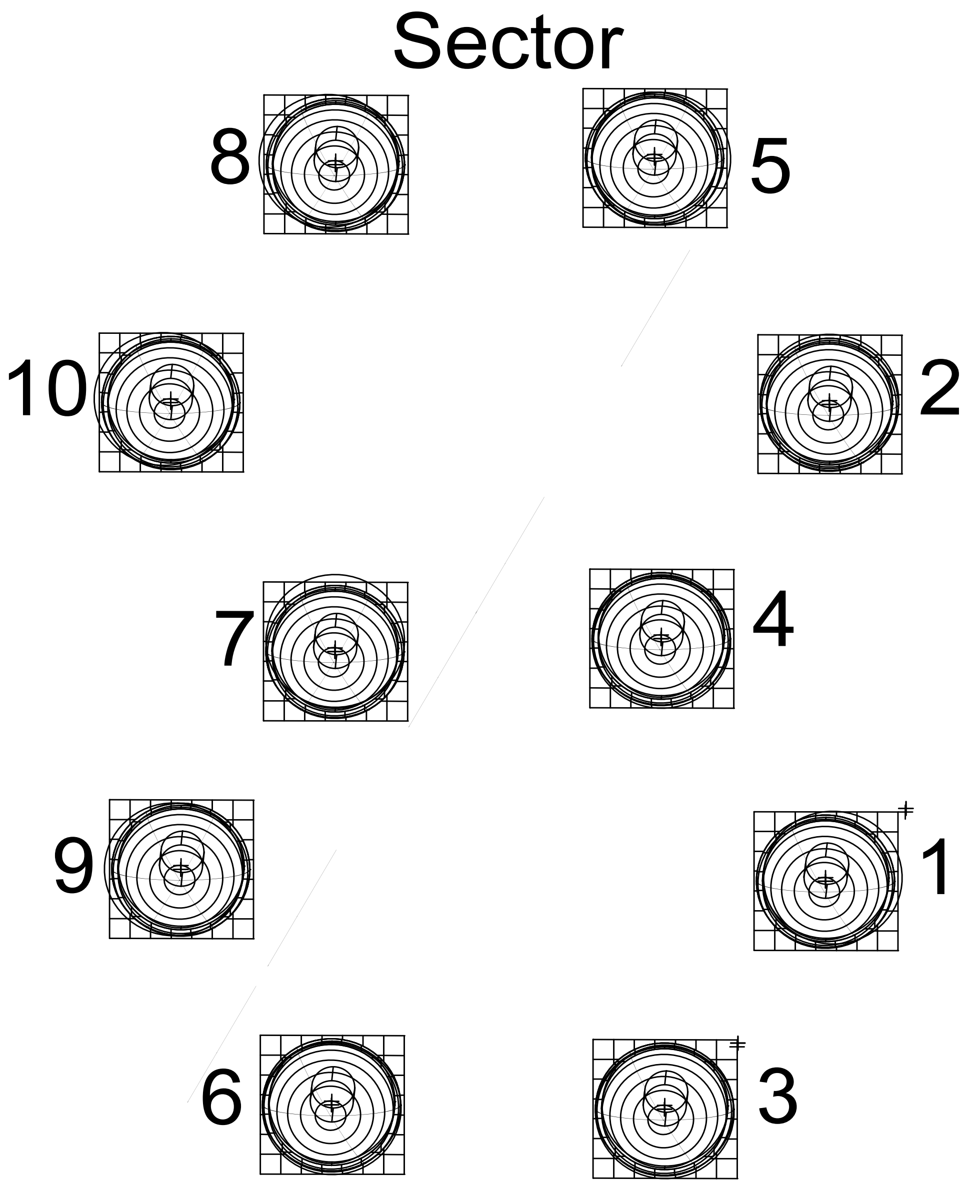

Figure 29: Positions of the PMTs in each sector.

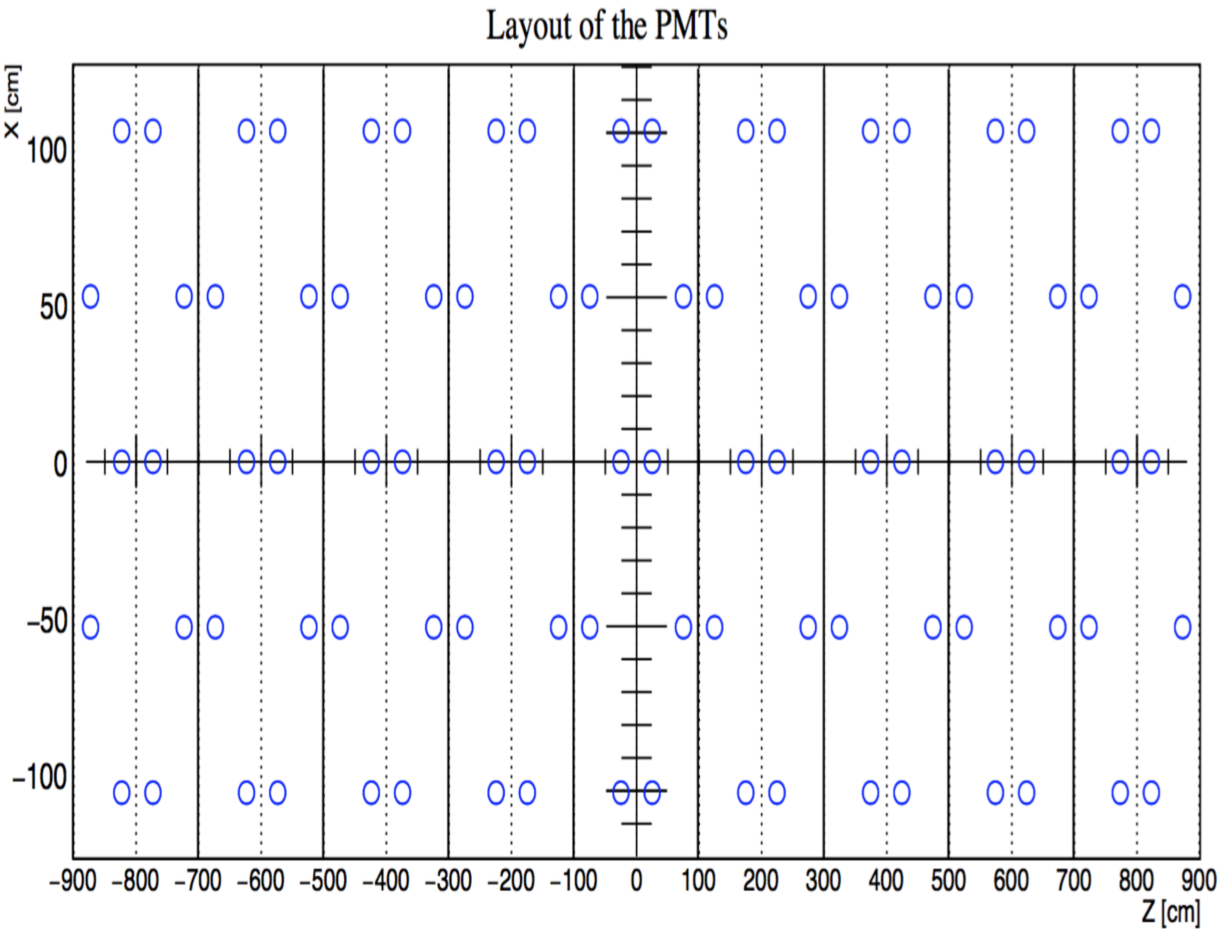

Figure 30: Positions of 90 PMTs for a single TPC in the ICARUS coordinate system.

Table 4: Z and X coordinates of 90 PMTs in a single TPC of the T600 detector, in the ICARUS coordinate system.

No.	Z coordinate of the detector [cm]	X coordinate of the detector [cm]
1	-823.02	-105.6
2	-773.14	-105.6
3	-623.5	-105.6
4	-573.62	-105.6
5	-423.98	-105.6
6	-374.1	-105.6
7	-224.46	-105.6
8	-174.58	-105.6
9	-24.94	-105.6
10	24.94	-105.6
11	174.58	-105.6
12	224.46	-105.6
13	374.1	-105.6
14	423.98	-105.6
15	573.62	-105.6
16	623.5	-105.6
17	773.14	-105.6
18	823.02	-105.6
19	-872.9	-52.8
20	-723.26	-52.8
21	-673.38	-52.8
22	-523.74	-52.8
23	-473.86	-52.8
24	-324.22	-52.8
25	-274.34	-52.8
26	-124.7	-52.8
27	-74.82	-52.8
28	74.82	-52.8
29	124.7	-52.8
30	274.34	-52.8
31	324.22	-52.8
32	473.86	-52.8
33	523.74	-52.8
34	673.38	-52.8
35	723.26	-52.8
36	872.9	-52.8
37	-823.02	0

38	-773.14	0
39	-623.5	0
40	-573.62	0
41	-423.98	0
42	-374.1	0
43	-224.46	0
44	-174.58	0
45	-24.94	0
46	24.94	0
47	174.58	0
48	224.46	0
49	374.1	0
50	423.98	0
51	573.62	0
52	623.5	0
53	773.14	0
54	823.02	0
55	-872.9	52.8
56	-723.26	52.8
57	-673.38	52.8
58	-523.74	52.8
59	-473.86	52.8
60	-324.22	52.8
61	-274.34	52.8
62	-124.7	52.8
63	-74.82	52.8
64	74.82	52.8
65	124.7	52.8
66	274.34	52.8
67	324.22	52.8
68	473.86	52.8
69	523.74	52.8
70	673.38	52.8
71	723.26	52.8
72	872.9	52.8
73	-823.02	105.6
74	-773.14	105.6
75	-623.5	105.6
76	-573.62	105.6
77	-423.98	105.6

78	-374.1	105.6
79	-224.46	105.6
80	-174.58	105.6
81	-24.94	105.6
82	24.94	105.6
83	174.58	105.6
84	224.46	105.6
85	374.1	105.6
86	423.98	105.6
87	573.62	105.6
88	623.5	105.6
89	773.14	105.6
90	823.02	105.6

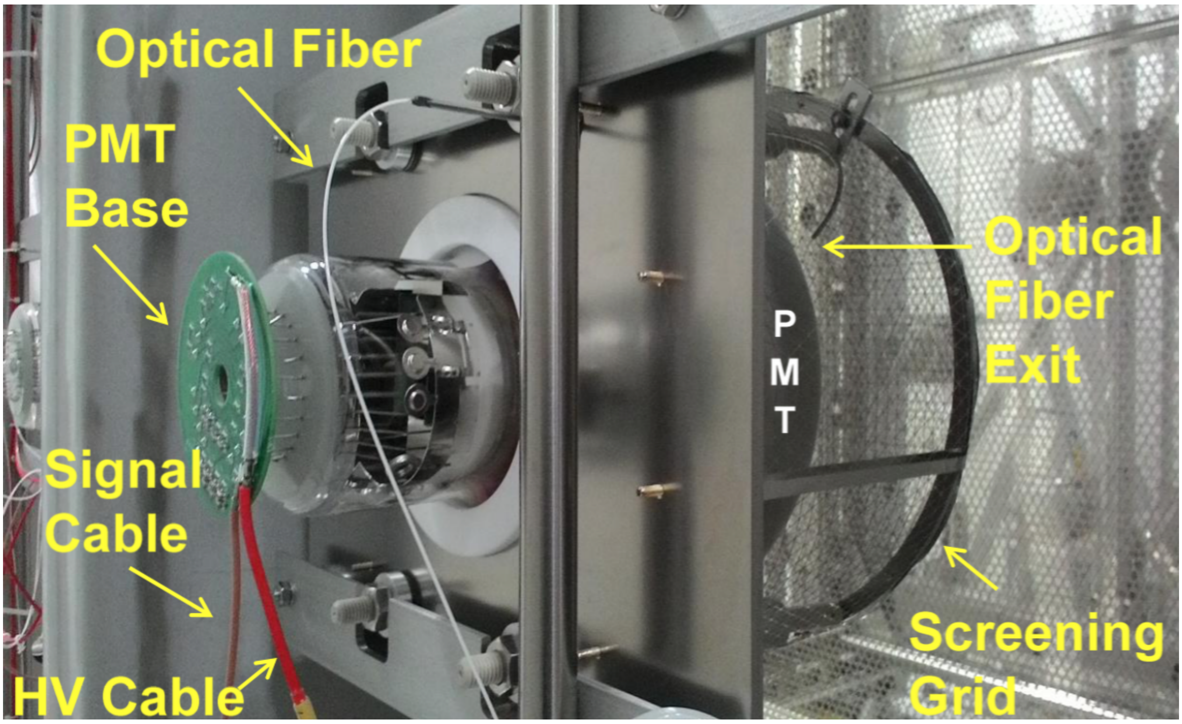

Figure 31: PMT, its printed base, optical fibre and cables.

7 Tables of the PMT positions in sectors with the PMT serial number and indices of the HV cable, signal cable and optical fibre.

7.1 First module, right side, sectors 1 - 3

SECTOR	POSITION	PMT	CABLE-HV	CABLE-SIG	FIBER
1R-1	1	**FB0039**	2	2	4
	2	**FB0130**	4	4	204
	3	**FB0054**	1	1	302
	4	**FB0022**	3	3	16
	5	**FB0038**	5	5	209
	6	**FB0101**	6	6	327
	7	**FB0119**	8	8	168
	8	**FB0040**	10	10	175
	9	**FB0086**	7	7	394
	10	**FB0142**	9	9	351
1R-2	1	**FB0234**	12	12	317
	2	**FB0060**	14	14	289
	3	**FB0242**	11	11	183
	4	**FB0043**	13	13	334
	5	**FB0103**	15	15	28
	6	**FB0208**	16	16	352
	7	**FB0091**	18	18	215
	8	**FB0116**	20	20	340
	9	**FB0235**	17	17	84
	10	**FB0092**	19	19	256
1R-3	1	**FB0168**	22	22	264
	2	**FB0136**	24	24	47
	3	**FB0240**	21	21	184
	4	**FB0057**	23	23	210
	5	**FB0146**	25	25	178
	6	**FB0162**	26	26	290
	7	**FB0117**	28	28	135
	8	**FB0131**	30	30	114
	9	**FB0176**	27	27	390
	10	**FB0076**	29	29	94

7.2 First module, right side, sectors 4 - 6

SECTOR	POSITION	PMT	CABLE-HV	CABLE-SIG	FIBER
1R-4	1	FB0197	32	32	367
	2	FB0129	34	34	329
	3	FB0205	31	31	9
	4	FB0089	33	33	332
	5	FB0133	35	35	311
	6	FB0179	37	37	399
	7	FB0090	38	38	244
	8	FB0128	40	40	67
	9	FB0189	36	36	277
	10	FB0082	39	39	197
1R-5	1	FB0102	42	42	417
	2	FB0100	44	44	180
	3	FB0077	41	41	393
	4	FB0085	43	43	235
	5	FB0145	45	45	105
	6	FB0198	46	46	188
	7	FB0097	48	48	149
	8	FB0134	50	50	252
	9	FB0081	47	47	58
	10	FB0143	49	49	62
1R-6	1	FB0026	52	52	13
	2	FB0084	54	54	153
	3	FB0112	51	51	298
	4	FB0064	53	53	185
	5	FB0051	55	55	308
	6	FB0030	56	56	412
	7	FB0066	58	58	182
	8	FB0114	60	60	422
	9	FB0069	57	57	15
	10	FB0078	59	59	408

7.3 First module, right side, sectors 7 - 9

SECTOR	POSITION	PMT	CABLE-HV	CABLE-SIG	FIBER
1R-7	1	**FB0029**	62	62	373
	2	**FB0073**	64	64	254
	3	**FB0098**	61	61	223
	4	**FB0068**	63	63	91
	5	**FB0147**	65	65	414
	6	**FB0062**	66	66	424
	7	**FB0058**	68	68	416
	8	**FB0115**	70	70	245
	9	**FB0127**	67	67	111
	10	**FB0079**	69	69	316
1R-8	1	**FB0132**	72	72	297
	2	**FB0083**	74	74	51
	3	**FB0055**	71	71	161
	4	**FB0061**	73	73	127
	5	**FB0037**	75	75	378
	6	**FB0099**	76	76	262
	7	**FB0093**	78	78	97
	8	**FB0122**	80	80	169
	9	**FB0074**	77	77	101
	10	**FB0036**	79	79	389
1R-9	1	**FB0126**	82	82	355
	2	**FB0035**	85	85	159
	3	**FB0041**	81	81	53
	4	**FB0044**	83	83	87
	5	**FB0056**	84	84	363
	6	**FB0121**	86	86	20
	7	**FB0027**	88	88	270
	8	**FB0045**	90	90	72
	9	**FB0120**	87	87	369
	10	**FB0049**	89	89	265

7.4 First module, left side, sectors 1 - 3

SECTOR	POSITION	PMT	CABLE-HV	CABLE-SIG	FIBER
1L-1	1	**FB0218**	97	97	405
	2	**FB0193**	99	99	181
	3	**FB0228**	96	96	292
	4	**FB0216**	98	98	200
	5	**FB0177**	100	100	325
	6	**FB0178**	91	91	109
	7	**FB0163**	93	93	376
	8	**FB0180**	92	92	45
	9	**FB0181**	95	95	61
	10	**FB0158**	94	94	107
1L-2	1	**FB0182**	107	107	231
	2	**FB0190**	109	109	255
	3	**FB0194**	106	106	79
	4	**FB0174**	108	108	328
	5	**FB0154**	110	110	375
	6	**FB0191**	101	101	2
	7	**FB0173**	103	103	306
	8	**FB0254**	105	105	299
	9	**FB0229**	102	102	409
	10	**FB0206**	104	104	154
1L-3	1	**FB0025**	117	117	389
	2	**FB0207**	119	119	323
	3	**FB0230**	116	116	64
	4	**FB0248**	118	118	170
	5	**FB0171**	120	120	195
	6	**FB0188**	111	111	234
	7	**FB0212**	113	113	33
	8	**FB0167**	115	115	293
	9	**FB0209**	112	112	134
	10	**FB0201**	114	114	345

7.5 First module, left side, sectors 4 - 6

SECTOR	POSITION	PMT	CABLE-HV	CABLE-SIG	FIBER
1L-4	1	**FB0231**	127	127	130
	2	**FB0239**	129	129	281
	3	**FB0261**	126	126	368
	4	**FB0232**	128	128	121
	5	**FB0157**	130	130	150
	6	**FB0170**	121	121	31
	7	**FB0214**	123	123	102
	8	**FB0150**	125	125	410
	9	**FB0237**	122	122	206
	10	**FB0251**	124	124	98
1L-5	1	**FB0196**	137	137	415
	2	**FB0256**	139	139	313
	3	**FB0144**	136	136	411
	4	**FB0249**	138	138	418
	5	**FB0153**	140	140	385
	6	**FB0160**	131	131	247
	7	**FB0199**	133	133	172
	8	**FB0165**	135	135	158
	9	**FB0104**	132	132	163
	10	**FB0187**	134	134	301
1L-6	1	**FB0183**	147	147	229
	2	**FB0210**	149	149	75
	3	**FB0024**	146	146	289
	4	**FB0258**	148	148	103
	5	**FB0175**	150	150	224
	6	**FB0138**	141	141	60
	7	**FB0220**	143	143	202
	8	**FB0169**	145	145	174
	9	**FB0135**	142	142	14
	10	**FB0238**	144	144	179

7.6 First module, left side, sectors 7 - 9

SECTOR	POSITION	PMT	CABLE-HV	CABLE-SIG	FIBER
1L-7	1	**FB0203**	157	157	187
	2	**FB0202**	159	159	271
	3	**FB0161**	156	156	162
	4	**FB0243**	158	158	74
	5	**FB0152**	160	160	370
	6	**FB0236**	151	151	44
	7	**FB0217**	153	153	52
	8	**FB0151**	155	155	196
	9	**FB0204**	152	152	296
	10	**FB0219**	154	154	241
1L-8	1	**FB0195**	167	167	66
	2	**FB0224**	169	169	259
	3	**FB0192**	166	166	288
	4	**FB0211**	168	168	139
	5	**FB0172**	170	170	333
	6	**FB0184**	161	161	324
	7	**FB0255**	163	163	425
	8	**FB0164**	165	165	142
	9	**FB0155**	162	162	302
	10	**FB0233**	164	164	307
1L-9	1	**FB0221**	176	176	356
	2	**FB0156**	179	179	21
	3	**FB0253**	177	177	143
	4	**FB0159**	178	178	152
	5	**FB0244**	180	180	119
	6	**FB0023**	171	171	123
	7	**FB0252**	173	173	314
	8	**FB0166**	175	175	283
	9	**FB0185**	172	172	349
	10	**FB0223**	174	174	320

7.7 Second module, right side, sectors 1 - 3

SECTOR	POSITION	PMT	CABLE-HV	CABLE-SIG	FIBER
2R-1	1	FB0272	182	182	157
	2	FB0260	184	184	294
	3	FB0333	181	181	211
	4	FB0429	183	183	71
	5	FB0343	185	185	116
	6	FB0391	186	186	331
	7	FB0408	188	188	7
	8	FB0263	190	190	37
	9	FB0424	187	187	240
	10	FB0321	189	189	346
2R-2	1	FB0387	192	192	361
	2	FB0323	194	194	96
	3	FB0370	191	191	274
	4	FB0426	193	193	146
	5	FB0319	195	195	55
	6	FB0299	196	196	398
	7	FB0380	198	198	284
	8	FB0141	200	200	85
	9	FB0464	197	197	27
	10	FB0439	199	199	192
2R-3	1	FB0378	202	202	332
	2	FB0450	204	204	403
	3	FB0392	201	201	263
	4	FB0384	203	203	420
	5	FB0295	205	205	125
	6	FB0397	206	206	384
	7	FB0434	208	208	160
	8	FB0302	210	210	198
	9	FB0399	207	207	189
	10	FB0328	209	209	208

7.8 Second module, right side, sectors 4 - 6

SECTOR	POSITION	PMT	CABLE-HV	CABLE-SIG	FIBER
2R-4	1	**FB0279**	212	212	57
	2	**FB0423**	214	214	337
	3	**FB0406**	211	211	207
	4	**FB0419**	213	213	366
	5	**FB0149**	215	215	99
	6	**FB0262**	216	216	156
	7	**FB0400**	218	218	88
	8	**FB0140**	220	220	303
	9	**FB0420**	217	217	381
	10	**FB0358**	219	219	305
2R-5	1	**FB0339**	222	222	343
	2	**FB0354**	224	224	131
	3	**FB0388**	221	221	267
	4	**FB0362**	223	223	113
	5	**FB0250**	225	225	338
	6	**FB0417**	226	226	216
	7	**FB0425**	228	228	237
	8	**FB0301**	230	230	10
	9	**FB0373**	227	227	344
	10	**FB0398**	229	229	372
2R-6	1	**FB0266**	232	232	199
	2	**FB0376**	234	234	342
	3	**FB0312**	231	231	70
	4	**FB0411**	233	233	38
	5	**FB0331**	235	235	76
	6	**FB0335**	236	236	319
	7	**FB0367**	238	238	214
	8	**FB0245**	240	240	419
	9	**FB0403**	237	237	41
	10	**FB0395**	239	239	77

7.9 Second module, right side, sectors 7 - 9

SECTOR	POSITION	PMT	CABLE-HV	CABLE-SIG	FIBER
2R-7	1	FB0451	242	242	222
	2	FB0455	244	244	68
	3	FB0402	241	241	404
	4	FB0357	243	243	129
	5	FB0324	245	245	26
	6	FB0330	246	246	46
	7	FB0456	248	248	401
	8	FB0317	250	250	112
	9	FB0316	247	247	5
	10	FB0281	249	249	140
2R-8	1	FB0341	252	252	304
	2	FB0274	254	254	32
	3	FB0314	251	251	65
	4	FB0405	253	253	318
	5	FB0298	255	255	90
	6	FB0275	256	256	17
	7	FB0377	258	258	167
	8	FB0259	260	260	120
	9	FB0457	257	257	282
	10	FB0368	259	259	42
2R-9	1	FB0293	262	262	212
	2	FB0401	264	264	100
	3	FB0315	375	261	253
	4	FB0433	263	263	272
	5	FB0257	265	265	413
	6	FB0148	266	266	1
	7	FB0303	268	268	92
	8	FB0320	270	270	330
	9	FB0366	267	267	201
	10	FB0271	269	269	228

7.10 Second module, left side, sectors 1 - 3

SECTOR	POSITION	PMT	CABLE-HV	CABLE-SIG	FIBER
2L-1	1	**FB0351**	277	277	374
	2	**FB0276**	279	279	230
	3	**FB0340**	276	276	350
	4	**FB0308**	278	278	166
	5	**FB0297**	280	280	35
	6	**FB0313**	271	271	177
	7	**FB0246**	273	273	83
	8	**FB0409**	275	275	212
	9	**FB0332**	272	272	93
	10	**FB0350**	274	274	106
2L-2	1	**FB0356**	287	287	80
	2	**FB0348**	289	289	406
	3	**FB0292**	286	286	321
	4	**FB0310**	288	288	387
	5	**FB0342**	290	290	380
	6	**FB0349**	281	281	357
	7	**FB0324**	283	283	255
	8	**FB0430**	285	285	43
	9	**FB0326**	282	282	173
	10	**FB0291**	284	284	249
2L-3	1	**FB0329**	297	297	35
	2	**FB0273**	299	299	78
	3	**FB0346**	296	296	391
	4	**FB0318**	298	298	176
	5	**FB0225**	300	300	310
	6	**FB0286**	291	291	233
	7	**FB0309**	293	293	246
	8	**FB0265**	295	295	11
	9	**FB0436**	292	292	25
	10	**FB0282**	294	294	95

7.11 Second module, left side, sectors 4 - 6

SECTOR	POSITION	PMT	CABLE-HV	CABLE-SIG	FIBER
2L-4	1	**FB0369**	307	307	136
	2	**FB0353**	309	309	194
	3	**FB0294**	306	306	269
	4	**FB0432**	308	308	243
	5	**FB0139**	310	310	186
	6	**FB0277**	301	301	219
	7	**FB0383**	303	303	423
	8	**FB0296**	305	305	148
	9	**FB0393**	302	302	6
	10	**FB0352**	304	304	421
2L-5	1	**FB0414**	317	317	379
	2	**FB0382**	319	319	39
	3	**FB0287**	316	316	24
	4	**FB0447**	318	318	82
	5	**FB0361**	375	320	360
	6	**FB0386**	311	311	122
	7	**FB0428**	376	313	326
	8	**FB0347**	315	315	147
	9	**FB0448**	312	312	227
	10	**FB0381**	314	314	226
2L-6	1	**FB0449**	327	327	205
	2	**FB0283**	329	329	9
	3	**FB0363**	326	326	388
	4	**FB0454**	328	328	126
	5	**FB0445**	330	330	151
	6	**FB0444**	321	321	236
	7	**FB0416**	323	323	278
	8	**FB0427**	325	325	48
	9	**FB0267**	322	322	30
	10	**FB0289**	324	324	258

7.12 Second module, left side, sectors 7 - 9

SECTOR	POSITION	PMT	CABLE-HV	CABLE-SIG	FIBER
2L-7	1	**FB0375**	337	337	108
	2	**FB0279**	339	339	164
	3	**FB0305**	336	336	19
	4	**FB0360**	338	338	141
	5	**FB0290**	340	340	23
	6	**FB0325**	331	331	12
	7	**FB0394**	333	333	390
	8	**FB0407**	335	335	395
	9	**FB0372**	332	332	268
	10	**FB0288**	334	334	138
2L-8	1	**FB0412**	347	347	137
	2	**FB0289**	349	349	257
	3	**FB0311**	346	346	43
	4	**FB0306**	348	348	128
	5	**FB0359**	250	250	190
	6	**FB0285**	341	341	220
	7	**FB0413**	343	343	309
	8	**FB0300**	345	345	354
	9	**FB0345**	342	342	69
	10	**FB0280**	344	344	266
2L-9	1	**FB0410**	357	357	239
	2	**FB0415**	359	359	50
	3	**FB0421**	356	356	132
	4	**FB0435**	358	358	22
	5	**FB0269**	360	360	144
	6	**FB0270**	351	351	191
	7	**FB0466**	353	353	364
	8	**FB0404**	355	355	295
	9	**FB0268**	352	352	110
	10	**FB0334**	354	354	341

8 Graphical representation of positions in sectors with identifiers of the corresponding PMT, HV cable, signal cable and optical fiber.

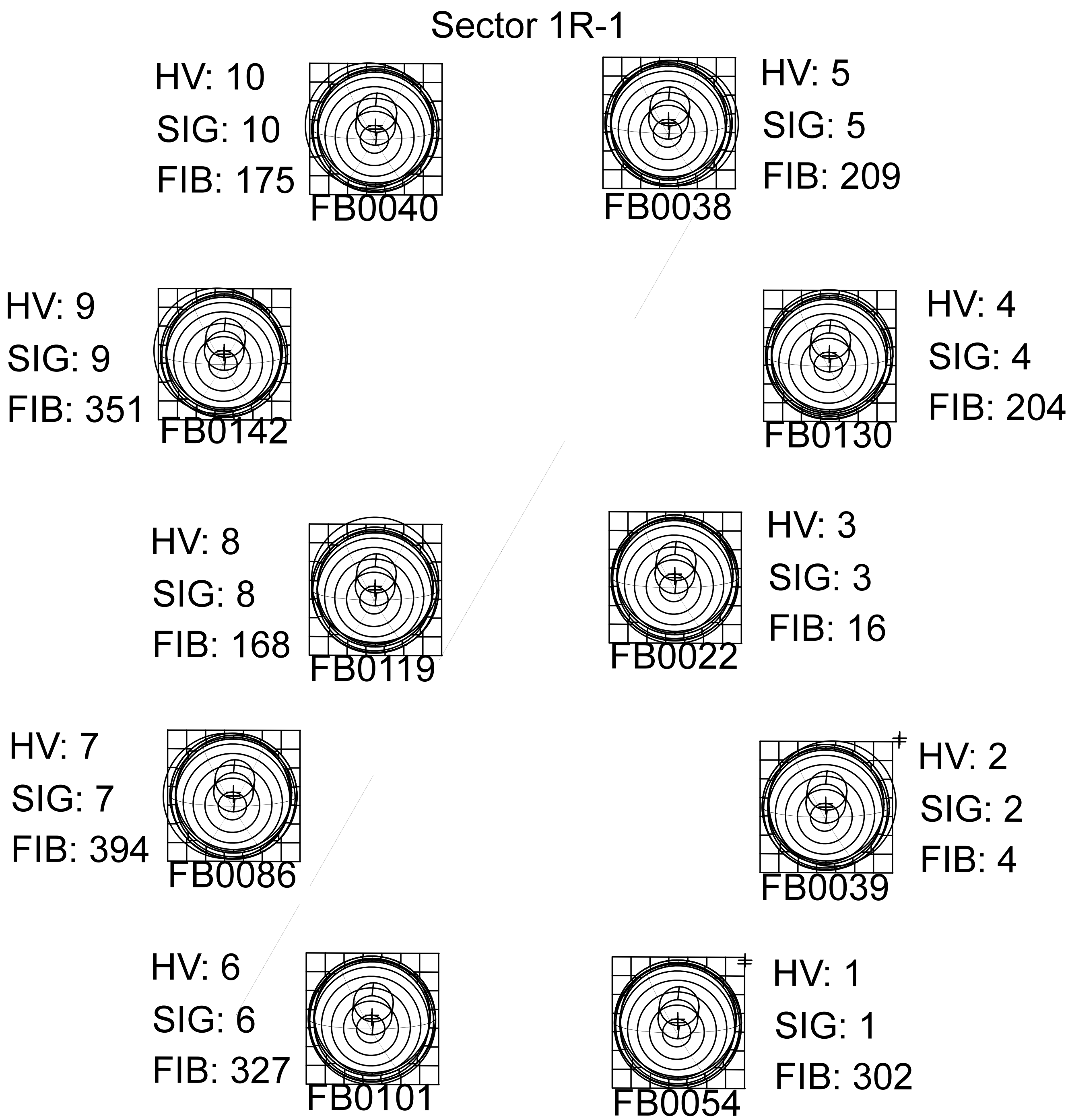

Figure 32: Sector 1R-1. The PMT deployment is seen from the TPC outside.

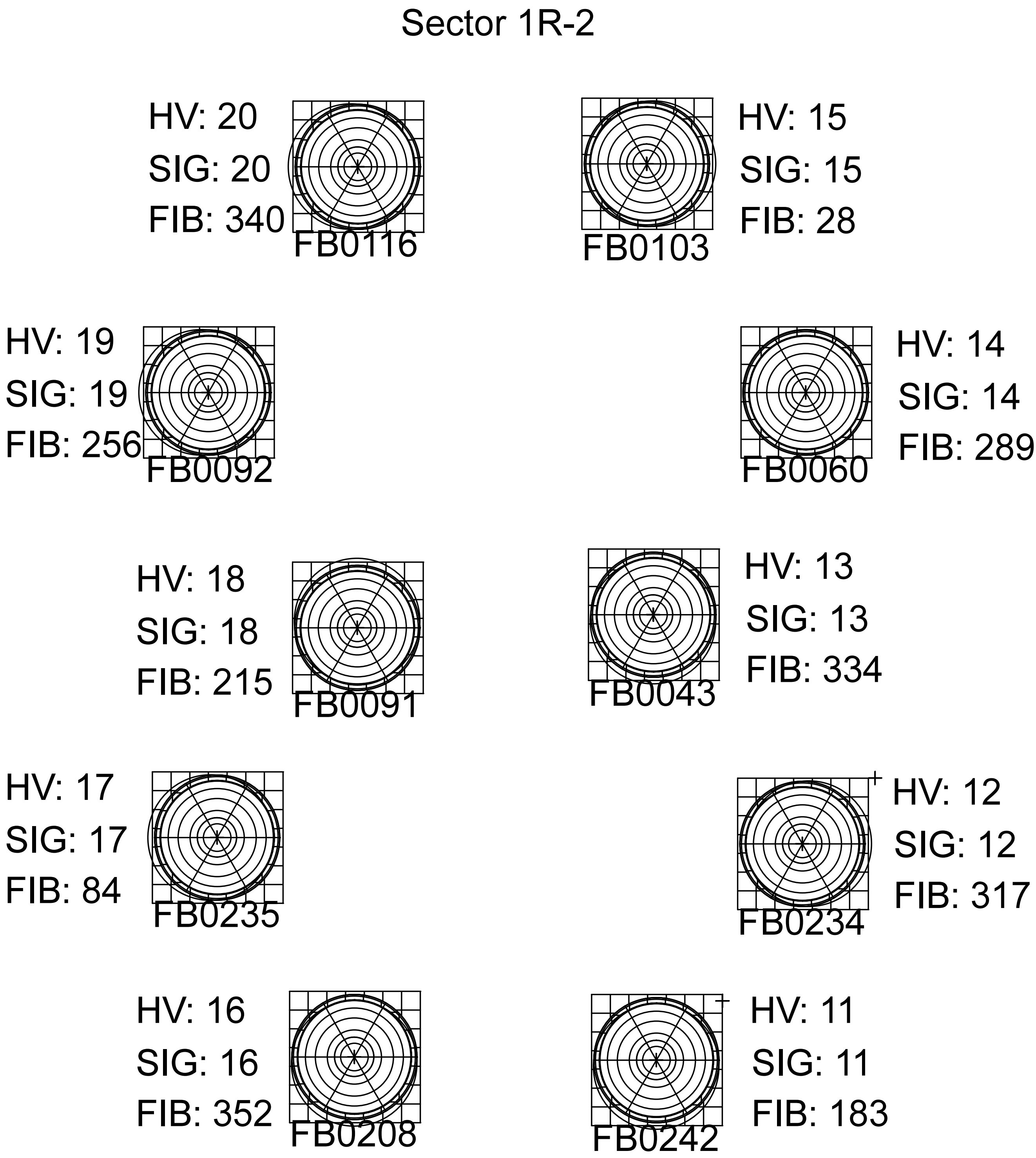

Figure 33: Sector 1R-2. The PMT deployment is seen from the TPC outside.

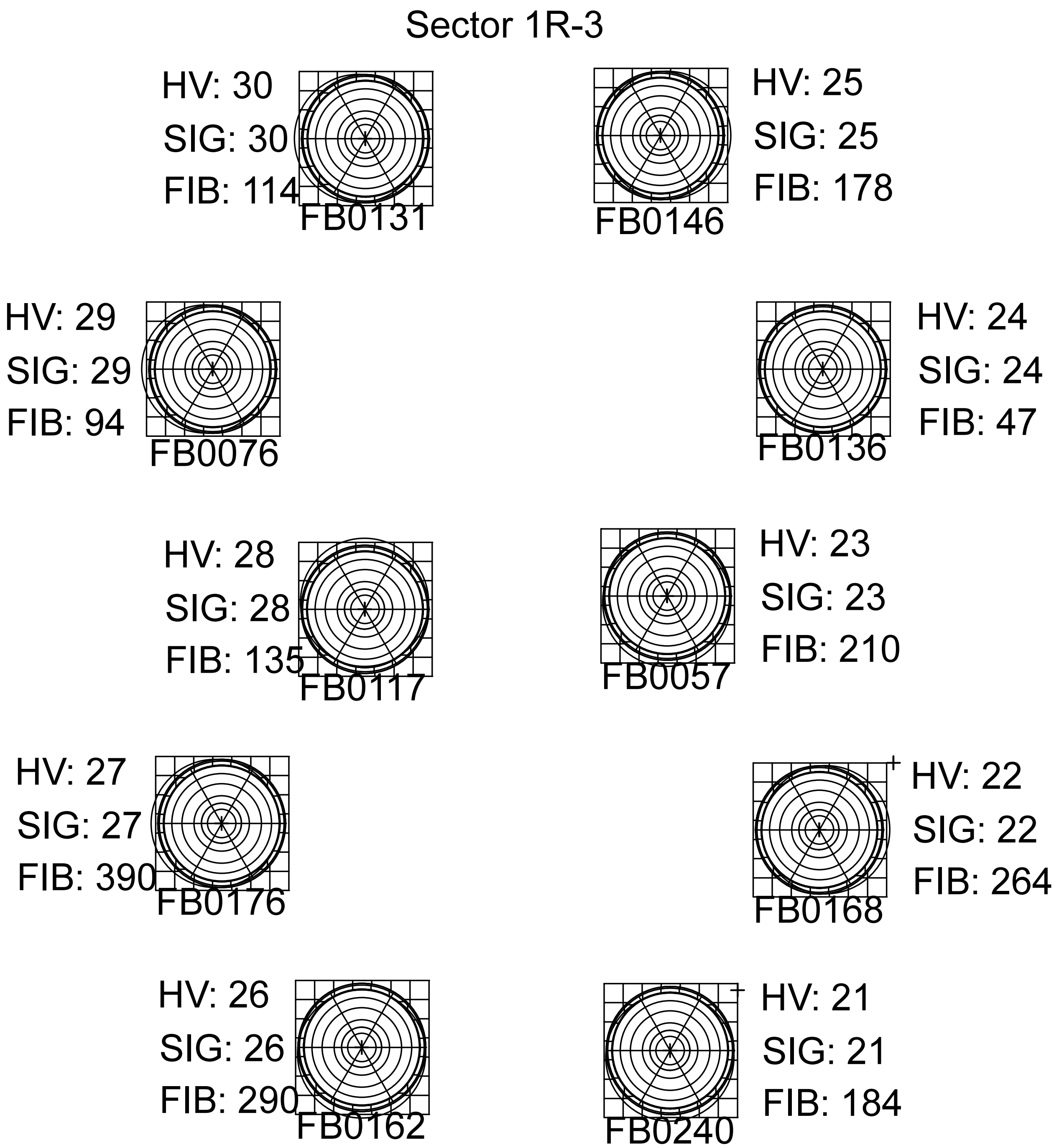

Figure 34: Sector 1R-3. The PMT deployment is seen from the TPC outside.

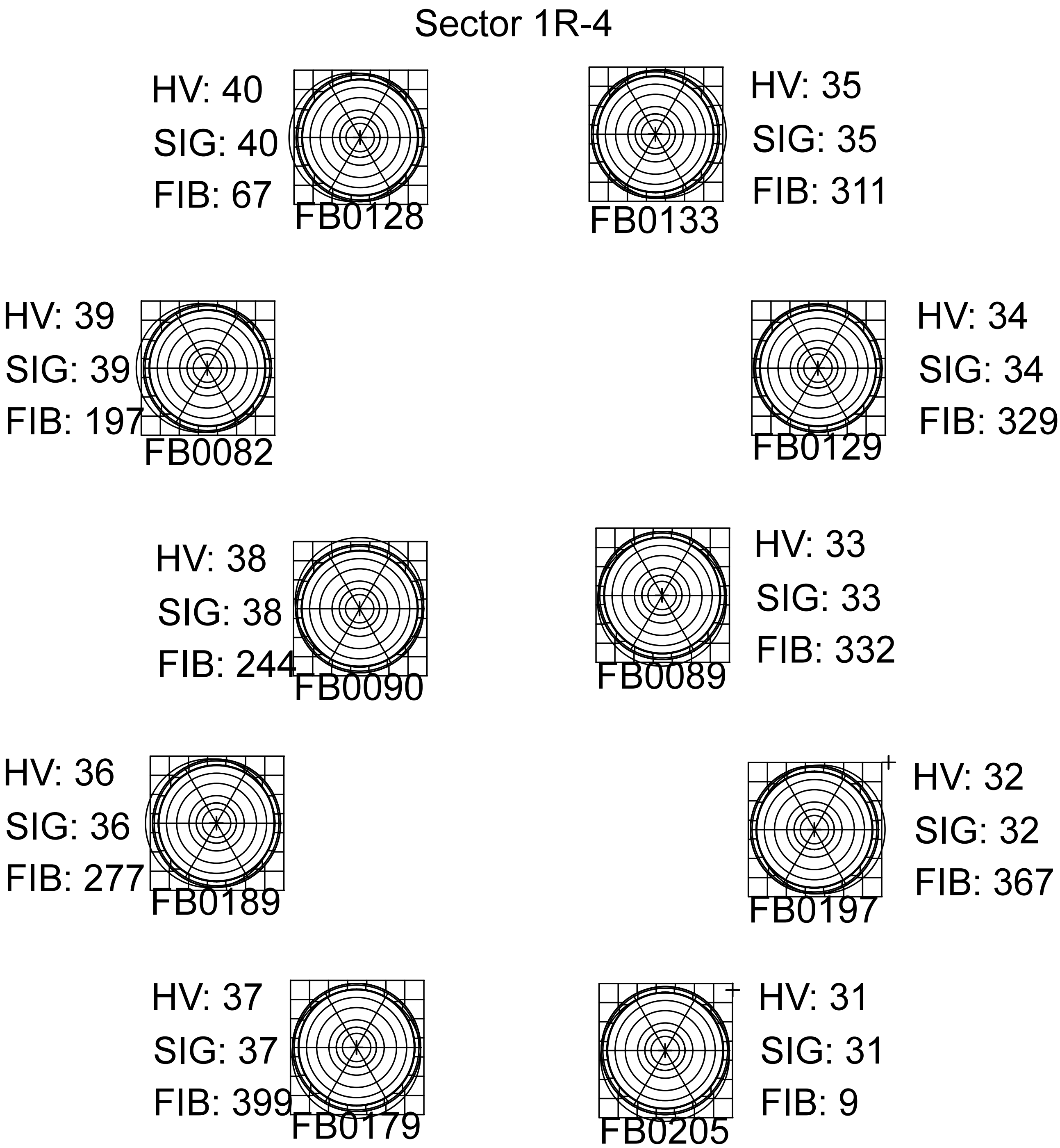

Figure 35: Sector 1R-4. The PMT deployment is seen from the TPC outside.

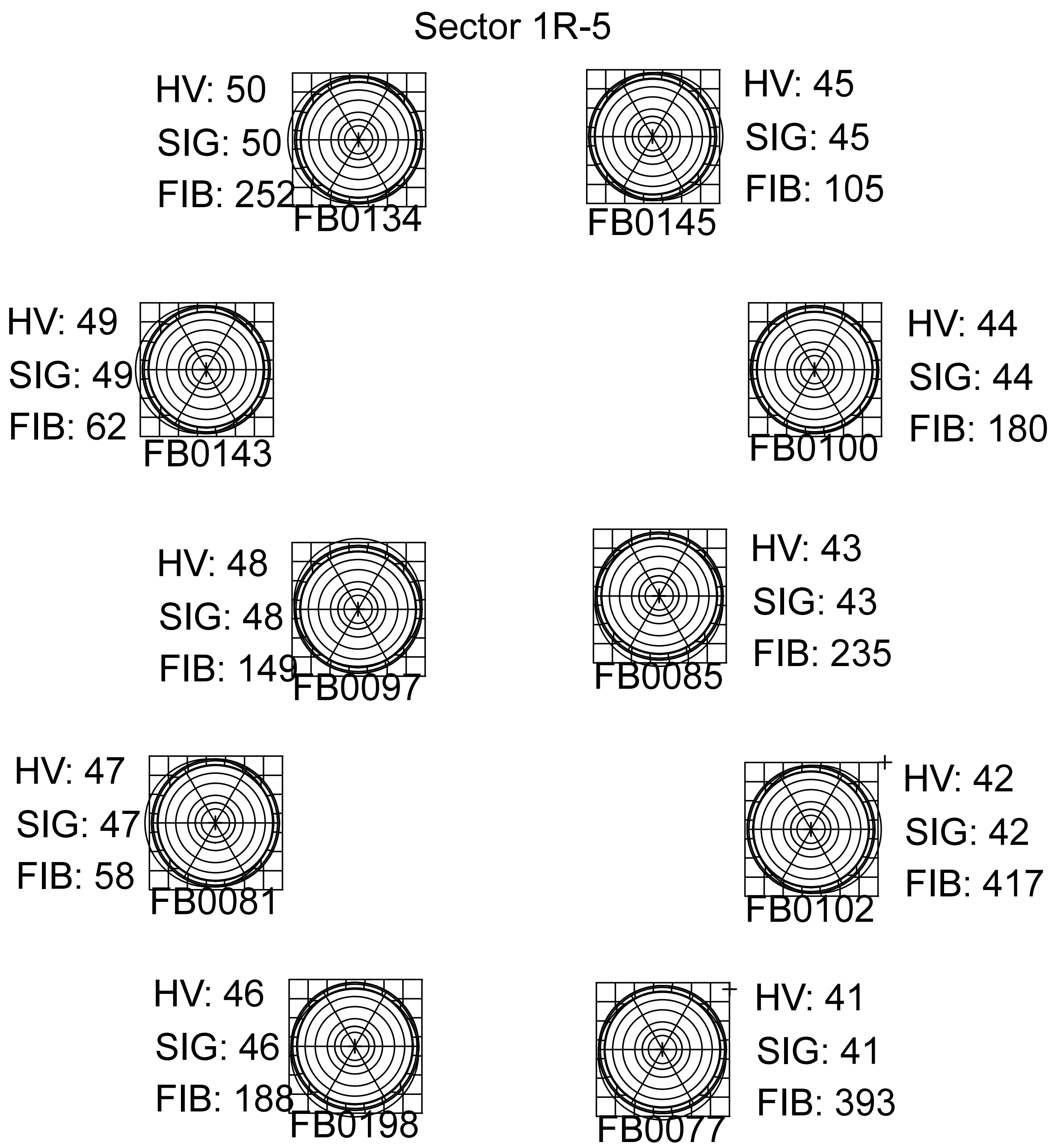

Figure 36: Sector 1R-5. The PMT deployment is seen from the TPC outside.

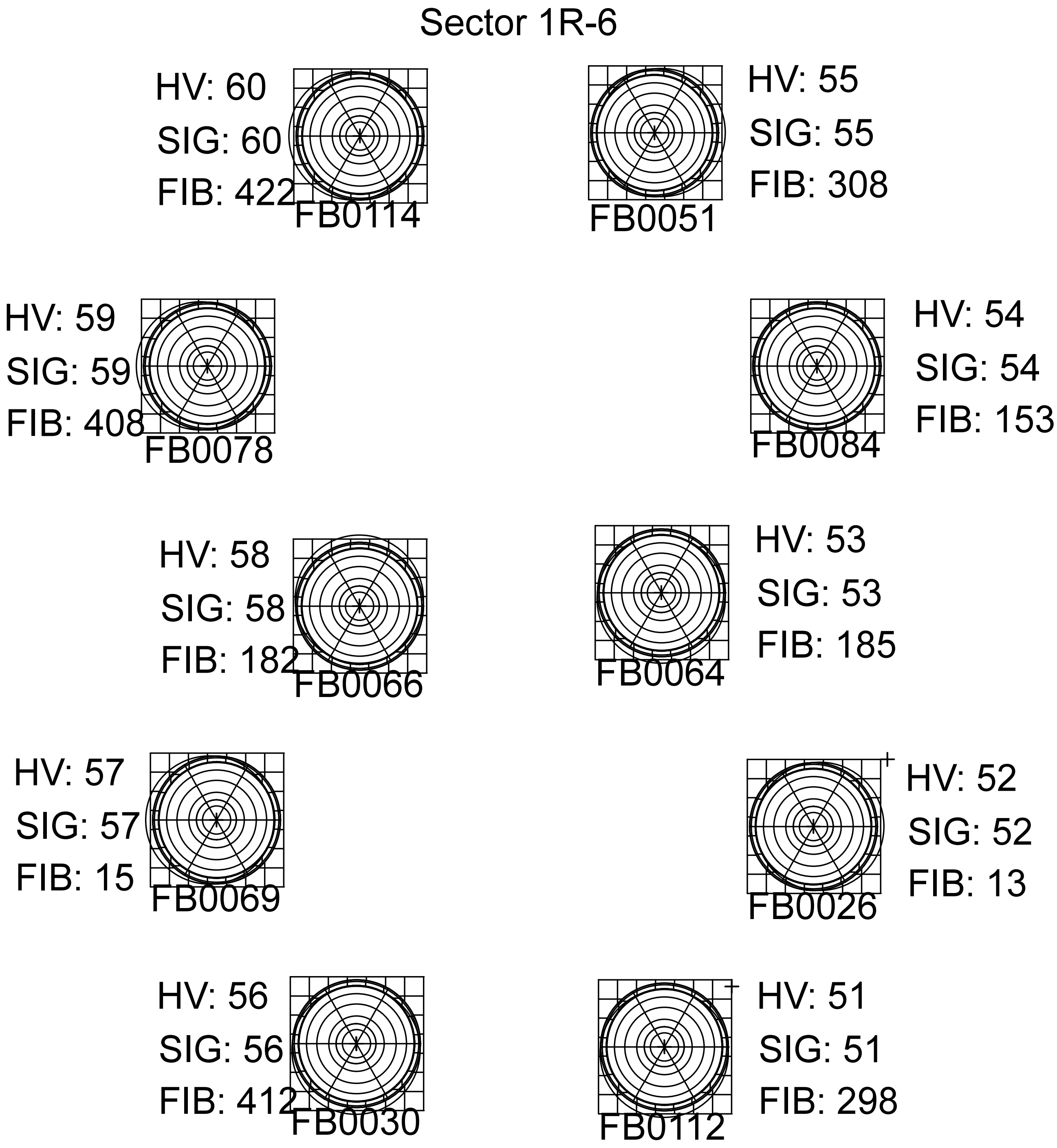

Figure 37: Sector 1R-6. The PMT deployment is seen from the TPC outside.

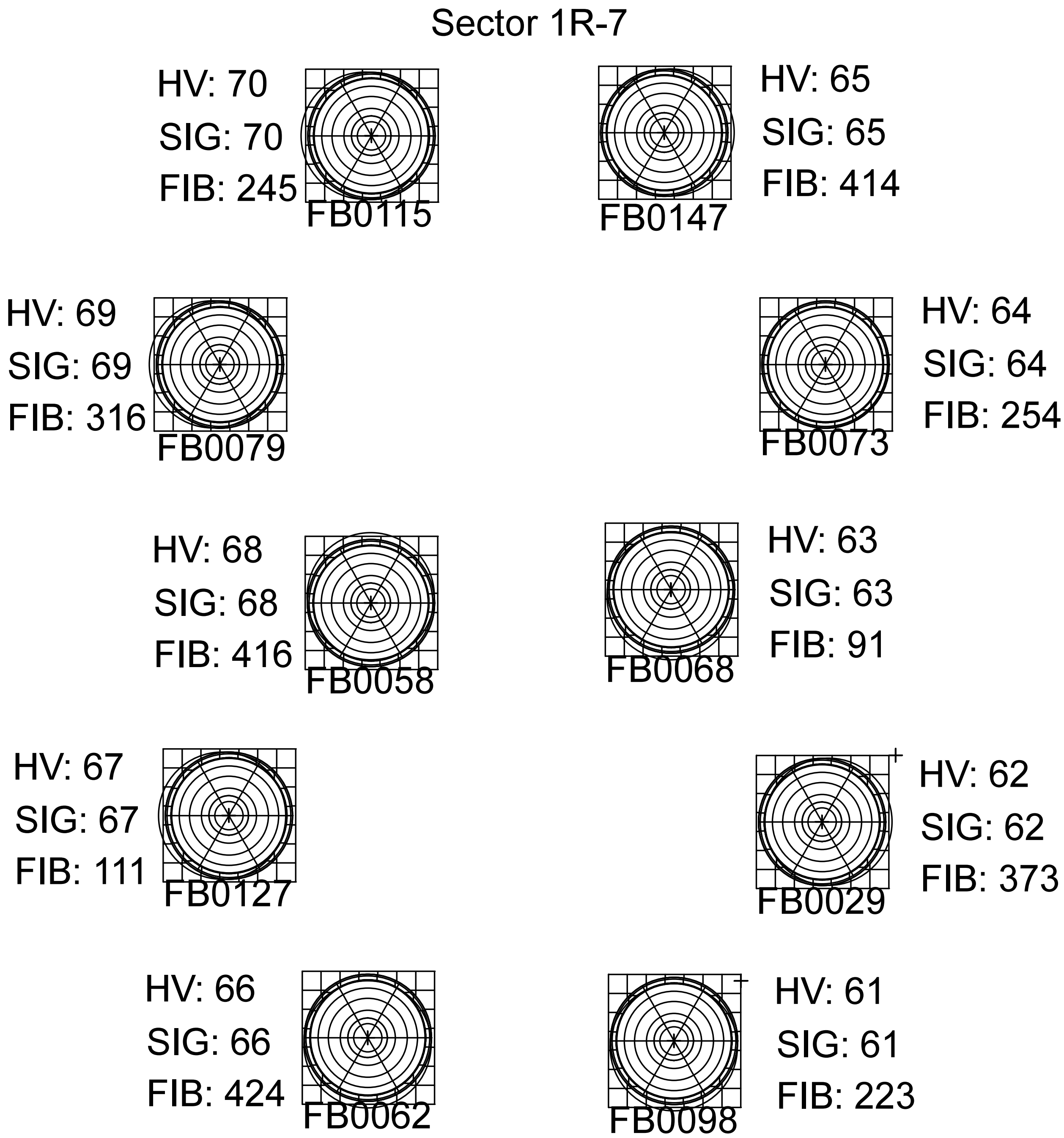

Figure 38: Sector 1R-7. The PMT deployment is seen from the TPC outside.

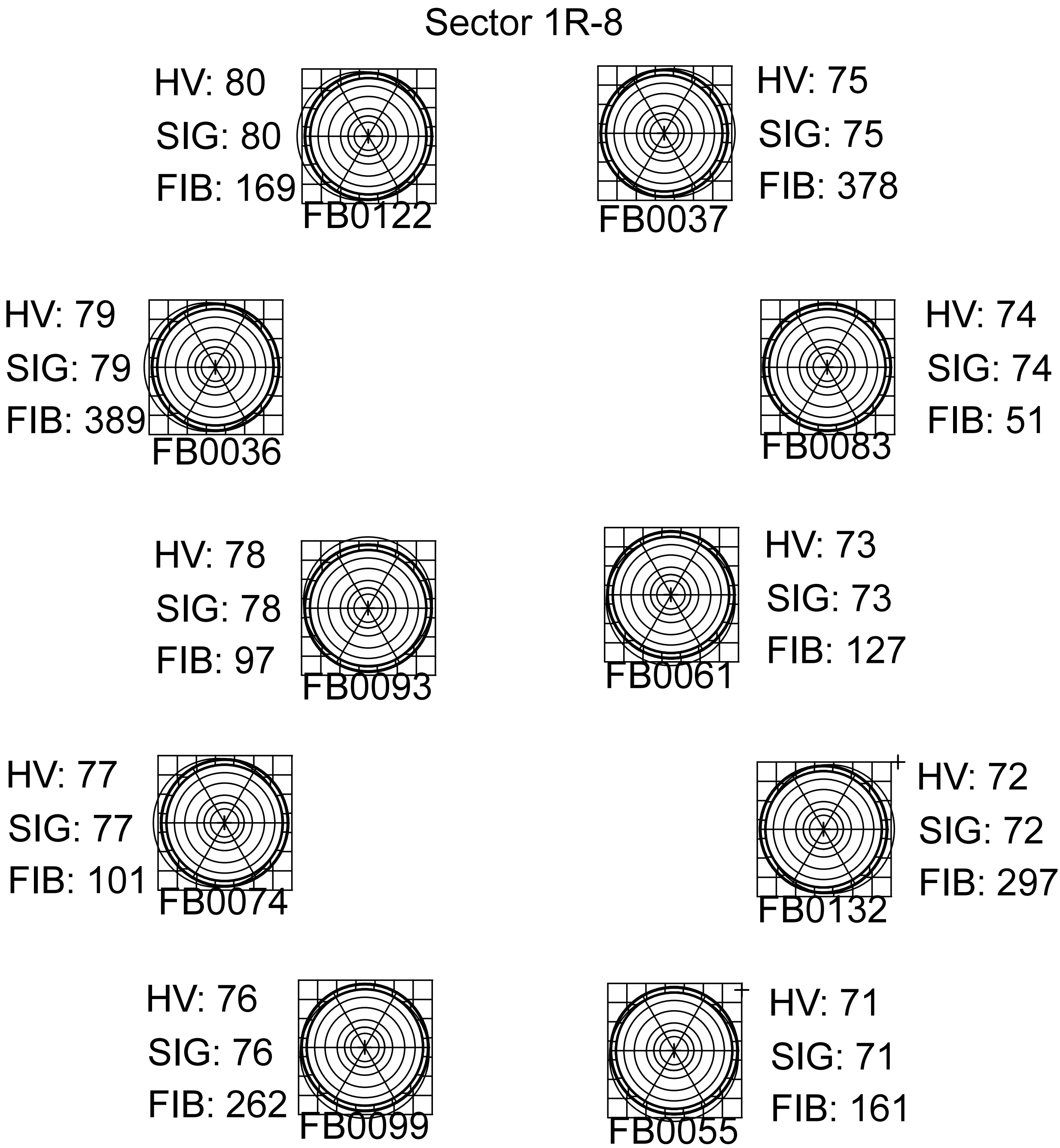

Figure 39: Sector 1R-8. The PMT deployment is seen from the TPC outside.

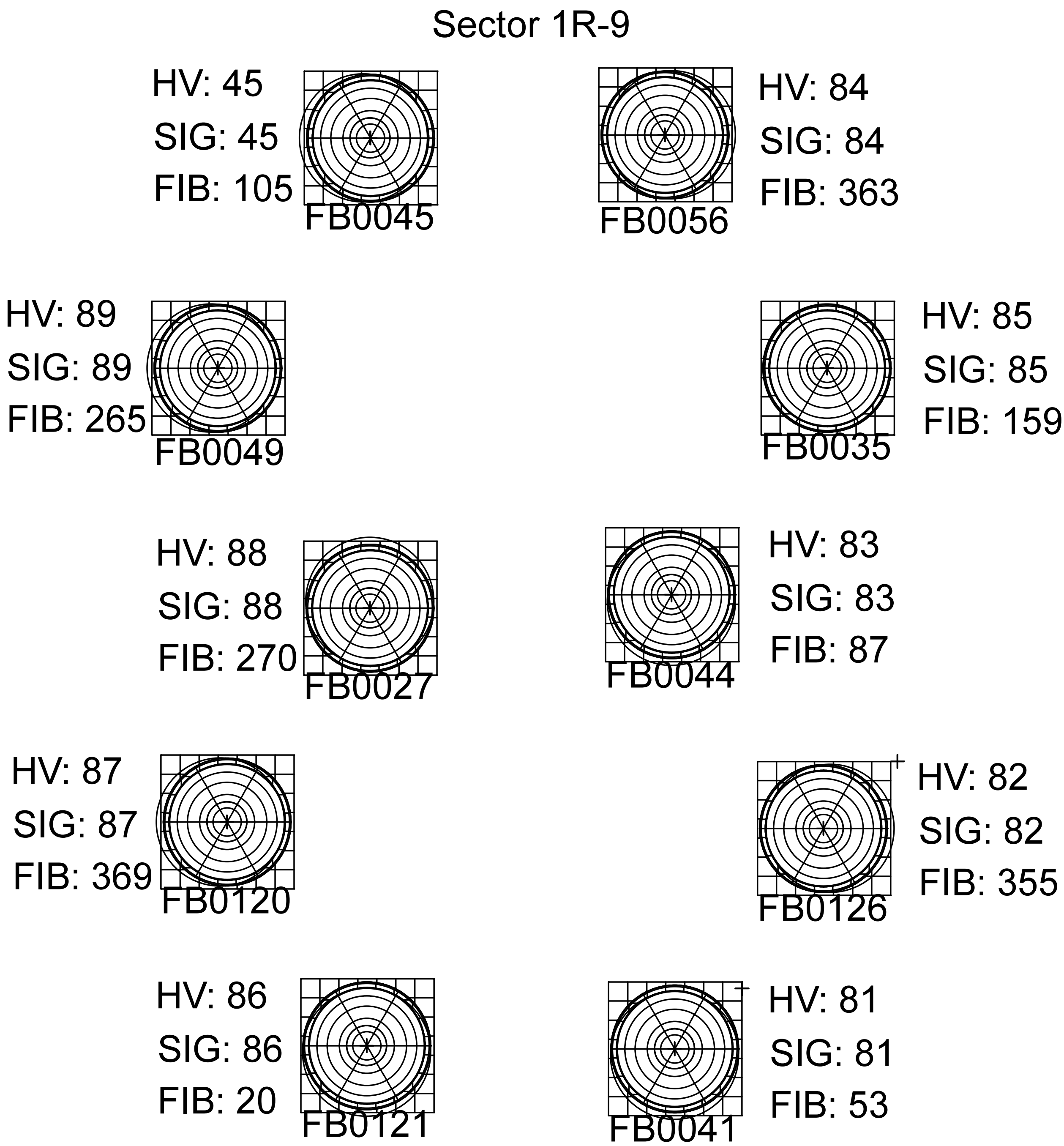

Figure 40: Sector 1R-9. The PMT deployment is seen from the TPC outside.

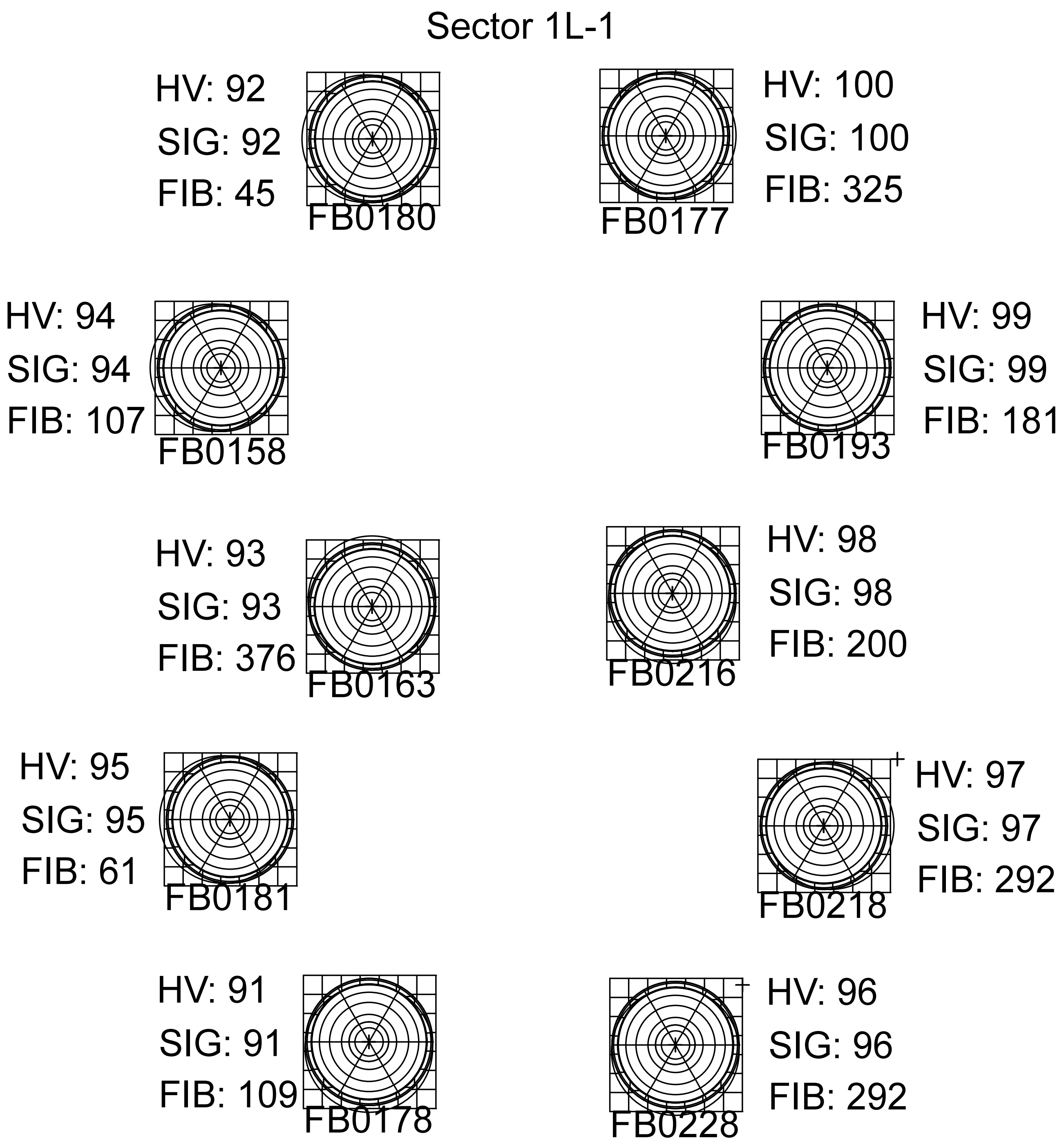

Figure 41: Sector 1L-1. The PMT deployment is seen from the TPC outside.

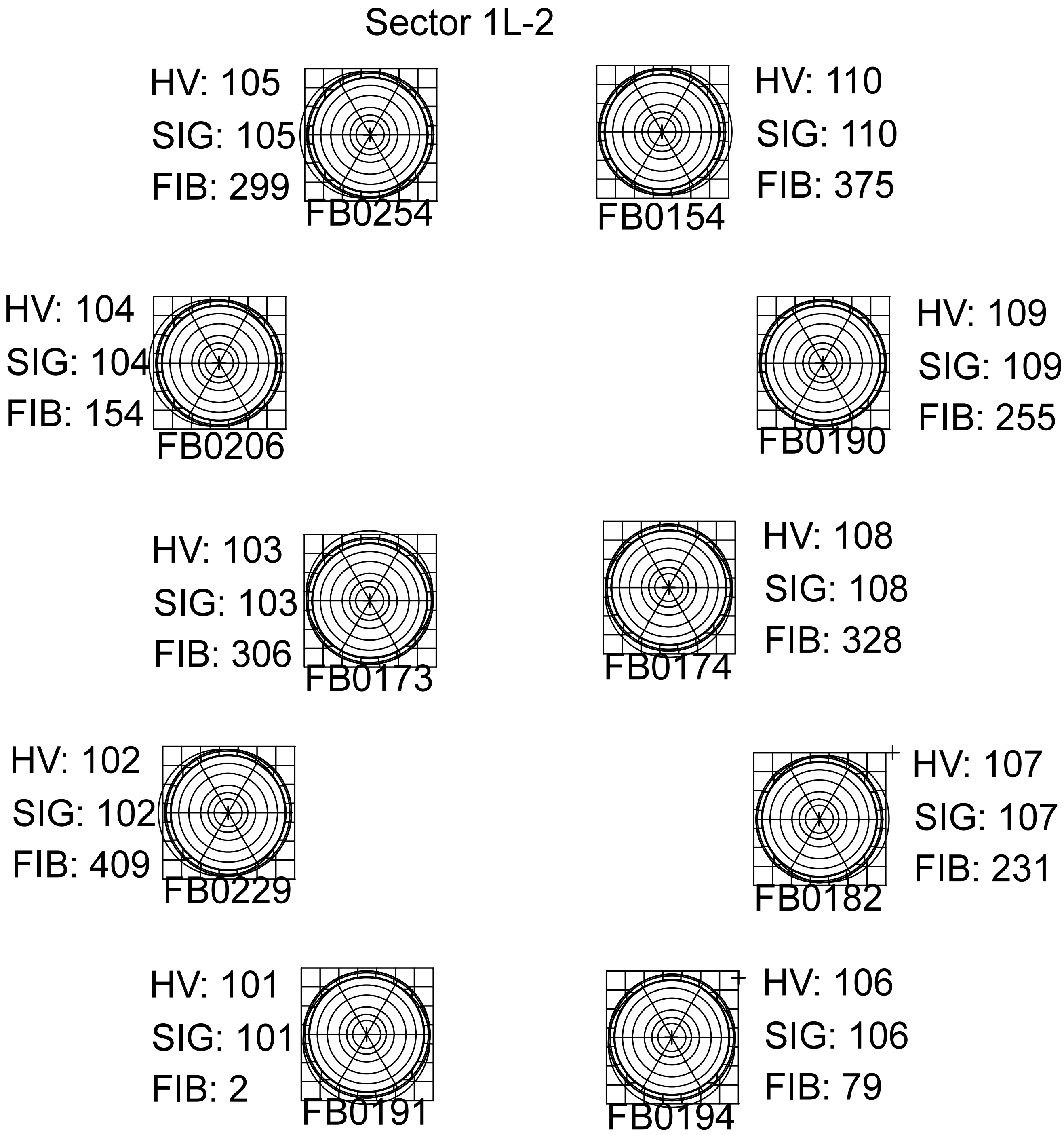

Figure 42: Sector 1L-2. The PMT deployment is seen from the TPC outside.

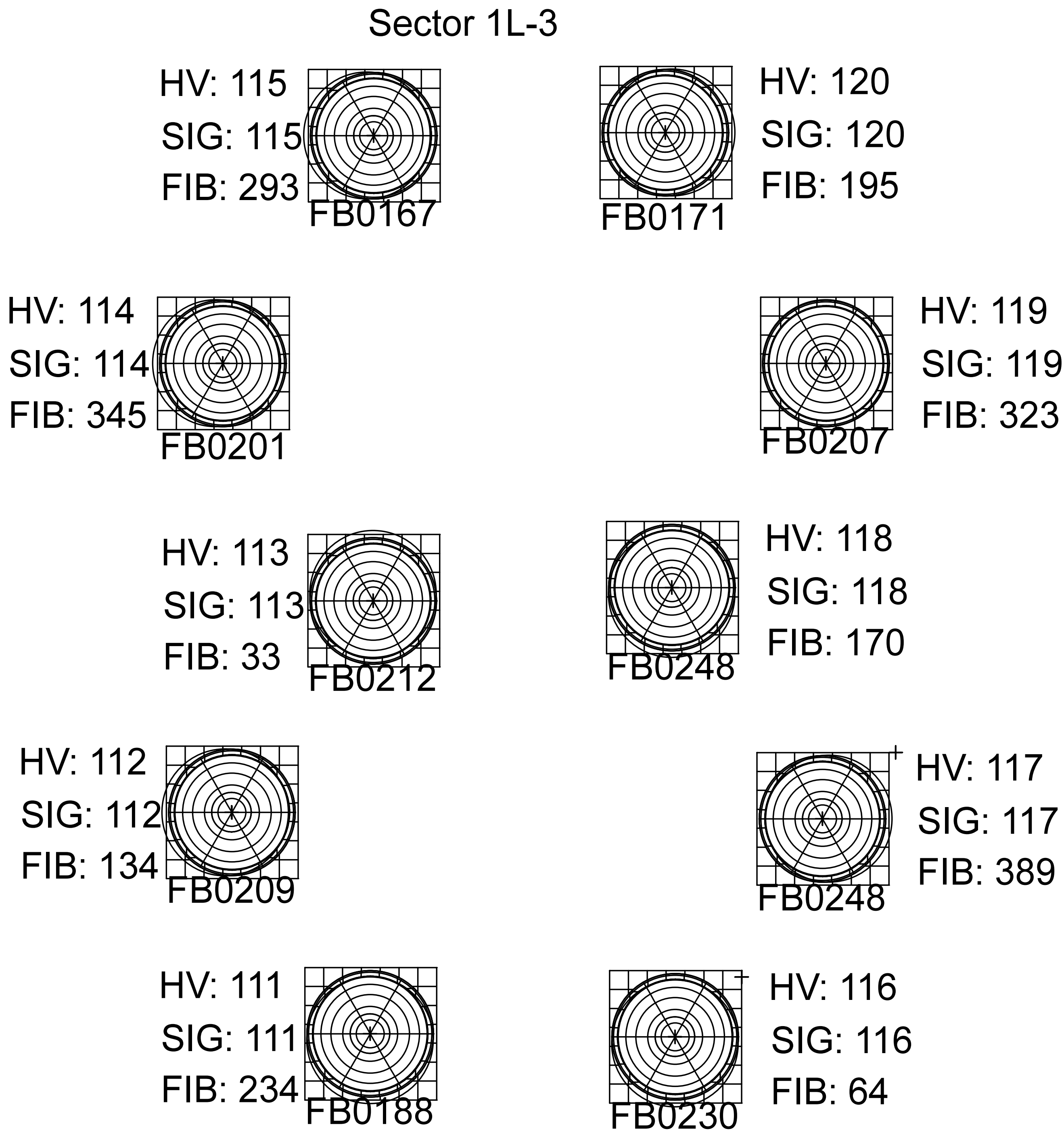

Figure 43: Sector 1L-3. The PMT deployment is seen from the TPC outside.

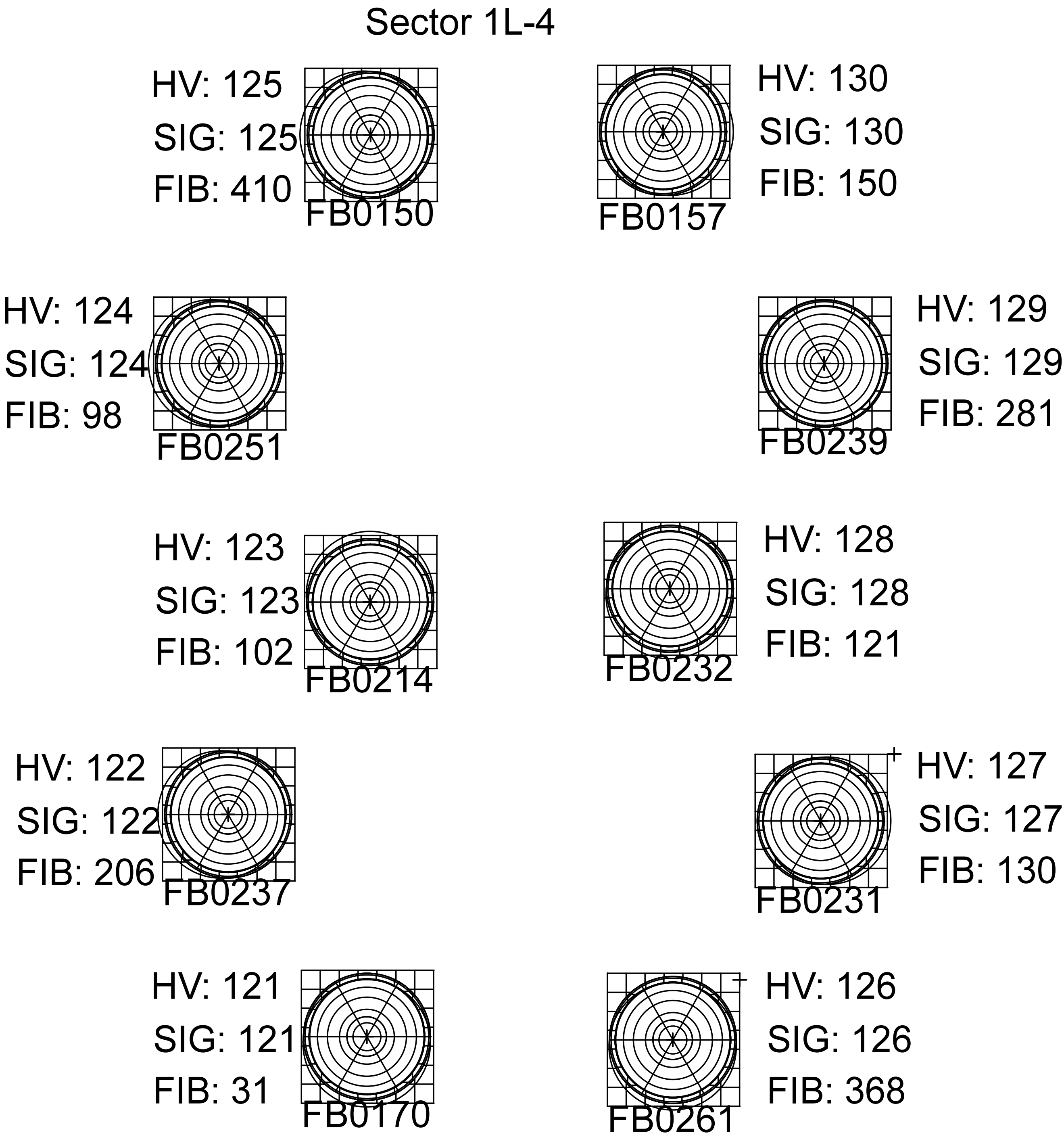

Figure 44: Sector 1L-4. The PMT deployment is seen from the TPC outside.

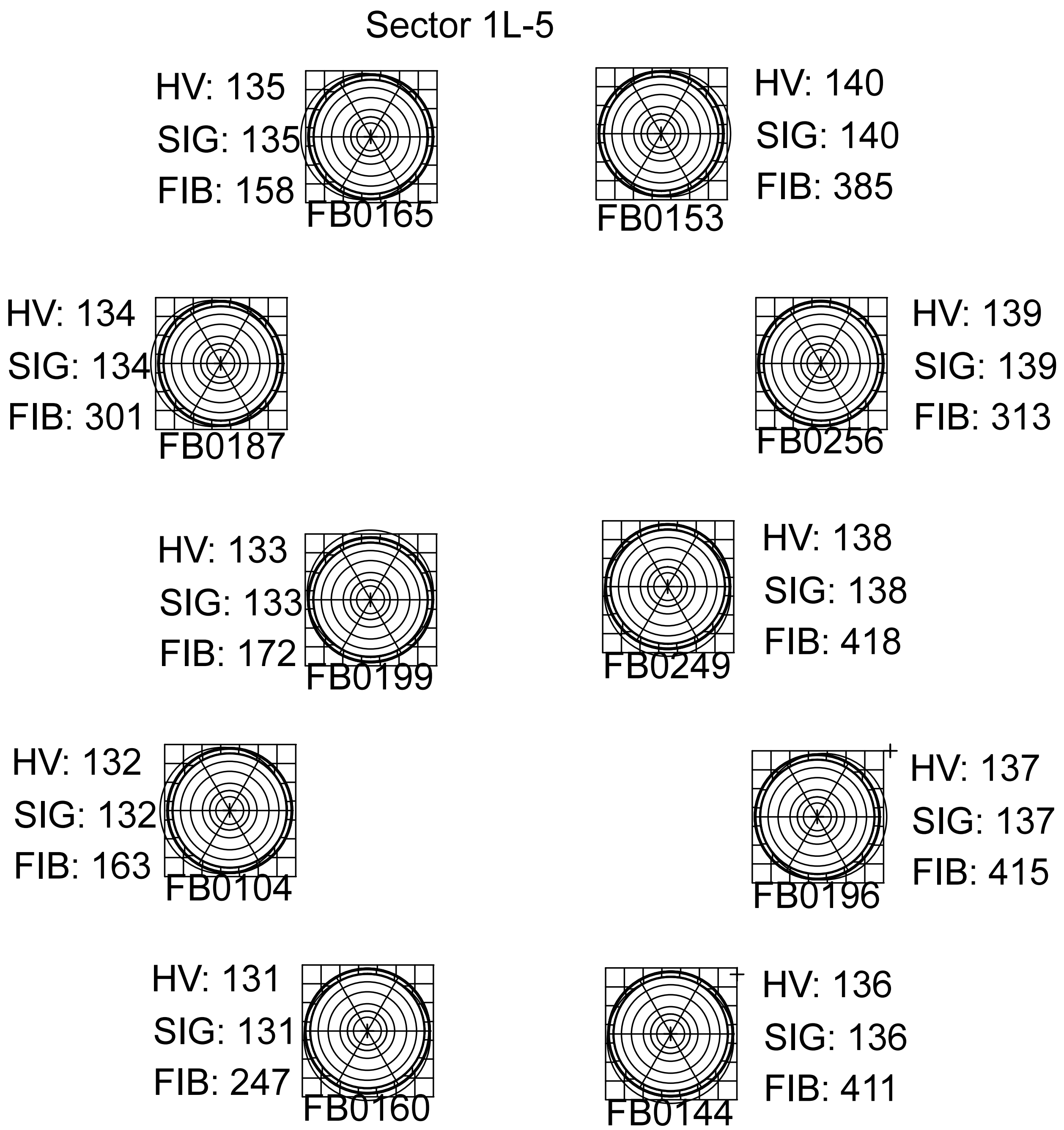

Figure 45: Sector 1L-5. The PMT deployment is seen from the TPC outside.

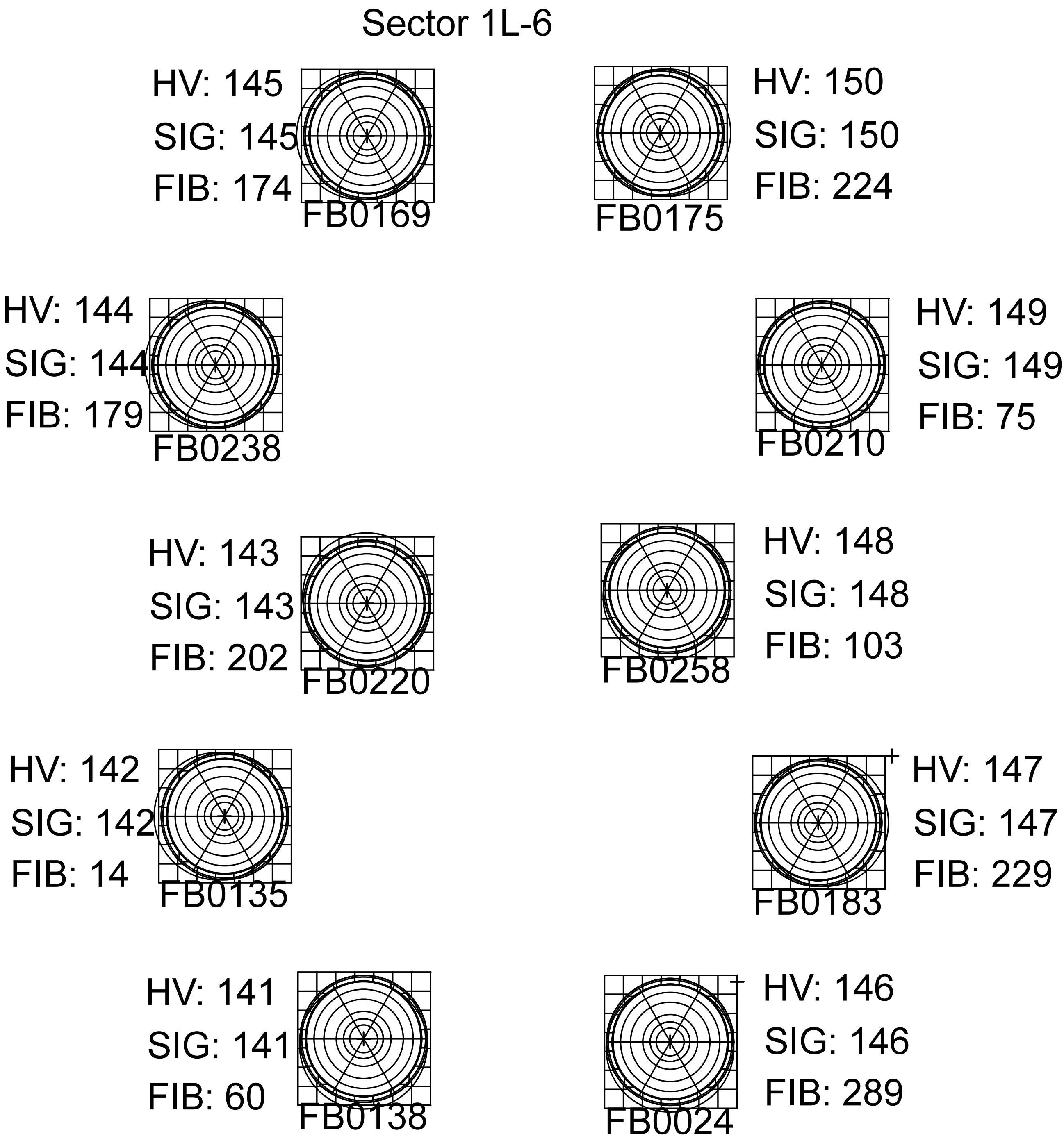

Figure 46: Sector 1L-6. The PMT deployment is seen from the TPC outside.

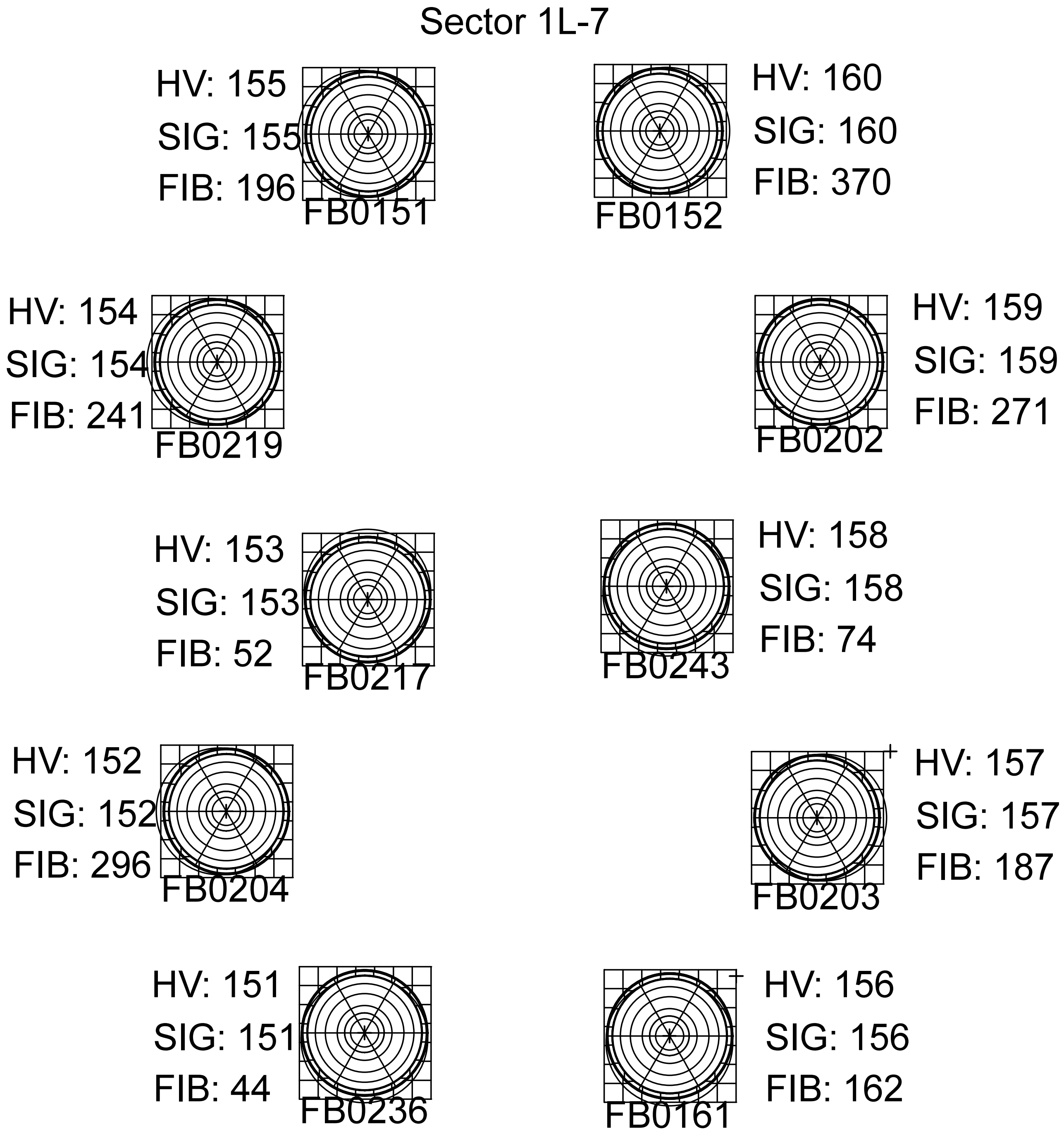

Figure 47: Sector 1L-7. The PMT deployment is seen from the TPC outside.

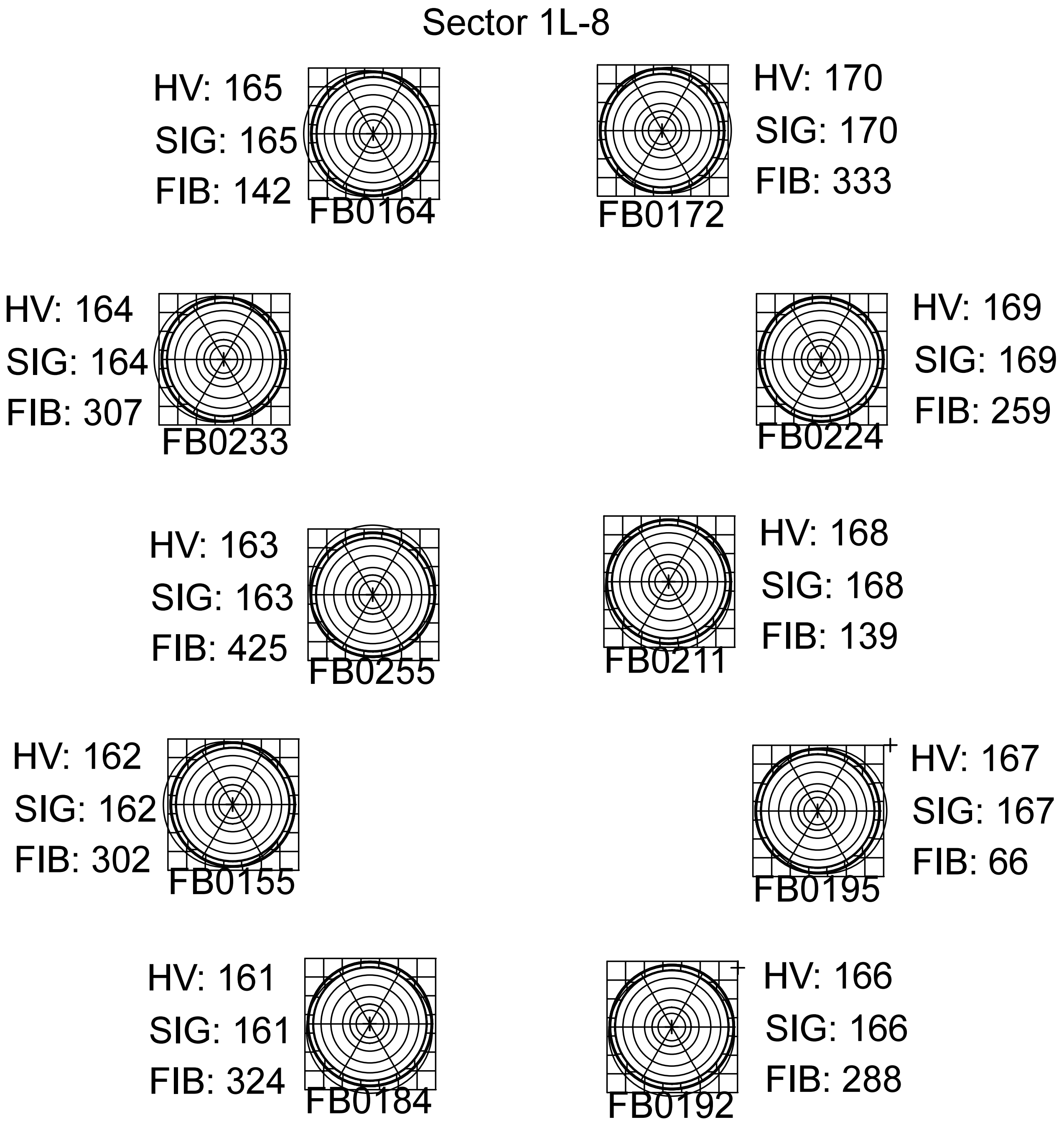

Figure 48: Sector 1L-8. The PMT deployment is seen from the TPC outside.

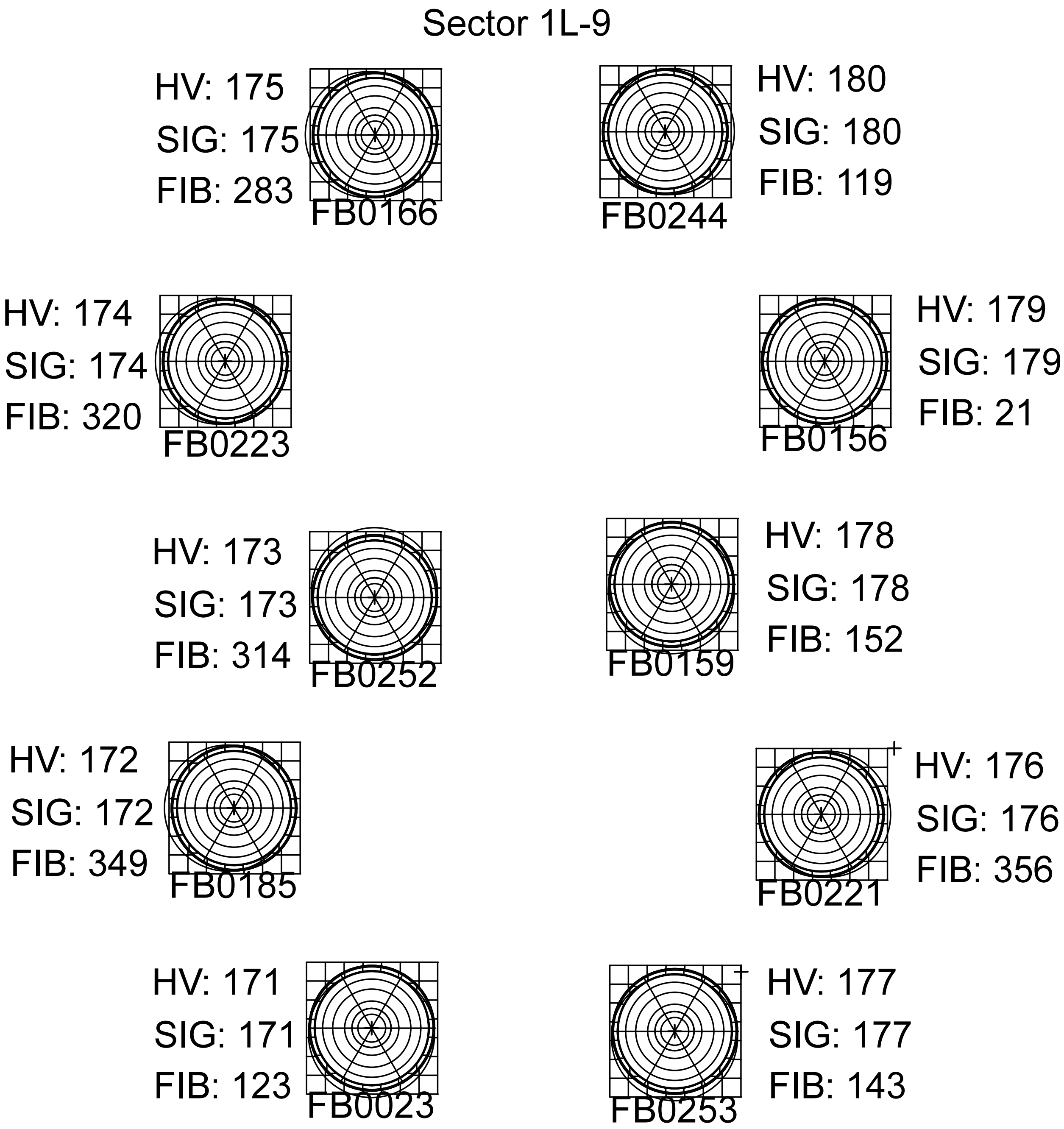

Figure 49: Sector 1L-9. The PMT deployment is seen from the TPC outside.

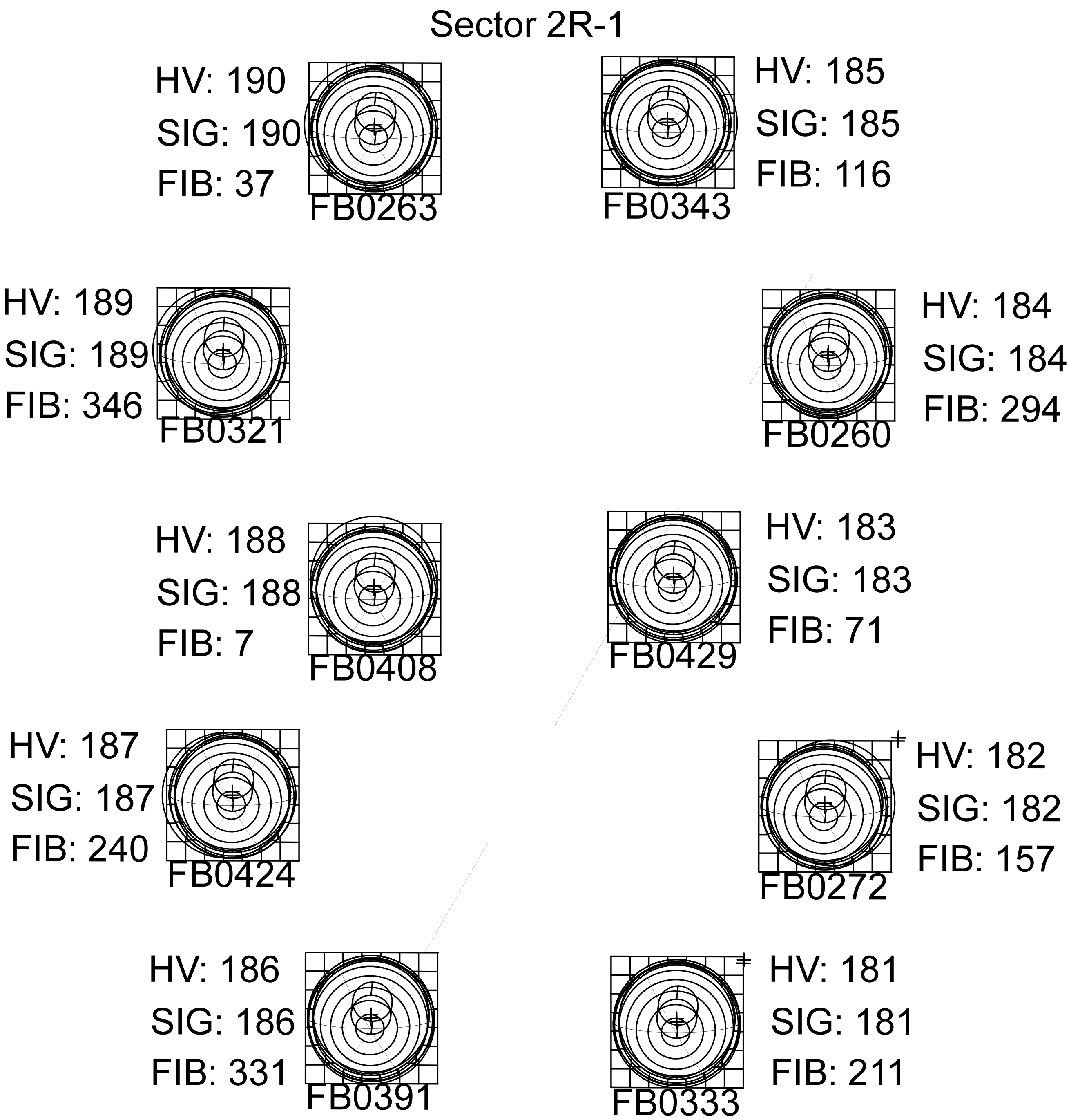

Figure 50: Sector 2R-1. The PMT deployment is seen from the TPC outside.

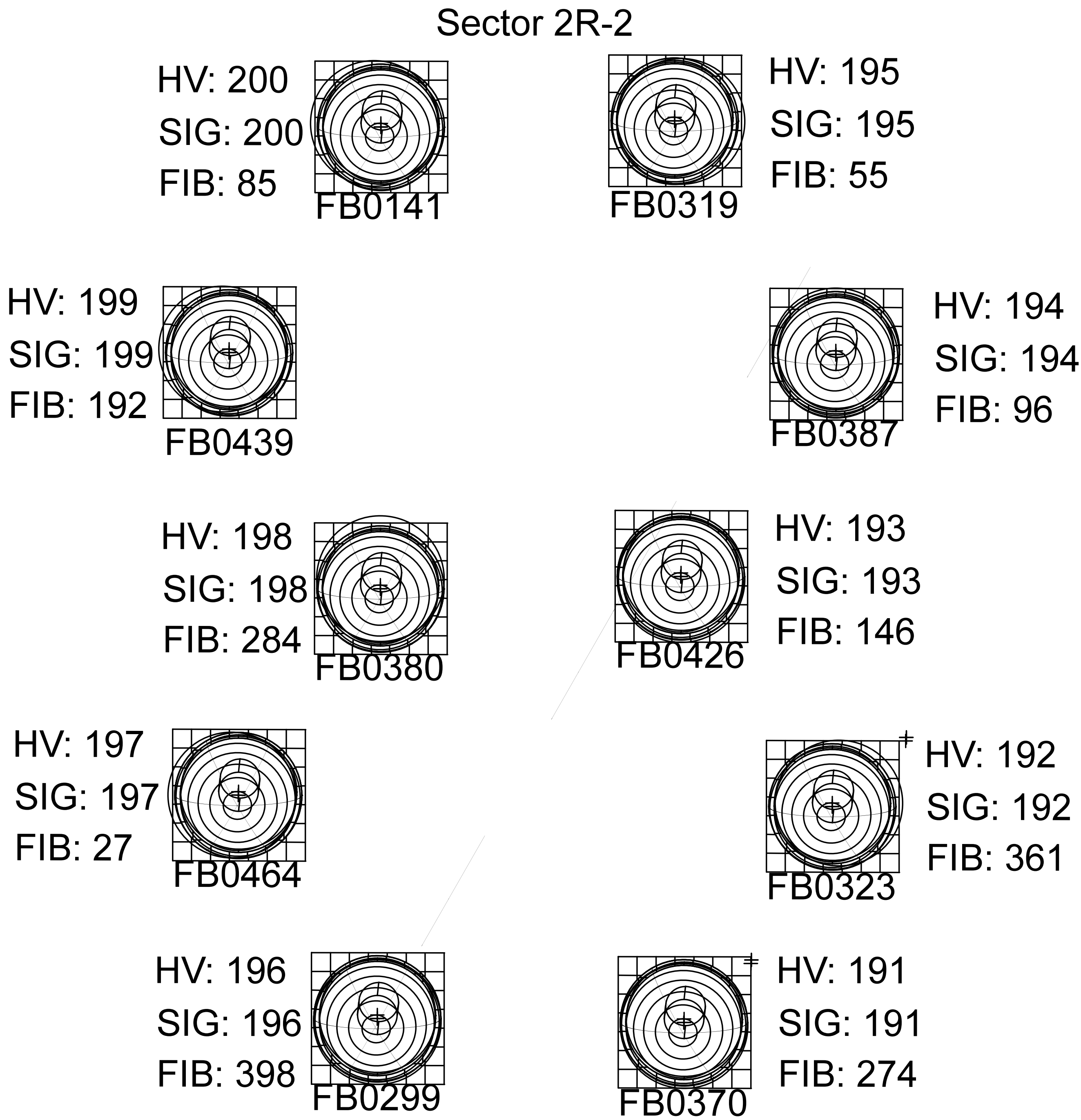

Figure 51: Sector 2R-2. The PMT deployment is seen from the TPC outside.

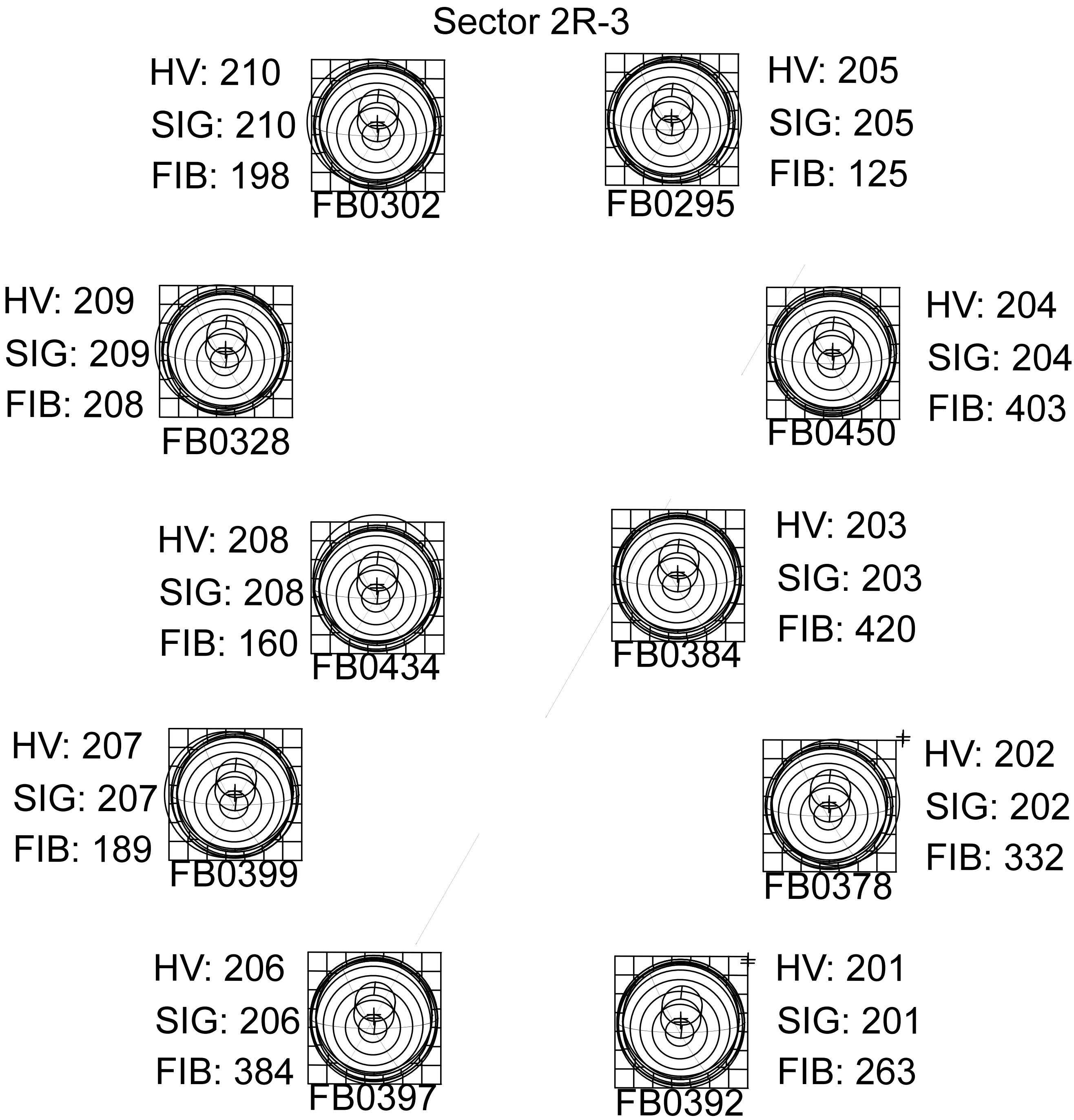

Figure 52: Sector 2R-3. The PMT deployment is seen from the TPC outside.

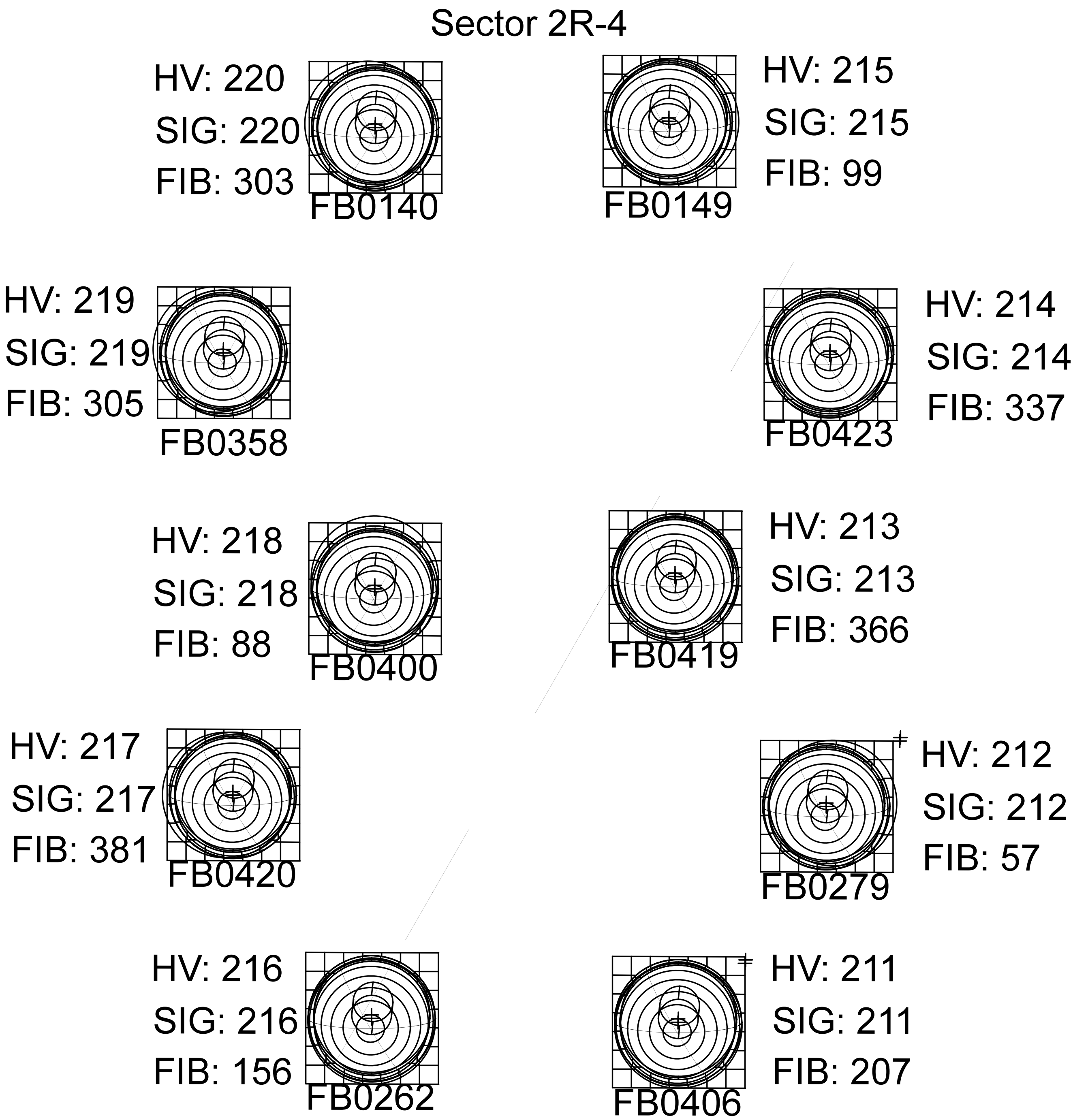

Figure 53: Sector 2R-4. The PMT deployment is seen from the TPC outside.

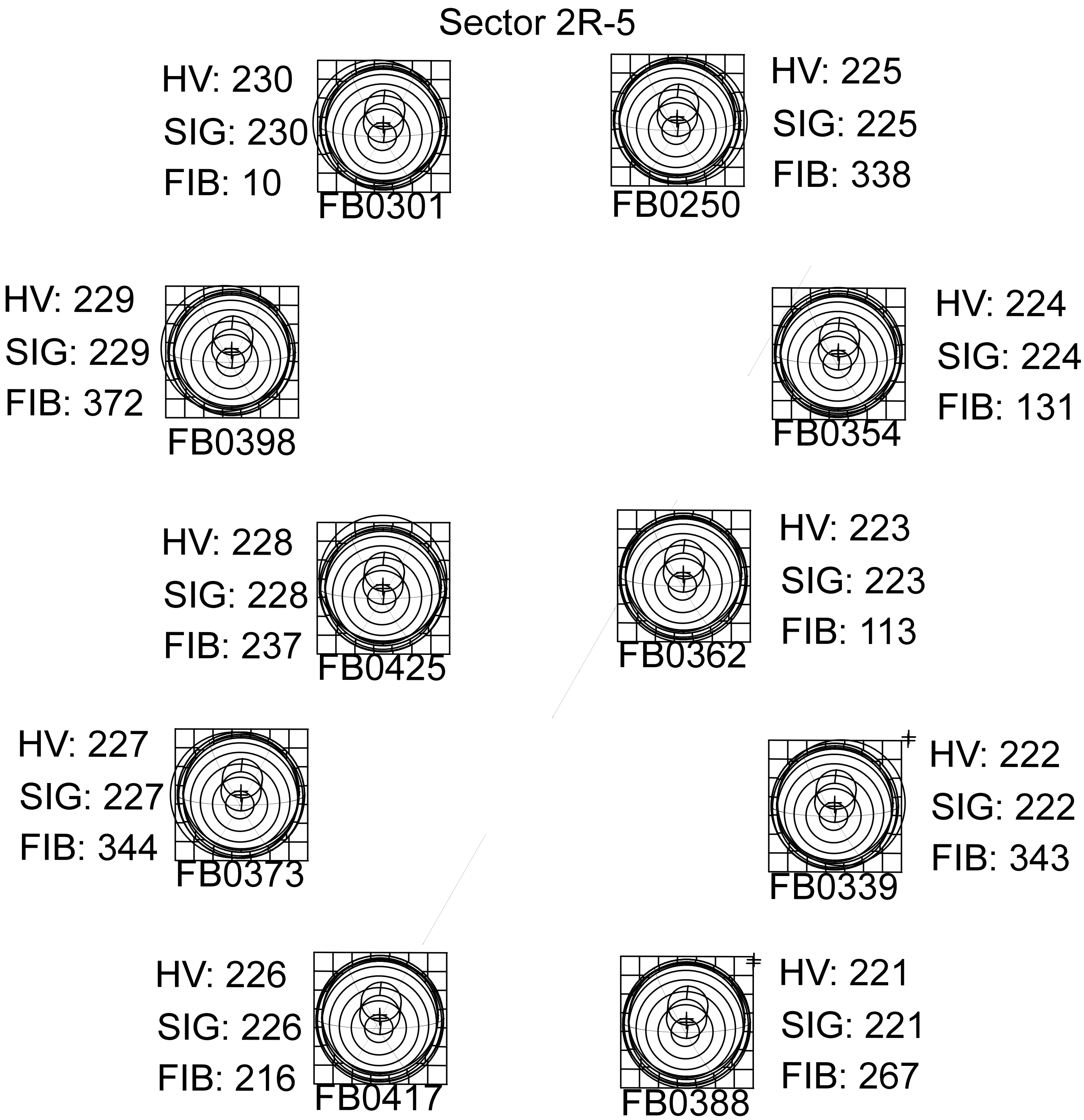

Figure 54: Sector 2R-5. The PMT deployment is seen from the TPC outside.

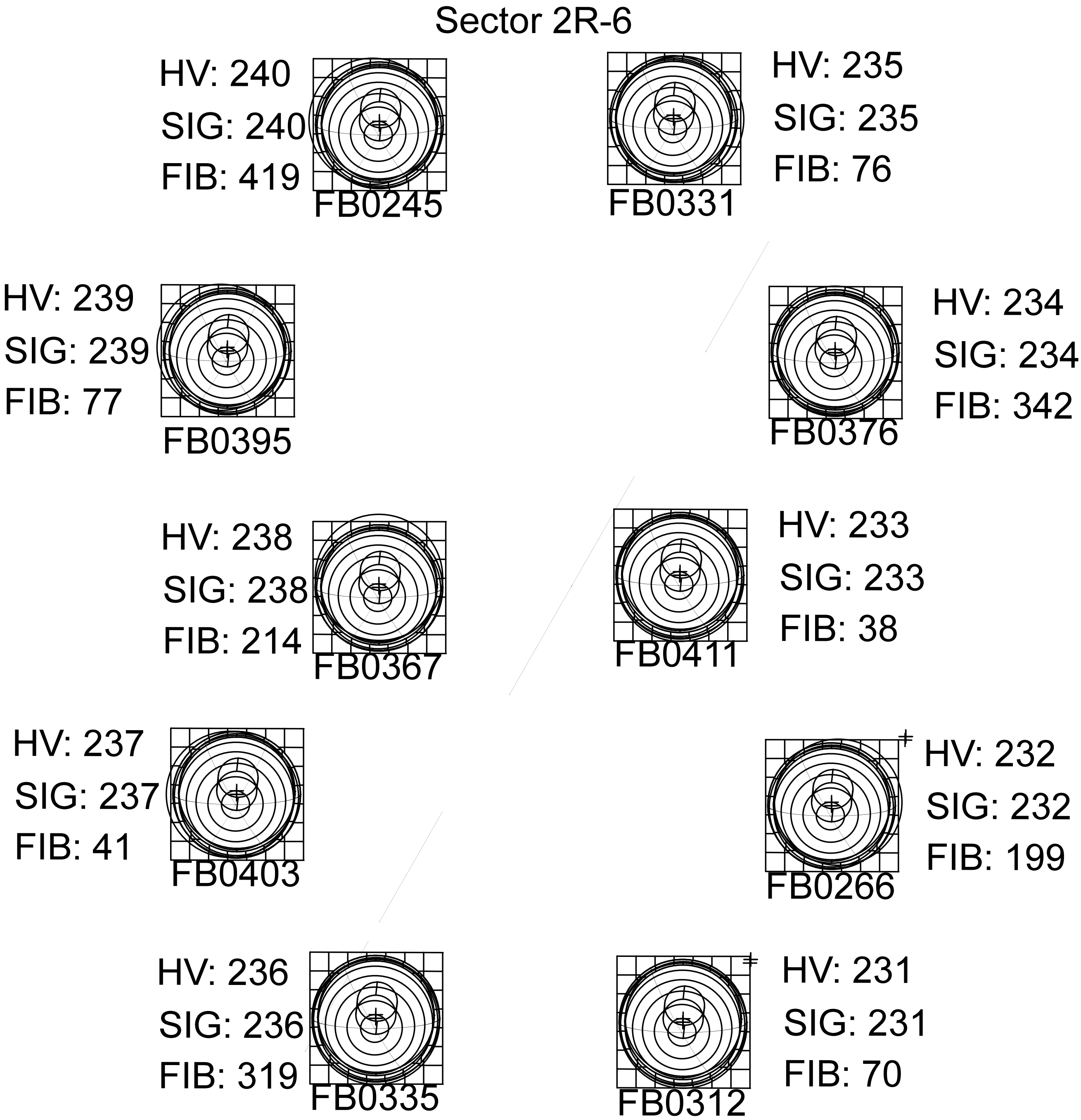

Figure 55: Sector 2R-6. The PMT deployment is seen from the TPC outside.

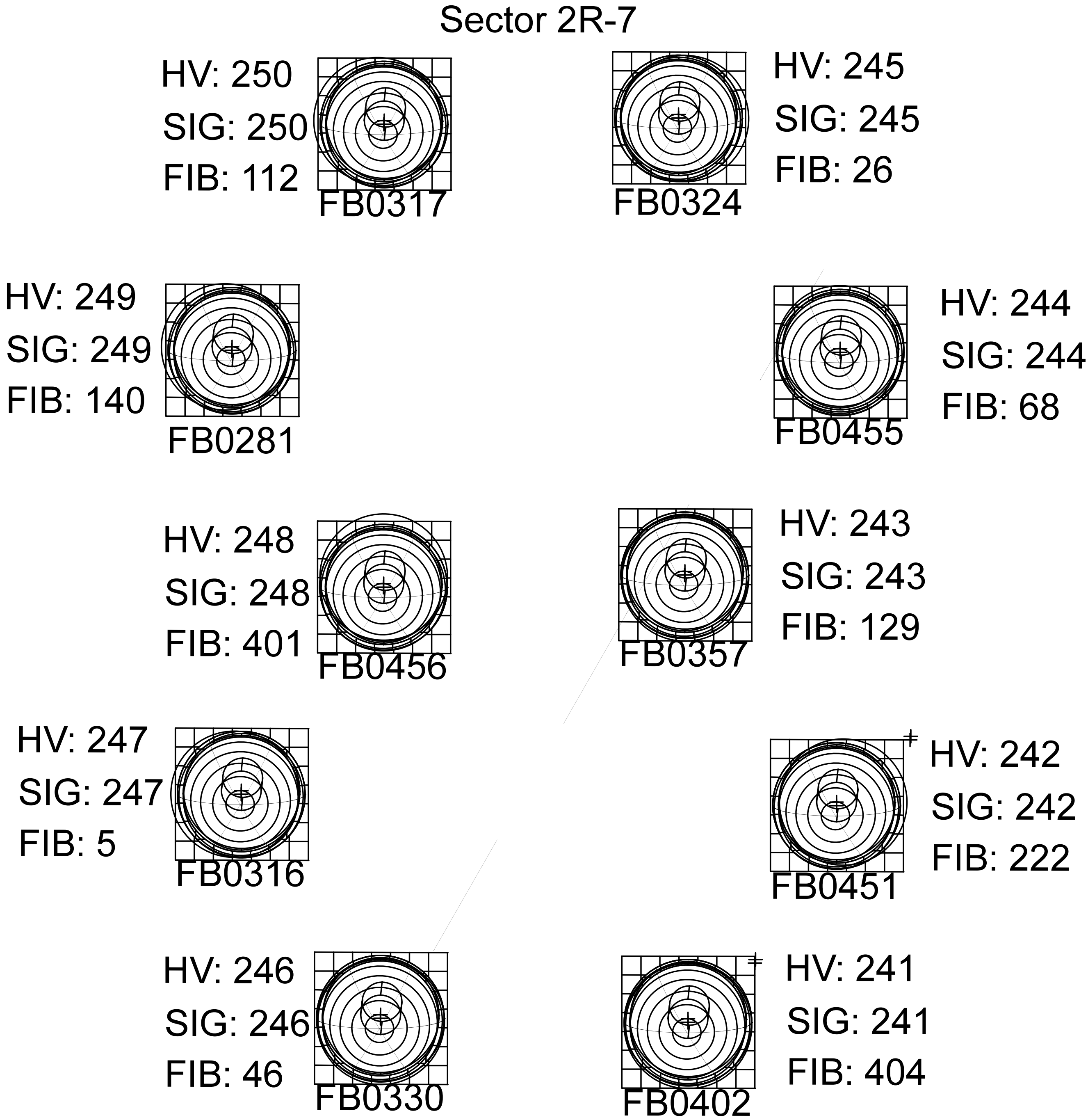

Figure 56: Sector 2R-7. The PMT deployment is seen from the TPC outside.

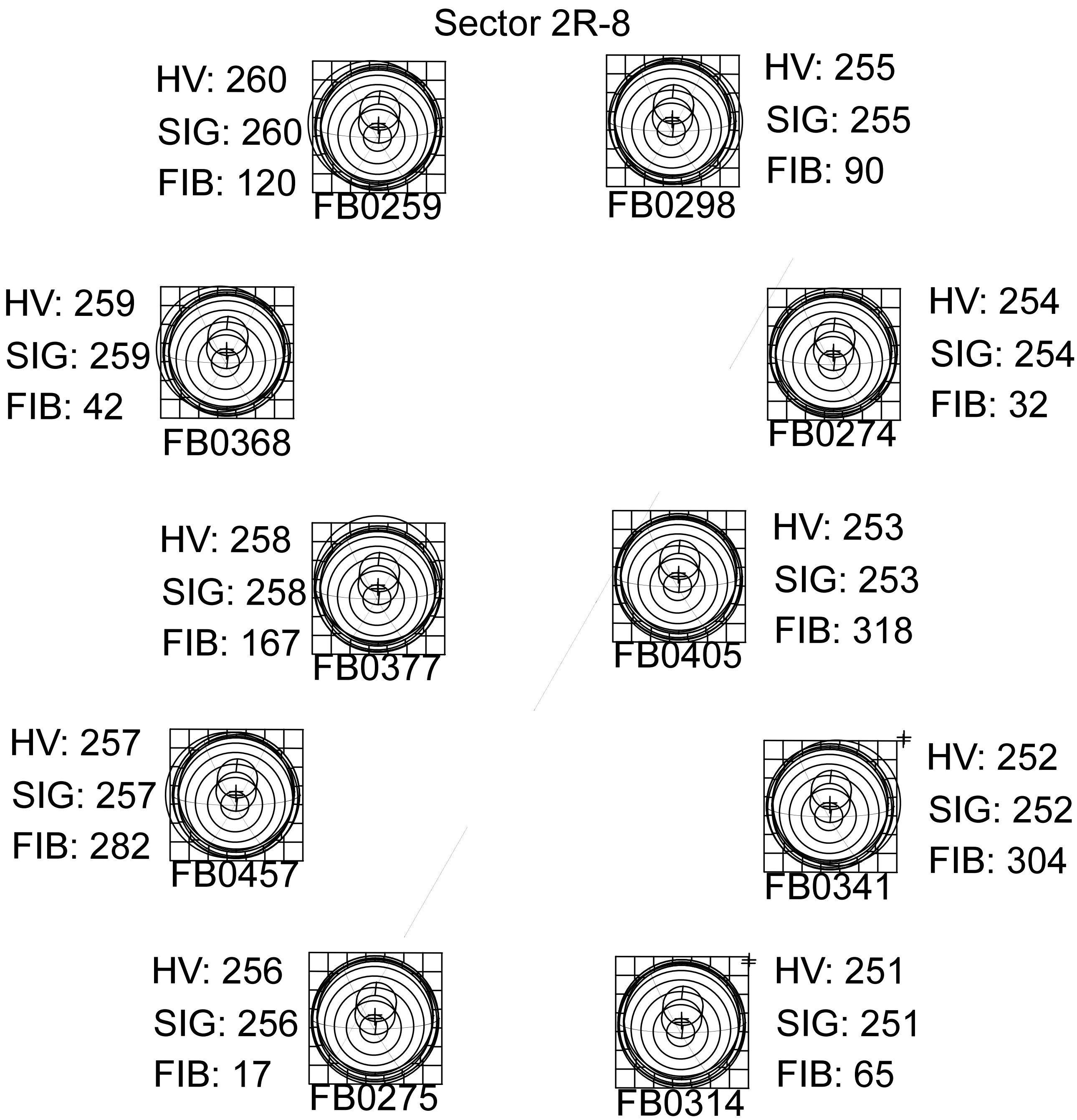

Figure 57: Sector 2R-8. The PMT deployment is seen from the TPC outside.

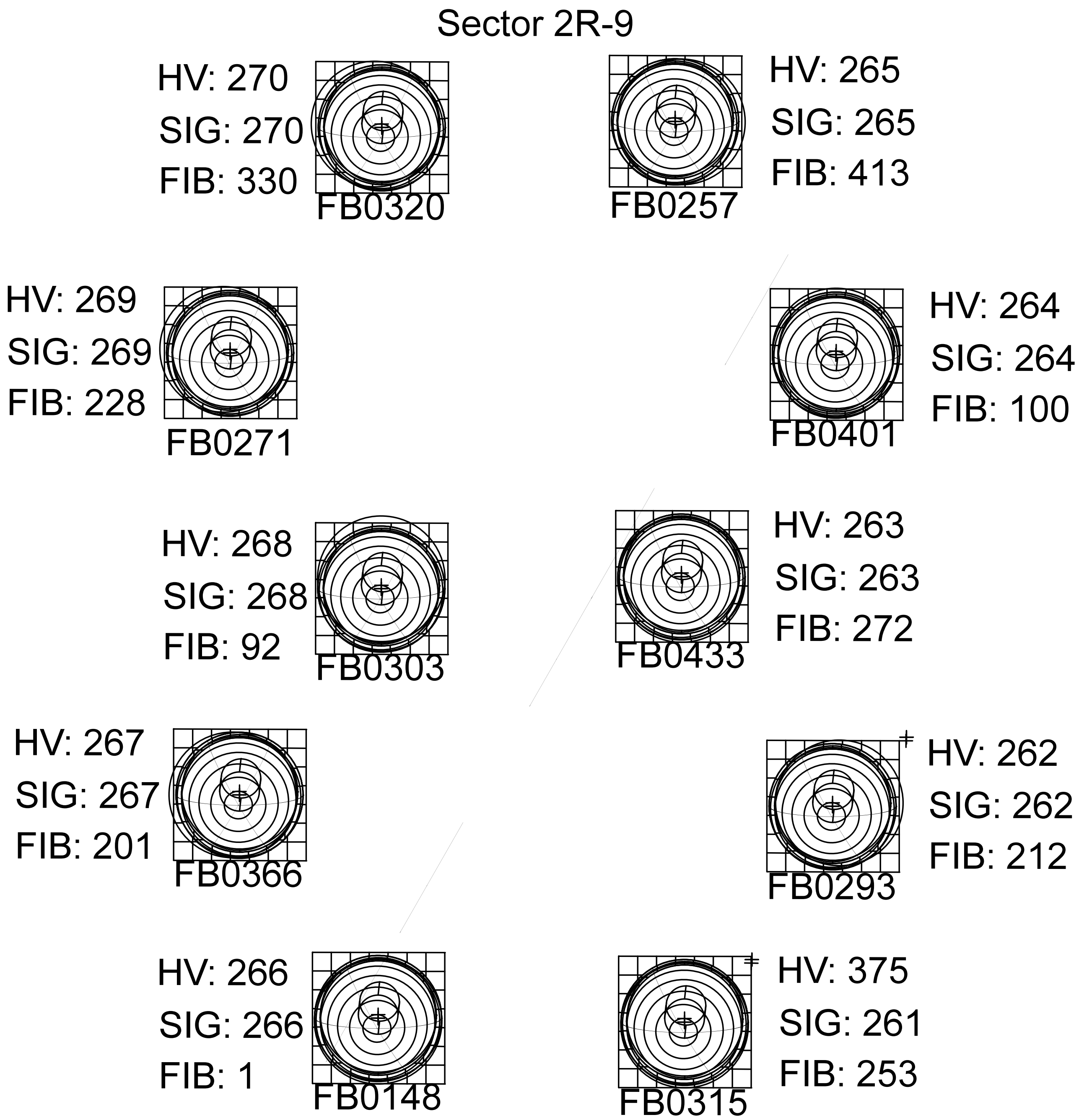

Figure 58: Sector 2R-9. The PMT deployment is seen from the TPC outside.

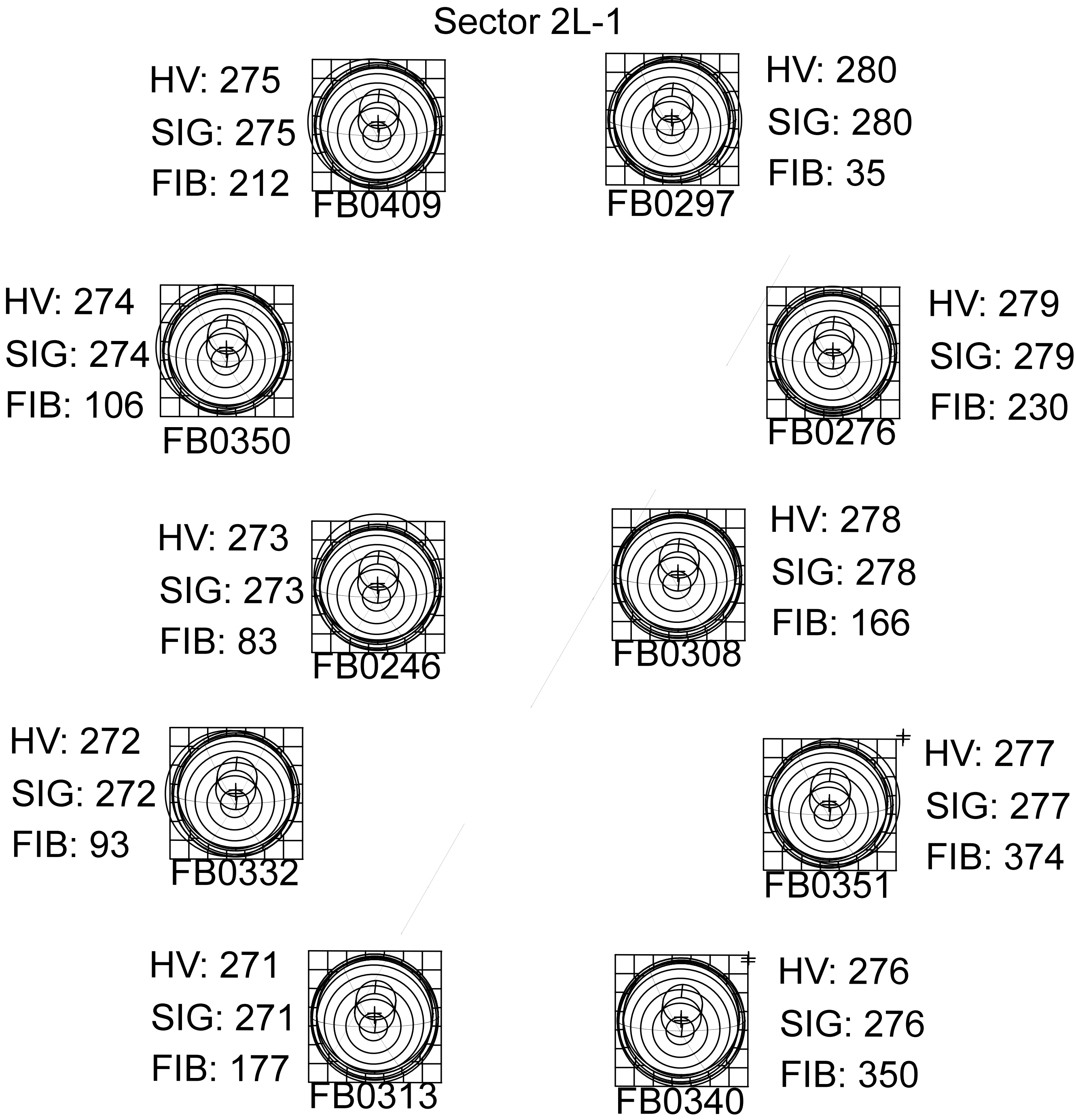

Figure 59: Sector 2L-1. The PMT deployment is seen from the TPC outside.

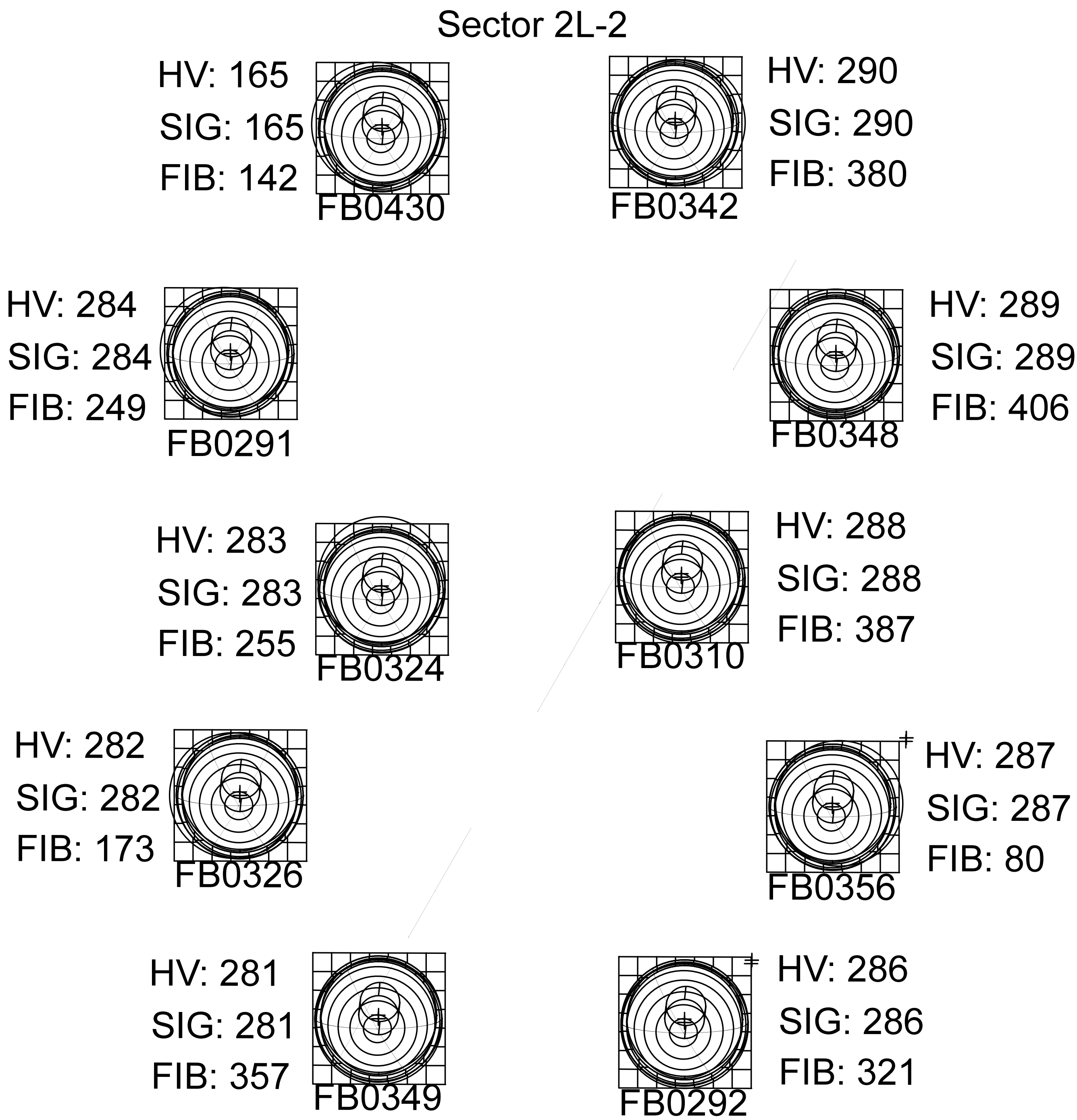

Figure 60: Sector 2L-2. The PMT deployment is seen from the TPC outside.

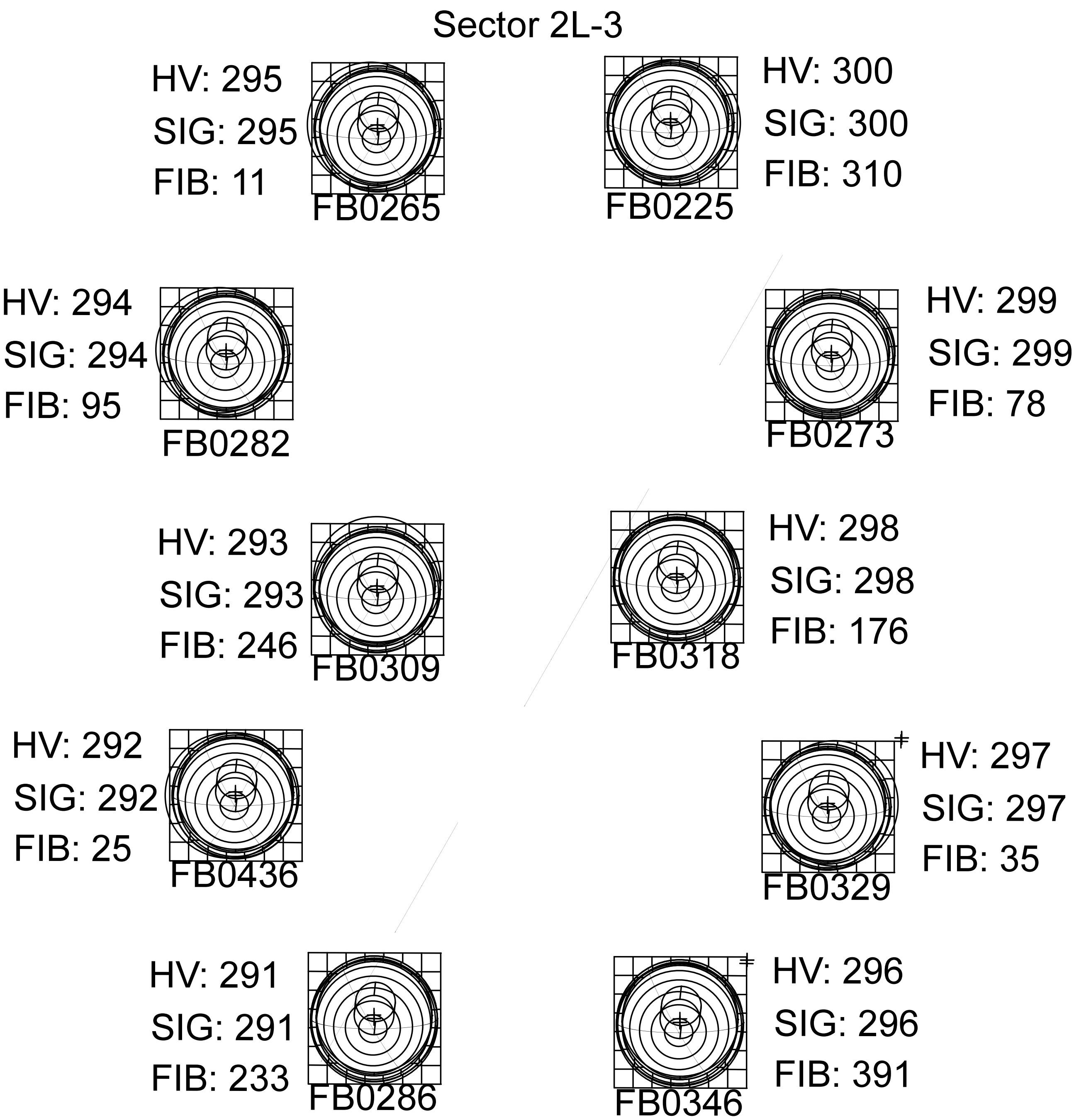

Figure 61: Sector 2L-3. The PMT deployment is seen from the TPC outside.

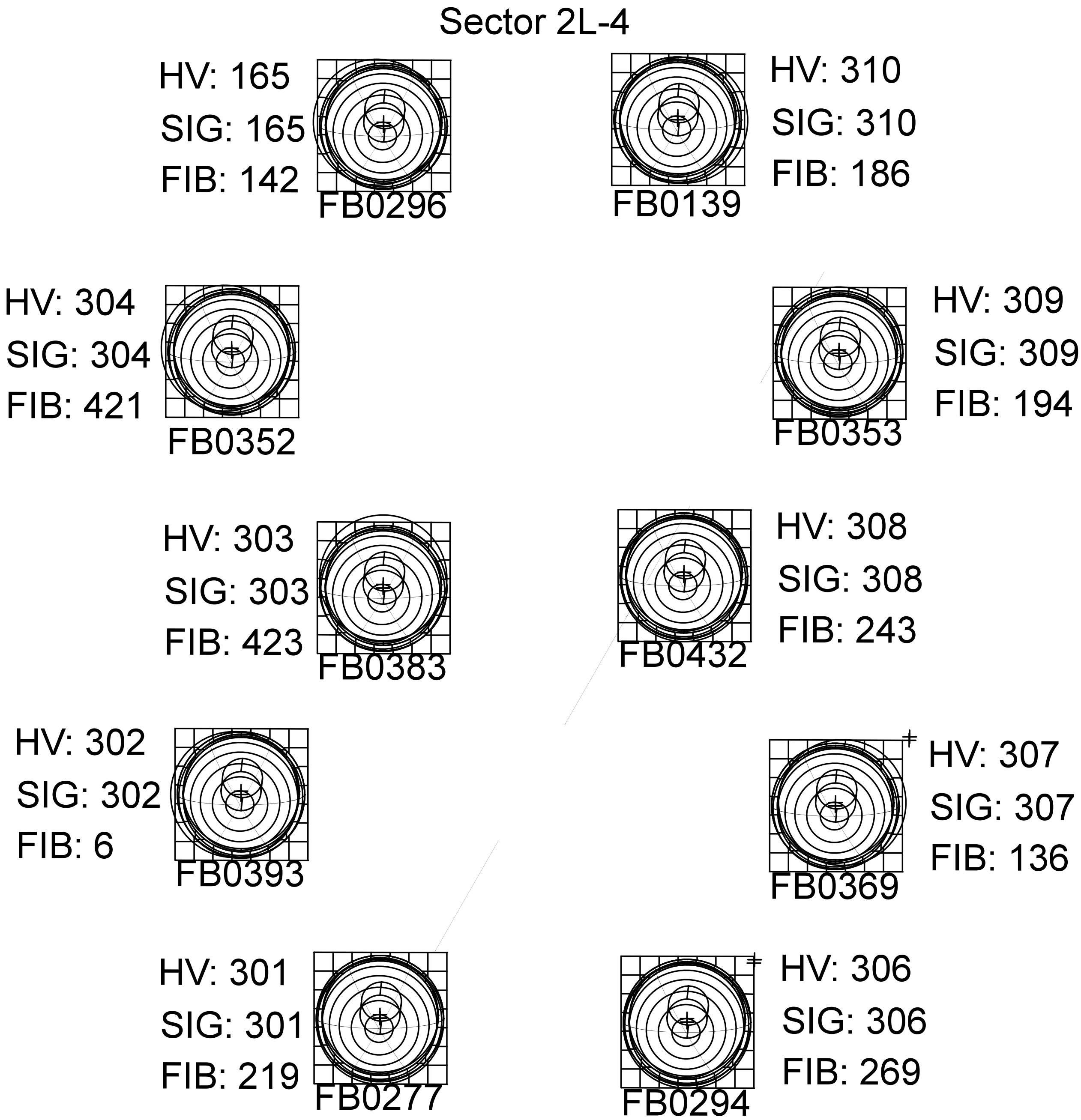

Figure 62: Sector 2L-4. The PMT deployment is seen from the TPC outside.

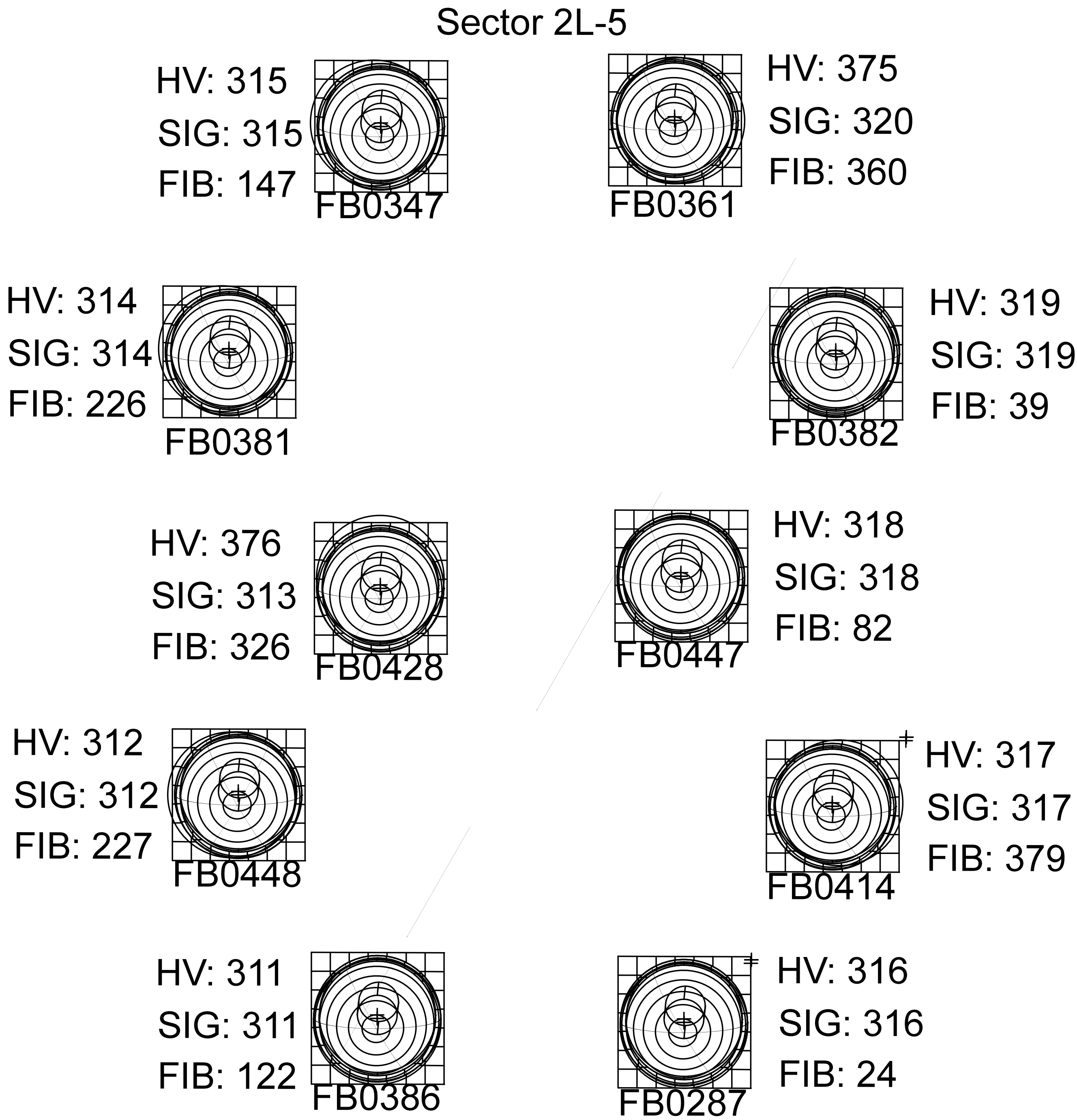

Figure 63: Sector 2L-5. The PMT deployment is seen from the TPC outside.

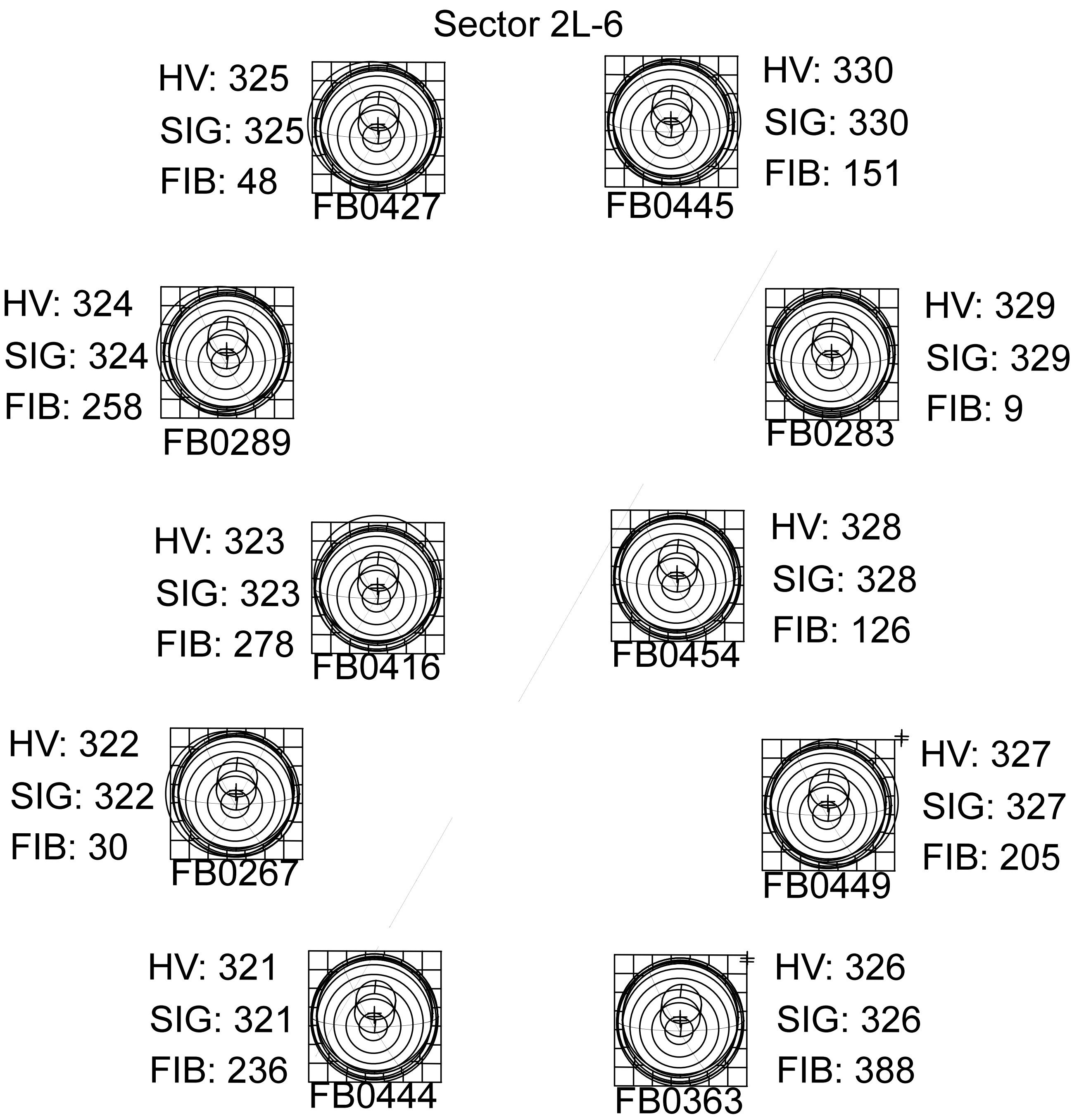

Figure 64: Sector 2L-6. The PMT deployment is seen from the TPC outside.

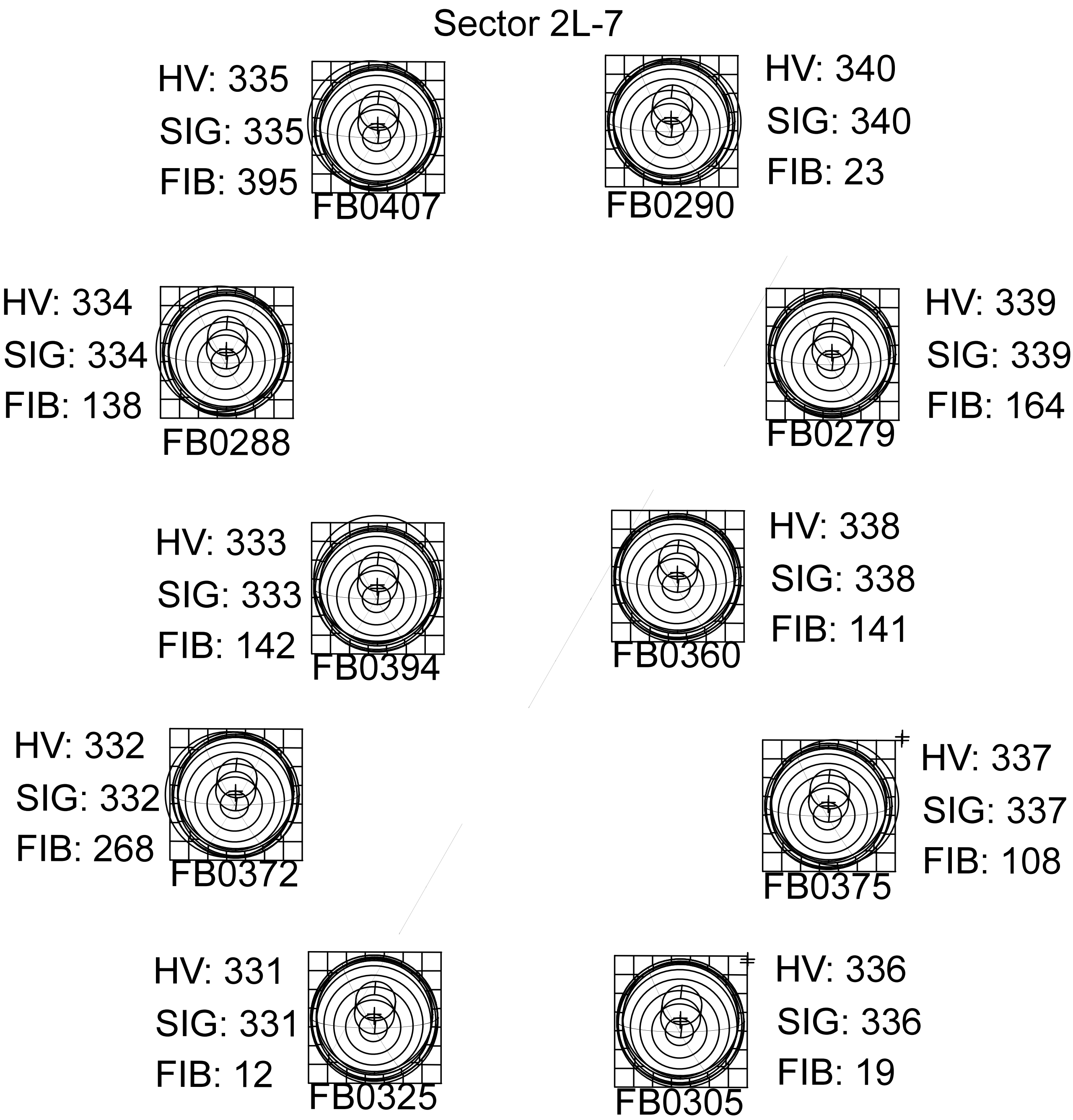

Figure 65: Sector 2L-7. The PMT deployment is seen from the TPC outside.

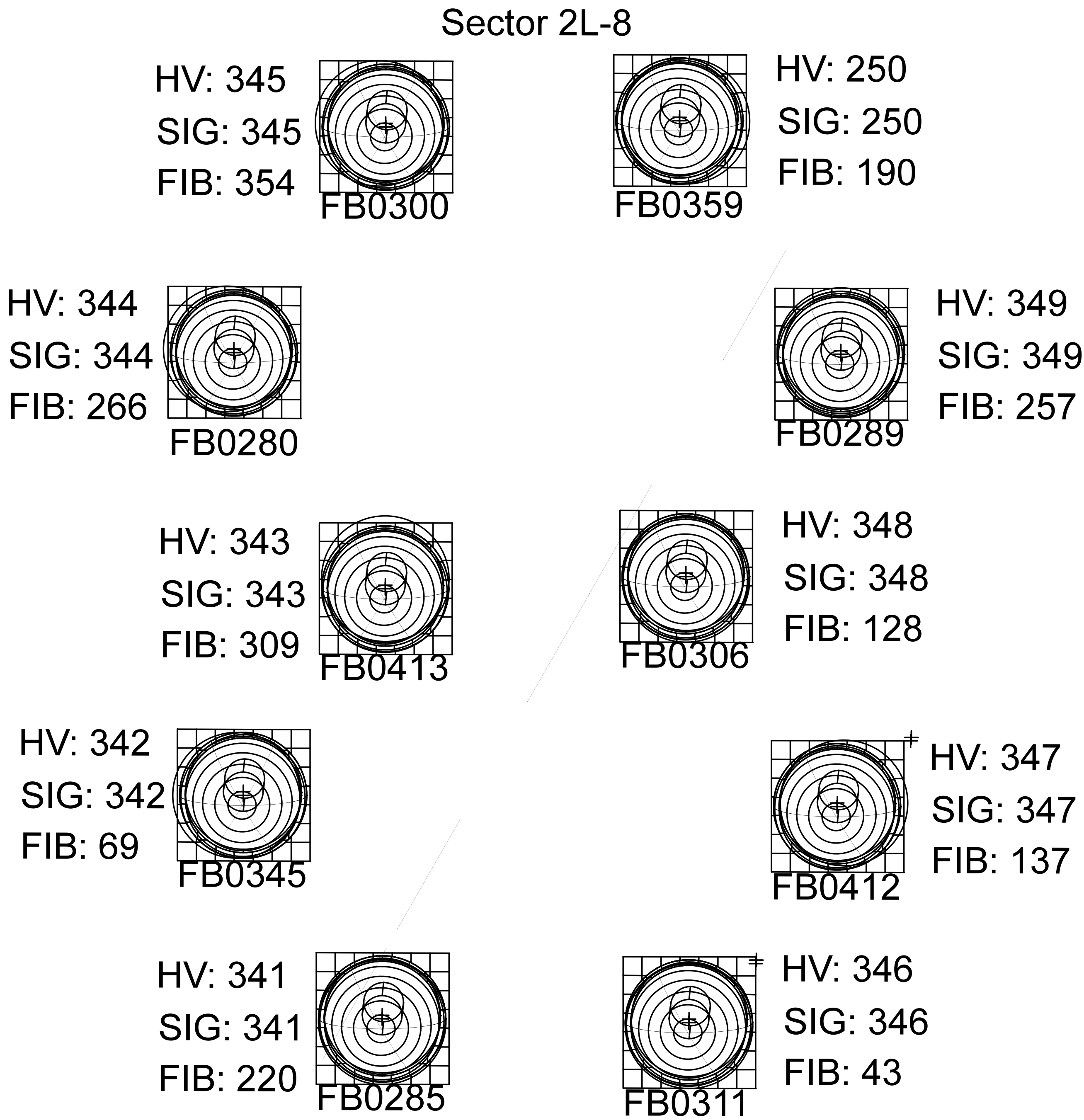

Figure 66: Sector 2L-8. The PMT deployment is seen from the TPC outside.

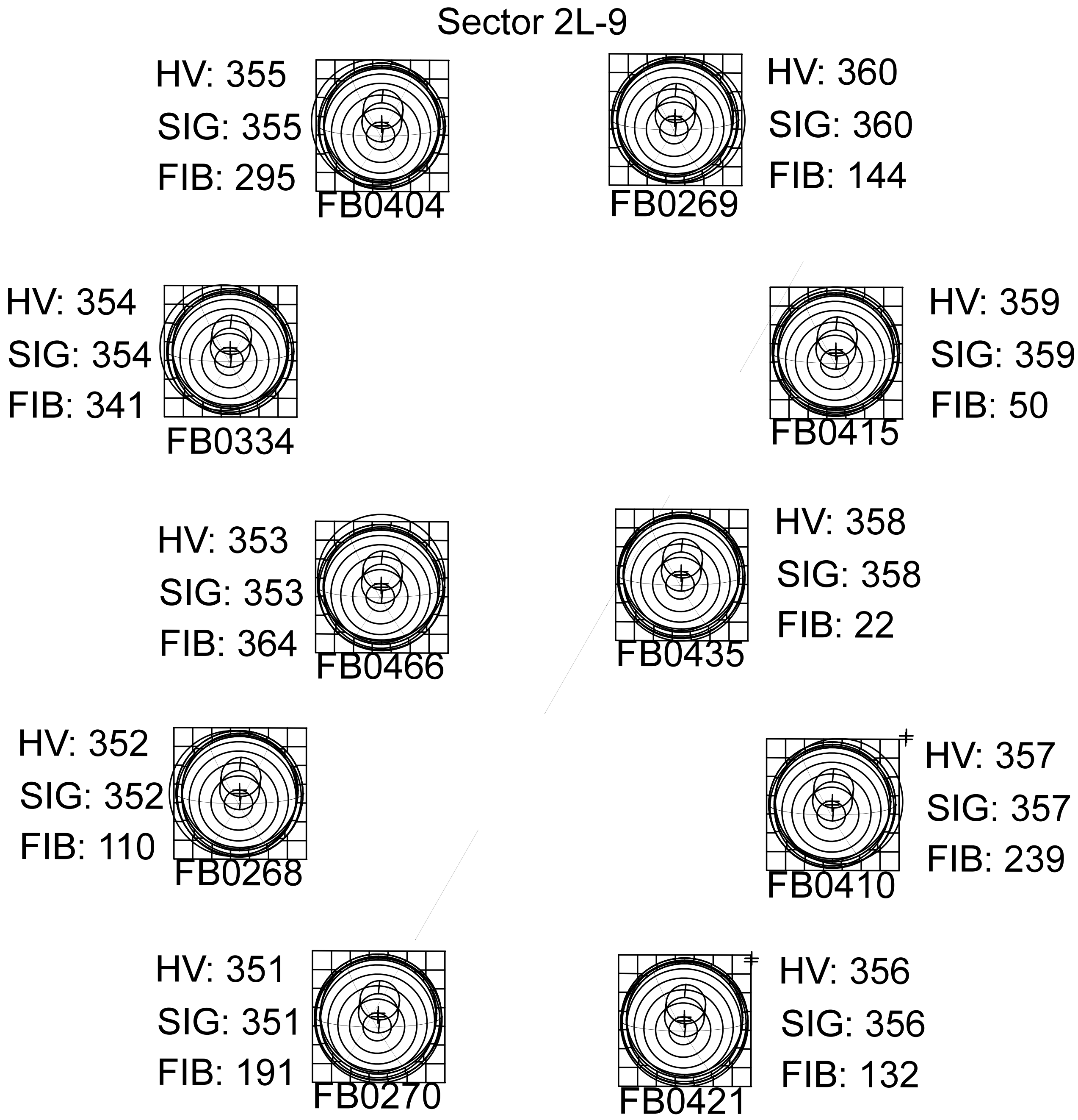

Figure 67: Sector 2L-9. The PMT deployment is seen from the TPC outside.